AN ABSTRACT OF THE DISSERTATION OF

Matthew Y. Coblyn for the degree of Doctor of Philosophy in Chemical Engineering presented on February 5, 2015.

Title: An Investigation of Multiphase Flow in Complex Microchannel Geometries for Hemodialysis Systems Using Residence Time Distribution Analysis

Abstract approved: _____
Goran N. Jovanovic

There are approximately 2.2 million cases of End-stage Renal Disease (ESRD) worldwide and current hemodialysis treatment is costly and ultimately insufficient compared to kidney transplantation. There is a strong need to arrive at a better solution for treating ESRD. Microchannel-based hemodialysis is one proposed option, already shown to have improved filtration performance characteristics over conventional hemodialysis. It has the potential to greatly improve the quality of life for patients but before microchannel hemodialysis is utilized in patient homes, there are still important challenges that must be overcome. A test loop was developed for measuring the pulse response of a dye tracer injected into a dialyzer device for the purpose of detecting defects, developing residence time distributions and characterizing lamina design. Four lamina designs were investigated: 1) a 60 microchannel array with slim asymmetric triangular headers, 2) a 60 microchannel array with wide asymmetric triangular headers, 3) a 60 microchannel array with wide asymmetric triangular headers filled with micro-post features, and 4) a micro-post grid pattern throughout the entire lamina. As a diagnostic tool for detecting defects, the pulse response test loop performed close to expectations, able to detect a difference in mean residence time for design 1 when only 4 of 60 channels were

obstructed or 4.1% difference in total system volume. Residence time distributions (RTD) of the dialyzer devices were obtained by deconvoluting the pulse response measurements. RTD variance tended to lower for designs that are more dominated, volume-wise, by the microchannel array versus the headers. These results also pointed out a discrepancy between the idealized conceptual device and the real fabricated device by emphasizing how issues such as sagging or bulging, fabrication tolerances, and miniscule misalignments can significantly impact a microchannel device. A multi-segmented CFD model developed for pairing with the pulse response test loop and dialyzer, showed good agreement between visual observation of the tracer in simulations and experiments, and the shape and peak height of the output profiles. In addition to this work, a Polyethylene oxide (PEO) – polybutadiene (PB) – polyethylene oxide triblock polymer coating, originally intended to improve device biocompatibility and therapeutic applications, was investigated for its effect on reducing bubble stagnation in microchannel lamina for dialysis use, thereby improving filtration performance. Experimental results show a statistically significant reduction in blocked channels by stationary bubbles for a 40 microchannel PEO-coated lamina versus a similar uncoated lamina between nominal average channel velocities of 1.8 to 3.6 cm/s. A numerical simulation based on the Lattice Boltzmann modeling approach indicate that beneficial effects may be ascribed to the maintenance of a lubricating, thin liquid film around the bubble. Experimental and numerical simulation results serve to validate the additional bubble lubricating utility of the PEO-PB-PEO coating.

An Investigation of Multiphase Flow in Complex Microchannel Geometries for Hemodialysis Systems Using Residence Time Distribution Analysis

by
Matthew Y. Coblyn

A DISSERTATION

submitted to

Oregon State University

in partial fulfillment of
the requirement for the
degree of

Doctor of Philosophy

Presented February 5, 2015
Commencement June 2015

Doctor of Philosophy dissertation of Matthew Y. Coblyn presented on February 5, 2015

APPROVED:

Major Professor, representing Chemical Engineering

Head of the School of Chemical, Biological, and Environmental Engineering

---

Dean of the Graduate School

I understand that my dissertation will become part of the permanent collection of Oregon State University libraries. My signature below authorizes release of my dissertation to any reader upon request.

Matthew Y. Coblyn, Author

ACKNOWLEDGEMENTS

I want to express sincere gratitude to all of the P.I.'s on the NIH dialyzer grant for their work to secure funding on this project and providing me with this assistantship throughout my graduate studies. Thank you, Dr. Joe McGuire, for being an amazing undergraduate advisor and starting me on my research path.

I would like to thank my advisor, Dr. Goran Jovanovic, for sharing his incredible breadth of knowledge, providing guidance and support, for teaching me not to be afraid to stick my neck out and tackle the tough problems and who, during the moments in my research that were most challenging and discouraging, always managed to re-inspire me and instill a feeling of deep appreciation to be a part of the field of science and engineering.

Thank you, Patrick McNeff and Dusty Ward, for your hard work in developing fabrication techniques and designing the device. Thank you, Dr. Mahshid Mohammadi, for four years of advice and encouragement. Thank you, Keely Heintz, for working on the PEO-coating and for powering through countless attempts during our first year on this project. Thank you, Dr. Agnieszka Truszkowska, for your knowledge and expertise in computational modeling. And thank you, Robin Wagner, Matthew Petersen, and Corey Lerch, for helping me solve the difficult fabrication challenges we faced early in the project.

I would like to thank all of my lab mates in the Jovanovic group for their advice and friendship, and a special thanks to Dr. Frederick Atadana for sharing an office with me for four years and wasting countless hours discussing anything and everything. I want to thank Peter Krieder, Mike Knapp and Dr. Brendan Flynn for being awesome roommates and creating the oversaturated, blissful memories I'll recall when I look back on grad school.

I want to thank Susannah Lee for her love, support, and patience, spending many late evenings keeping me company in the lab and office over the phone, for encouraging me to expand beyond my familiarities and experience so much more.

Lastly, I want to thank my loving family for their endless support. My sister, Erica, for always looking out for me and helping in every imaginable way outside of research and exams. And to my parents, John and Heakyu, for their encouragement and providing me with all of the opportunities in life that have allowed me to reach this point. Thank you for being a steady and calming presence in my life during these last four years.

TABLE OF CONTENTS

TABLE OF CONTENTS (Continued)

TABLE OF CONTENTS (Continued)

LIST OF FIGURES

LIST OF FIGURES (Continued)

LIST OF FIGURES (Continued)

LIST OF FIGURES (Continued)

LIST OF FIGURES (Continued)

LIST OF FIGURES (Continued)

LIST OF FIGURES (Continued)

LIST OF FIGURES (Continued)

LIST OF TABLES

LIST OF VARIABLES

$f_a^{\xi,eq}(\mathbf{x},t)$	ξ^{th} component equilibrium distribution function in the a^{th} direction
$f_a^{\xi}(\mathbf{x},t)$	ξ^{th} component density distribution function in the a^{th} direction
$\bar{t}, \tau$	Mean residence time
$\mathbf{u}_{\boldsymbol{\xi}}^{eq}$	Equilibrium velocity of the ξ^{th} component
C	Concentration
Ca	Capillary number : $Ca = \eta V / \gamma$
c_s	Speed of Lattice
D	Molecular diffusion coefficient
$\mathbf{D}$	Dispersion coefficient
D_H	Hydraulic diameter
$E(t')$	System response function
$\mathbf{e}_a$	Discrete velocities
$\mathbf{F}_{a,\xi}$	Forcing term for attractive interactions within ξ^{th} component
$\mathbf{F}_{ads,\xi}$	Forcing term for interactions with solids of ξ^{th} component
$\mathbf{F}_{ext,\xi}$	External force acting on the ξ^{th} component
$\mathbf{F}_{r,\xi}$	Forcing term for repulsive interactions of ξ^{th} component with other components
g	Standard gravity
h	Lubrication film thickness
h_z	Depth of microchannel
i	Input column vector
l	Characteristic length for *We*, typically the droplet diameter
L	Characteristic length
m_{tot}	Total mass
o	Output column vector
Q	Volumetric flow rate
r	Reaction coefficient

Re	Reynolds number : $Re = \rho VL/\eta$
$\boldsymbol{s}$	Coefficient matrix containing the system response function
s	Skewness
t	Time
t'	Relative fluid age
u	Velocity
$\mathbf{u}'$	Composite velocity
$\mathbf{u}_\xi$	Macroscopic velocity of the ξ^{th} component
v	Mean velocity
V	Volume
We	Weber number
x	Distance
γ	Interfacial tension
ΔP_{cap}	Capillary pressure
Δt	Time step
η, μ	Viscosity
κ	Local mean curvature
μ	Dynamic viscosity of liquid
ξ	ξ^{th} component
ρ	Density of fluid
ρ_ξ	Macroscopic density of the ξ^{th} component
σ	Standard deviation
τ_ξ	Relaxation time of the ξ^{th} component
ϕ	Concentration
Φ_n	Normal mass flux
ω_a	Weighting factor in the a^{th} direction

1 INTRODUCTION

In 2010 there were approximately 600,000 patients treated for End-stage Renal Disease (ESRD) in the United States and approximately 2.2 million cases worldwide, with the number of cases continuing to grow each year.[1] Compound this with limited kidney transplants, and an insufficient hemodialysis treatment method due to decreased survival rates and increased associated costs, and it becomes crucial that we arrive at a better solution for treating ESRD. Microchannel-based hemodialysis is one proposed option, already shown to have improved filtration performance characteristics over conventional hemodialysis. It has the potential to greatly improve the quality of life for patients but before microchannel hemodialysis is utilized in patient homes, there are still important challenges that must be overcome.

1.1 Renal Disease

The kidneys are associated with renal function and are responsible for various regulatory roles within our bodies.[2] They perform homeostatic regulation of the water and ion content of the blood, assist in regulating pH by removing or conserving H^+ and bicarbonate (HCO_3^-), and removing metabolic waste products and foreign molecules such as drugs and toxins. Examples of waste products include creatinine, urea, uric acid, urobilinogen (giving urine its yellow color), and hormones. The human body contains two kidneys each approximately the size of a balled up fist but the functional units of the kidney, nephrons (Figure 1), are microscopic tubules surrounded by peritubular blood capillaries. An individual kidney can filter 90 L of blood per day and generate only 1 L of urine. The volume of fluid that is filtered through the kidneys is the glomerular filtration rate (GFR). A health kidney has a GFR of 90 ml/min/1.73 m^2 or approximately 180 L/day and with a total plasma volume of 3 liters.[3] This equates to the kidneys filtering our entire plasma volume 60 times each day or once every 24 minutes!

Chronic kidney disease (CKD) is the progressive loss of renal function over the course of months or years.[4] Individuals at higher risk of CKD are those with

high blood pressure or diabetes. CKD is also associated with cardiovascular disease, anemia, and pericarditis.[5] Professional guidelines classify the severity of CKD into five incremental stages: stage 1 is slightly diminished renal function (GFR ≥ 90 ml/min/1.73 m^2 but there are other signs of disease such as proteinuria, polycystic kidney disease, and abnormal kidney structure), stages 2-4 are associated with further decreases in GFR and stage 5 is established kidney failure or end stage renal disease (ESRD) (GFR < 15 ml/min/1.73 m^2).

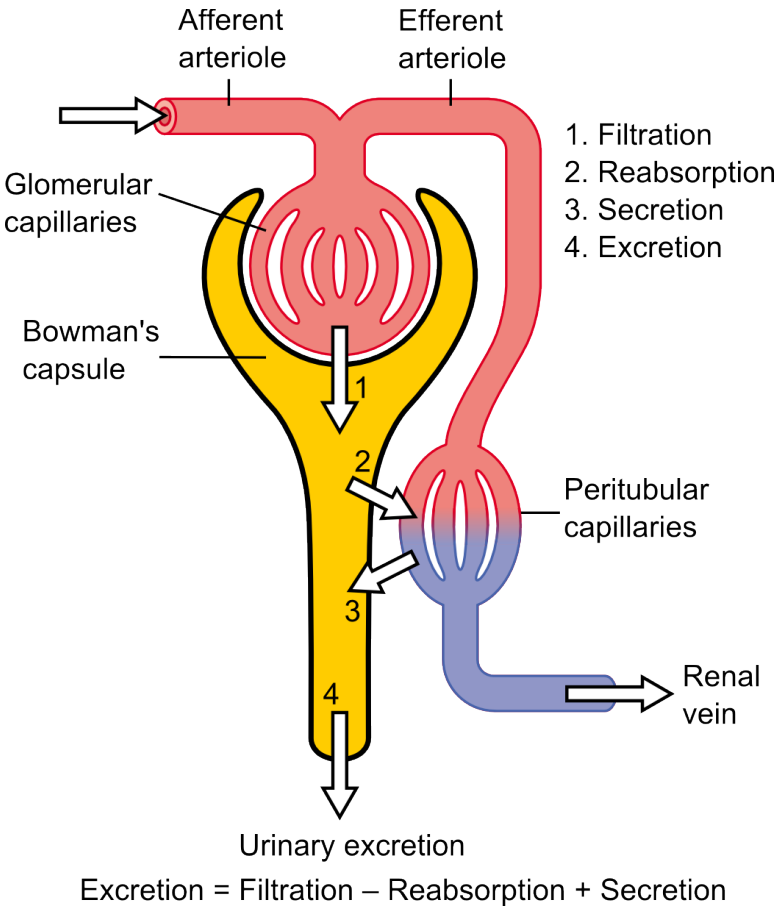

Figure 1. Schematic of the nephron: the functional unit of the kidney. Blood solutes are removed in the glomerular capillaries and some of the removed product reenters the blood stream via the peritubular capillaries.
Source: http://commons.wikimedia.org/wiki/File:Physiology_of_Nephron.png

1.2 Hemodialysis and Other Treatment Modalities

ESRD patients require renal replacement therapy, the two most common therapies being hemodialysis and kidney transplantation. The limited number of kidney transplants available, along with restrictions on viable candidates and wait times result in most patients relying solely on hemodialysis, with almost all patients at some point utilizing it. Hemodialysis has associated shortcomings. Current methods fall short in mimicking the continuous function of our kidneys, instead treating the patient in periodic intense filtration sessions, approximately three times per week. This is a product of the current approach to hemodialysis, which utilizes a hollow-fiber tube and shell filtration cartridge. We can see from Figure 2 that the majority of ESRD patients treated by various dialysis modalities rely primarily on in-center hemodialysis, with in-home hemodialysis only accounting for approximately 1% of dialysis treatments. Previous studies have shown that in-home, long duration dialysis is a superior treatment method for ESRD patients by better mimicking the filtration rates of healthy kidneys and better stabilizing blood solute concentrations and may even reverse the effects from short duration hemodialysis.[6]–[8]

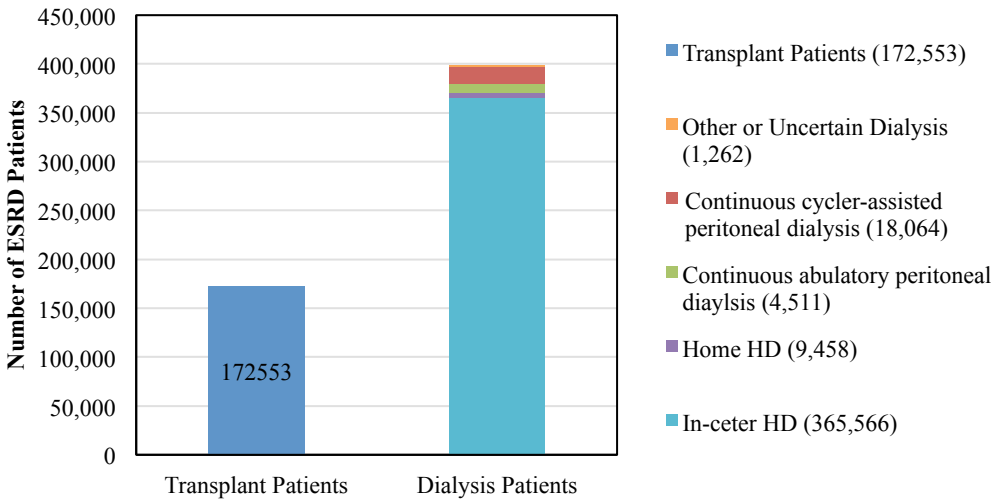

Figure 2. Breakdown of number of ESRD patients treated by various modalities in the U.S.

In Figure 3, the survival rates for patients undergoing dialysis and transplant are shown over the course of 5 years. We can see that with progressive years, dialysis patients show a stronger decrease in survival rates. Additionally, Figure 4 shows that

the associated cost per patient undergoing hemodialysis is over twice the costs associated with transplantation. This places additional stress on an already overburdened medical system. Understandably, with the higher population of ESRD patients receiving dialysis treatment, the U.S., total patient costs for dialysis ($1.7 billion) are 5.3 times higher than transplant recipients ($320K). When considering per patient per year costs, dialysis is still higher than transplant ($8,003 vs. $6,459). Additionally, these values do not reflect the reality that dialysis is a reoccurring cost for a dialysis patient each year. All of this information points to a need for a better solution to current hemodialysis especially when it is the primary method of treating ESRD.

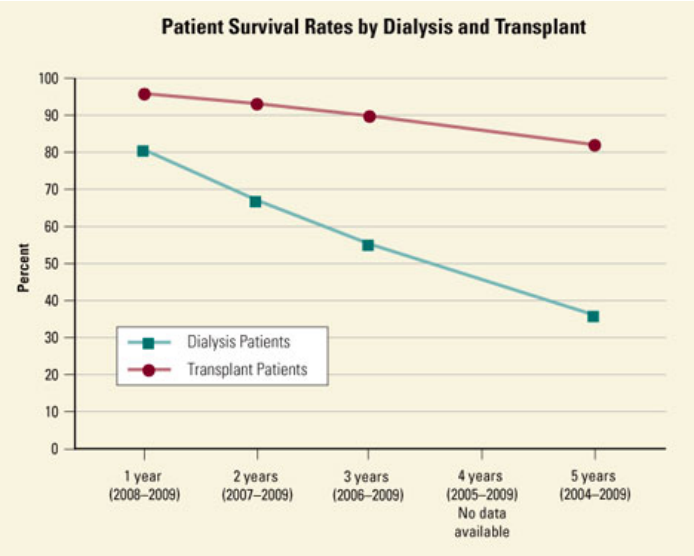

Figure 3. Patient survival rates by dialysis and transplant in the U.S. ***Source: National Kidney and Urologic Disease Information Clearinghouse, NIH***

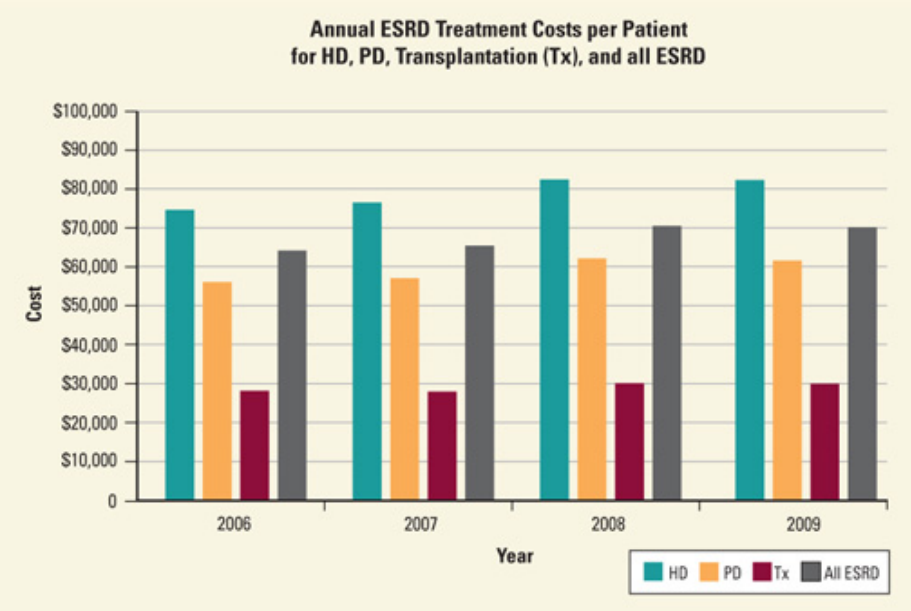

Figure 4. Annual ESRD treatment costs per patient in the U.S. ***Source: National Kidney and Urologic Disease Information Clearinghouse, NIH***

1.2 Microchannel Hemodialysis

Implementation of microchannel technology for hemodialysis may improve filtration performance and reduce dialysate waste, resulting in smaller hardware systems and potential in-home, daily, nocturnal application. This approach to treatment may increase survival rates and significantly improve the quality of life for end-stage renal disease (ESRD) patients [7], [8]. A general microchannel configuration for hemodialysis is show in Figure 5 where an array of microchannels carry blood countercurrent to an array of channels carrying dialysate with the sets of channels separated by dialysis membrane. The key benefit of microchannel hemodialyzers over traditional hollow-fiber hemodialyzers is the control of both blood and dialysate fluid flow at micro-scale level. In previous research, microchannel-based dialysis resulted in a 60% increased mass transfer coefficient compared to hollow-fiber devices [9].

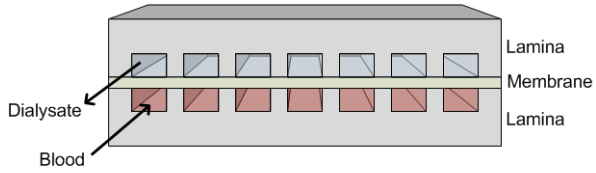

Figure 5. General configuration of microchannel hemodialyzer laminae

The advantages of controlling chemical processes at the microscale level have been understood for many years, based on transport phenomena principles, but the application of this knowledge was limited mostly by fabrication abilities. With the rise of integrated circuits came the development of better tools and methods for micro-scale fabrication and this opened up the potential to truly optimize chemical processing systems at the micro-scale level.

Microchannel systems intensify chemical operations (e.g. chemical reactions, molecular filtration) by decreasing the working distance of molecular species within the unit, minimizing heat and mass transfer resistance.[10] At micro-scale distances, molecular diffusion dominates over convective mixing, increasing favorable molecular collisions or with regards to hemodialysis, transport of species across a membrane. Hollow-fiber systems operate at the micro-scale in the blood side compartment in a slightly uncontrolled manner feeding blood into a cluster of unsupported hollow fibers and do not operate at the micro-scale for dialysate compartment. The ability to have micro-scale control over both blood and dialysate in microchannel hemodialysis is a key distinction between the two methods. With hollow-fiber dialysis, dialysate fluid is violently flushed through the shell side of the filtration unit resulting in high volumes of dialysate waste, making home application impractical considering the necessary resources associated with the process. Previous work by Tuhy and colleagues has shown microchannel-based hemodialysis to have improved filtration perfomance over traditional devices which may allow for decreased dialysate waste production.[9]

Operating at the micro-scale presents a multiphase problem of gas bubble blockage. The bubbles arise during normal setup and operation of the device and are

present in hollow-fiber systems as well, although they are mostly ignored in the filter itself. The bubbles enter the microchannel system and become lodged within the channels and manifold. These bubbles then obstruct flow, reducing filtration surface area and disturbing flow distribution through the channel array. These effects result in decreased filtration performance and potential blood damage due to high shear zones created around bubbles. Increasing flow velocity can flush out bubbles from the system but is not an option for this application due to increased potential to damage blood cells and decreasing filtration performance.[11] The primary approaches to processing bubbles through the microchannel system are 1) alter the interfacial energies between channel surface, gas bubble, and liquid and 2) optimizing microchannel geometries and manifold design to facilitate bubble movement.

Various surface treatments can be utilized in medical devices to reduce protein fouling and deliver therapeutic molecules. In our previous work, the polycarbonate microchannel surfaces were treated with a triblock copolymer of polyethylene oxide – polybutadiene – polyethylene oxide (PEO-PBD-PEO), creating a freely mobile PEO brush-layer that carries energetic properties similar to water.[12] This decreases the driving force for protein to adsorb to the microchannel surface. The PEO brush-layer can also be 'loaded' and end-group tethered with therapeutic molecules[13], [14]. Finally, with respect to bubble management, this PEO bursh-layer, operating similarly to protein repulsion, may facilitate bubble movement through the device by decreasing the affinity between bubble and channel wall as the microchannel surface now looks energetically similar to the liquid phase.

This research was funded by NBIB grant no.RO1EB011567. The primary focus of this grant was to investigate methods for bubble management within microchannel hemodialysis devices. In order to do so, we require an analytical tool to characterize hydrodynamic behavior within the device. This tool would work in conjunction with imaging techniques (shadowgraphy and tracer imaging) along with numerical simulations (finite element analysis and lattice boltzmann modeling) that were also developed in parallel during this work.

Residence time distribution (RTD) analysis is proposed as a method of characterizing microchannel/header geometries, detection and characterization of

two-phase [gas-liquid] flow in the microchannel-based hemodialysis units, along with fabrication defects that may exist in the device. RTD has been utilized in the chemical reactor field to characterize the hydrodynamic behavior within a reactor or fluid flow system. These larger systems are more conducive for collecting necessary data and many reactor goemeteries have associated analytical solutions. The application of RTD in the microfluidic field has been investigated by various groups over the last 10 years. Yet this remains a relatively new application and much more work is necessary to begin to understand the potential utility of this approach.

2 RESEARCH GOALS AND OBJECTIVES

2.1 Research Goals

The goal of my research is to characterize fluid age within microchannel hemodialysis devices using residence time distribution analysis. A secondary goal is to determine the sensitivity of RTD analysis for use in detecting device defects commonly associated with two-phase flow problems such as channel obstruction due to bubbles. A third goal is to determine the utility of PEO-coatings for decreasing bubble stagnation in microchannel devices.

2.2 Objectives

The following were objectives necessary to meet the research goals:

1. Develop microchannel lamina “test articles” and device enclosure.
2. Construct and validate RTD test loop for measuring inlet-outlet concentration profiles.
3. Collect experimental pulse response data for relevant systems and flow scenarios.
4. Collect experimental data for bubble blockage levels in PEO-coated vs uncoated systems.
5. Develop deconvolution methods for obtaining RTD profiles and generate RTD profiles from experimental data.
6. Run in conjunction, numerical simulations of equivalent systems and flow scenarios and validate numerical simulations using experimental RTD data.
7. Determine the sensitivity and applicability of RTD in microchannel hemodialysis applications by sequentially decreasing the flow maldistribution within test articles.

2.3 Contribution Science

This research focuses on the development, validation, and critique of residence time distribution analysis for application in characterization of microchannel hemodialysis devices, a technology that has the potential to improve the

quality of life for many ESRD patients. There are two contributions to science that will emerge from this work.

The first scientific contribution is the development of a non-visual analytical tool for microchannel hemodialysis systems utilizing residence time distribution analysis. This work focuses on development of a hemodialysis device but RTD could be utilized in many different areas to characterize fluid age within devices and as a means to validate numerical models. Although RTD analysis has been applied to microchannel systems, in most previous cases, these were systems that required direct visual access to the microchannels and less complex microchannels devices. In this work, we investigate a method that would allow characterization of multilayer and/or non-transparent systems (i.e. stainless steel reactors).

The second contribution to science is to add to the current body of knowledge on microchannel flow by developing RTDs for flow through complex geometries not previously investigated. This research will investigate flow maldistribution in microchannel geometries and develop conclusions on the various effects associated with fluid age and mixing.

3 LITERATURE REVIEW

3.1 Microchannel Technology

Microchannel technology is the operation of chemical processes within systems whose geometries are measured in the 1-1000 micron range. Originally utilized for lab on a chip systems for high-speed detection or characterization of microliter sample volumes, new and potentially breakthrough work has been applied to continuous chemical processing systems.

Microchannels are optimized to carry out chemical processes, whether they are reactions or separations, by minimizing the mass and heat transfer lengths for species within the system for short processing times in the absence of mixing mechanisms. Figure 6 shows three basic configurations for chemical reaction and separation in microchannel systems. Microreactor is a term for microchannel systems for carrying out chemical reactions but the term is often loosely associated with any geometry for various microchannel chemical processes.

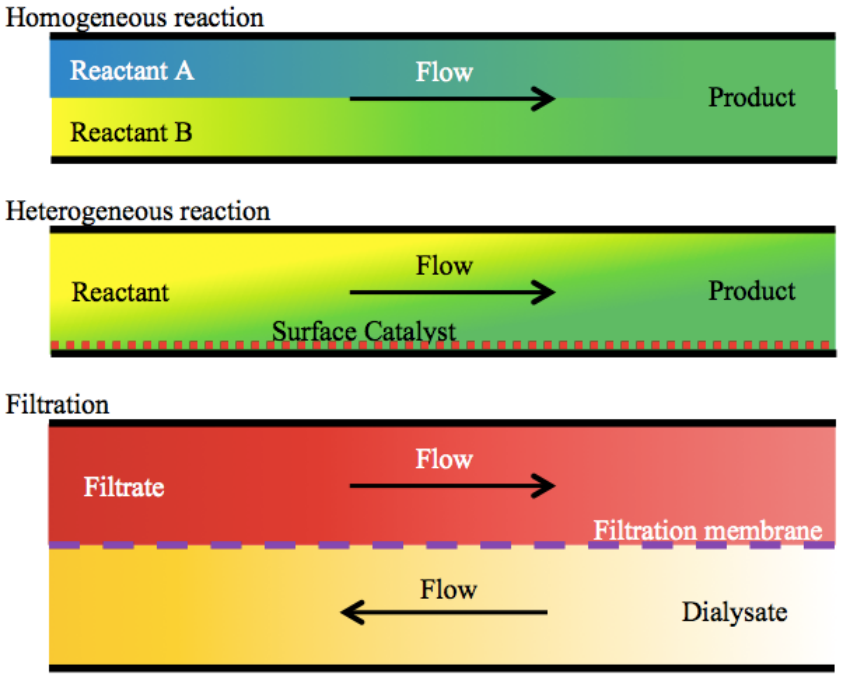

Figure 6. Example schematics of microchannel chemical process as viewed from the longitudinal cross-section of a single channel.

Mass transfer within a thermodynamically stabile system follows Fick's law of diffusion, and heat transfer follows the equivalent Fourier's law of heat conduction.[15] Equation 1 is Fick's second law, relating mass flux to spatial concentration gradients with concentration (C), time (t), and distance (x).

$$\frac{\partial C}{\partial t} = D\frac{\partial^2 C}{\partial x^2} \qquad \text{Equation 1}$$

We can see from this equation that time is related to distance to the second power. This tells us that maintaining all else (i.e. diffusion constant), decreasing diffusion distance by a factor 'n' decreases diffusion time by n^2. It shows the strong relationship between the two variables and it is the reason why at larger distances the time for diffusional mass transfer becomes prohibitively long and at short enough distances becomes near instantaneous, on the order of milliseconds. Most diffusion coefficients for solutes within a liquid are on the order of magnitude 10^{-9} m^2/s This equates to 'diffusion times' of approximately 10 seconds for distances of 100 microns and this is the primary reason it is of great research interest to design chemical systems on the micro-scale.

Liquid solutions flowing through a microchannel are able to quickly mix chemical reagents and transport molecules to heterogeneous catalyst on the channel surface for reaction or to a dialysis membrane where the concentration gradient across the membrane will continue the transport process for filtration. This enhanced mass transport time eliminates the need for separate mixing mechanisms found in traditional systems as no mixing methods could achieve similar mass transfer rates and, additionally, those other mixing methods are more energy intensive. Everything that has been discussed for the mass transfer can be applied to optimizing microchannel systems for heat conduction. For chemical process systems that require precise temperature control of reactants and/or products, the ability to reach optimum temperature quickly allows for localized temperature control throughout the microchannel system. This could assist in promoting a preferred reaction pathway by minimizing side products and degradation but also may open up new synthesis and processing opportunities via rapid heating and quench cooling. For example,

researchers have synthesized amorphous cobalt and cobalt samarium nanoparticles via elevated reaction temperatures followed by rapid quenching of colloids in a microreactor.[16], [17]

Additionally, another benefit of microchannel systems is the ability to optimize fluid flow to a precise level by operating in the laminar flow regime, allowing for more complete modeling and optimization of the system. This is based on satisfying Reynolds number (*Re*) criteria for laminar flow (*Re* < 2100).[15] The equation for Reynolds number is given in Equation 2 where ρ is the fluid density (kg/m^3), v is the mean velocity (m/s), D_H is the hydraulic diameter (m), and μ is the dynamic viscosity (N·s/m^2).

$$Re = \frac{\rho v D_H}{\mu} \qquad \text{Equation 2}$$

If we insert typical values for microchannel systems, the density and viscosity of water at 25°C (1000 kg/m^3 and 0.001 kg/s-m), a hydraulic diameter of 100 μm and fluid velocity of 1 cm/s, the *Re* is 1 within the channel, well within the laminar regime that even with different fluids and flow velocities the flow will still remain laminar. While laminar flow characteristics exist in the microchannel, there are exceptions to what is considered the standard boundary conditions, specifically the no-slip assumption, when dealing with certain material-liquid combinations. This discussion will continue in the Section 3.2.

Previous Master's work by Alana Warner-Tuhy and Eric Anderson has shown improved filtration performance in microchannel dialysis over conventional hollow-fiber dialysis. Microchannel hemodialysis systems were fabricated and filtration performance was measured for 'blood' side removal of urea and creatinine. The microchannel system has a mass transfer coefficients ranging from 0.068 to 0.14 for a range of average velocities (1.0 – 5.0 [cm/s]) and the mass transfer coefficient was predicted to 0.08 cm/min. The microchannel system outperforms commercial dialyzers that typically have a mass transfer coefficient of 0.05 cm/min and the numerical simulation created accurately models the microchannel system,

emphasizing previously the associated performance benefits of microreactor systems and that fluid behavior in these systems can be accurately predicted.[18], [19]

3.2 Two-phase flow

Two-phase flow refers to both gas-liquid and immiscible liquid-liquid flow. Gas-liquid flow will result in bubbles if the minor fluid is gas and droplets if the minor fluid is liquid. Immiscible liquid-liquid flow will result in droplets in the case of either liquid being the minor fluid. And in both cases, thin films can arise under sufficiently high shear rates or similar fluid viscosities and/or similar flow rates. There are various flow patterns predicted for two phase flow at different ranges of conditions. These conditions are gas/liquid flow rate ratio, reactor design/dimensions, and inlet design, along with others.[20] The Capillary number (*Ca*) (Equation 3), Weber number (*We*) (Equation 4), and previously discussed Reynolds number are all used to identify which flow pattern may be present in the microchannel system. Capillary number describes the relative effect of viscous forces versus surface tension forces and Weber number describes the relative effect of inertia forces versus surface tension forces. Figure 7 is a chart that visually describes two-phase flow patterns based on which forces dominate within the system.

$$Ca = \frac{\mu v}{\gamma} \qquad \text{Equation 3}$$

$$We = \frac{\rho v^2 l}{\gamma} \qquad \text{Equation 4}$$

For systems in which surface tension forces dominate, bubbly, and slug-bubbly flow exists when the liquid flow rate is higher than the gas flow rate. Slug/Taylor flow exists when gas flow rate is larger than liquid flow rate in surface tension dominant systems. In the transition region between surface tension dominant and inertia dominant systems, either churn flow or slug-annular flow will arise until inertial forces fully dominate and then parallel/annular flow exists.[20]–[22] These different flow patterns are described visually in Figure 8.

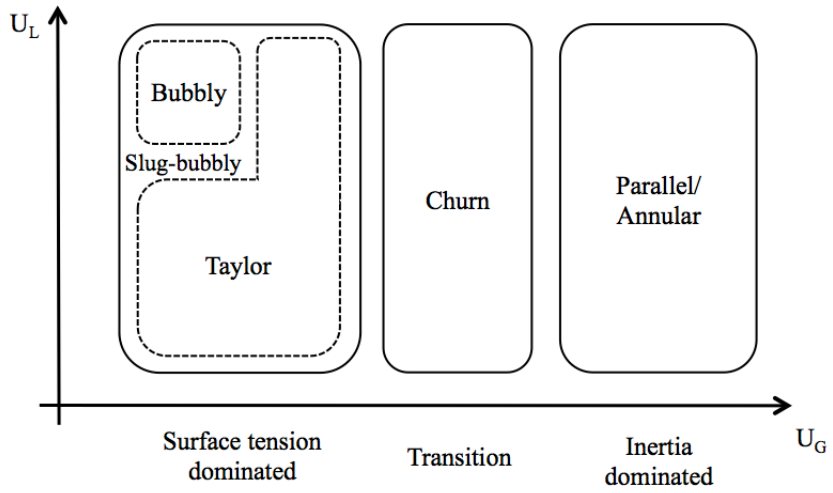

Figure 7. General flow hydrodynamics map in microscale systems [20], [21]

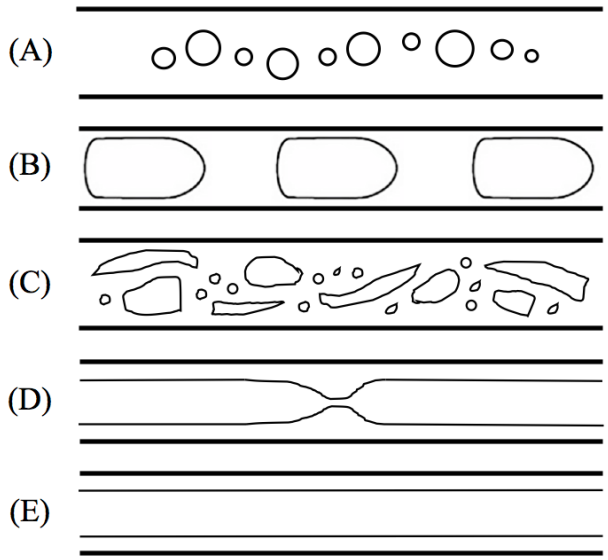

Figure 8. Flow regimes in microchannel [37][38] : (a) Bubbly flow, (b)Slug/Taylor flow (c) Churn Flow (d)Slug/Annular flow (e)Annular flow. [20]–[22]

Two-phase flow is often a necessary characteristic of the system, such as with chemical microreactors that require a gas that cannot be dissolved sufficiently in the liquid as a reagent. An additional phase can be added to the single-phase systems to reduce the inherent broad diffusion bands associated with a laminar flow profile. It can also be an unfortunate consequence of normal operation of a single-phase system. With microchannel hemodialysis, what should be a single-phase system is often

interrupted by the presence of air bubbles that enter the system via the priming process or from dissolved gases in blood.[11]

Two-phase flow encountered in hemodialysis is primarily bubble flow or slug flow due to the lower flow rates and strong surface tension forces between air, dialysate, blood, and device material. Bubble flow within a capillary tube has been investigated under a variety of conditions and various models have been proposed to explain flow behavior. In the last ten years, research in bubble behavior within rectangular microchannels has increased as a result of the growing interest in microchannel technology. Before discussing further two-phase flow, studies examining single-phase behavior will be reviewed. Flow behavior within microchannels can mostly be assumed laminar, although the common boundary condition of no-slip at the channel surface has been shown to be inaccurate under certain conditions.

In work by Choi and colleagues, slip behavior of water was investigated in hydrophilic and hydrophobic microchannels of 1 and 2 μm depth and 500 μm width.[23] Flow rates were measured under various pressure differences across the microchannel and difference in experimental values and theoretical expectations is accounted for by modifying slip conditions within the model. Under hydrophilic conditions, N-type silicon etched using reactive ion etching and RCA-1 cleaned to leave a native oxide layer, there may be slip conditions present based on subtle trends in the data but lack of sensitivity in measurements and control of surface smoothness leaves only uncertain conclusions. For hydrophobic surfaces, the same N-type silicon wafers etched by reactive ion etching and coated with octadecyltrichlorosilane (OTS), the slip behavior is more apparent. Figure 9 shows the shape of the meniscus in hydrophilic and hydrophobic channels in their study. Slip length was approximately linear with respect to shear rate with an approximate value of 30 nm for a shear rate of 10^5 s^{-1} (see Figure 10).

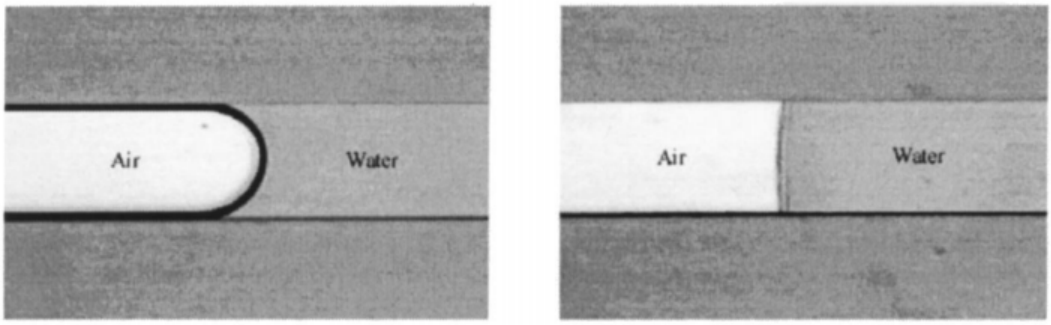

Figure 9. Meniscus shape for the RCA-1 cleaned hydrophilic channel (left) and the OTS-coated hydrophobic channel (right). ***Source: Choi et al., 2003***

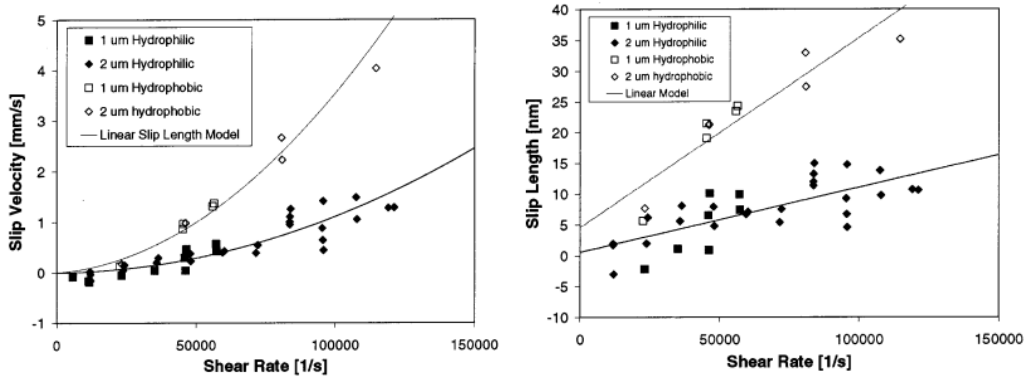

Figure 10. Slip velocity and associated slip length for pure DI water versus rate of shear. The data analysis allows for slip over both the hydrophilic and hydrophobic surfaces. ***Source: Choi et al., 2003***

Zhu and Granick investigated slip behavior in three systems: (i) tetradecane against adsorbed surfactant; (ii) tetradecane against a methyl-terminated self-assembled monolayer (SAM); and (iii) water against methyl-terminated SAM.[24] In all three cases, the classical no-slip boundary condition failed to predict the decreased hydrodynamic forces measured experimentally. It was observed that associated partial slip increased with increasing flow rate through the channel and eventually reached 2-4 orders of magnitude less hydrodynamic force in partially wetted systems compared to the expected force using no-slip boundary conditions. Although contact angle varied largely between the three groups, increasing with respect to the same order listed above, the authors cannot state with certainty whether this is a primary factor in slip behavior due to the additional presence of variance in surface roughness.

Bonaccurso and colleagues found that for a Newtonian fluid in a completely wetting system (advancing contact angle of 0°) in the absence of a polymer coating, the degree of slip increases with surface roughness.[25] They make an important note

that in the case of polymer coatings where the chains protrude into the solution, the plane of shear is shifting into the solution, resulting in a negative slip length and which is a reason why their rough surface behaves differently from previous studies investigating surface roughness but employing polymer coatings. While the surface they use is wetting, encouraging interaction between channel wall and liquid, the scale of the roughness is large with respect to the fluid molecule. From the assumption that most real world systems exhibit this scale of roughness, the authors conclude that in most practical situations, boundary slip occurs and leads to a reduction in drainage force.

It has been show in these studies and in others that slip conditions do arise in microchannel flow and result in a decreased pressure drop across the system. [26]–[28] This will affect the velocity profile within the channel and may be observed in RTD measurements by reduced dispersion as the flow profile approaches plug flow in the most extreme case. Additionally, slip must be considered when developing numerical models and when describing two-phase flow behavior.

Under steady flow conditions and negligible gravitational acceleration and temperature gradients, two fluid phases reach equilibrium when the pressures in both phases are uniform and differ only by the capillary pressure given by the Young-Laplace equation (Equation 5) where γ is the interfacial tension and κ is the local mean curvature at the interface.[29]

$$\Delta P_{cap} = \gamma\kappa \qquad \text{Equation 5}$$

Solid surfaces are most often characterized by their roughness and wetting behavior, determined by the contact angle. When two immiscible fluid phases interact with a solid surface the three phases can intersect at a contact line or a thin film can be formed by one of the fluids as shown in Figure 11B. As with the capillary pressure, this contact angle is related to the interfacial tensions between the three phases and is described by Young's equation (Equation 6) where 1 refers to fluid 1, 2 refers to fluid 2 and S refers to the solid.

$$\gamma_{12} \cos\theta = \gamma_{1S} - \gamma_{2S}$$ Equation 6

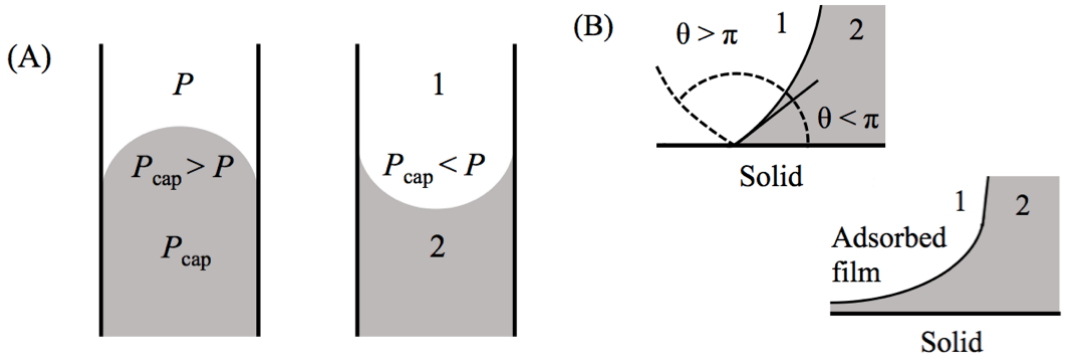

Figure 11. (A) The curvature is related to the differences in capillary pressure and ambient pressure.[30] (B) The configuration of three phases, one where the three phases intersect at a contact line and another where a thin-film form between the solid and the other fluid phase.[31] ***Adapted from V. Hessel et al., 2009***

In work by Fuerstman and colleagues, the pressure drop along rectangular microchannels containing bubbles was investigated.[32] For solutions containing no surfactant to <0.1 critical micelle concentration (CMC), the pressure drop along the channel was primarily dependent on the number of bubbles in the channel. At very high concentrations of surfactant, >100 CMC for Tween-20 and 10 CMC for SDS, the pressure drops were still primarily dependent on the number of bubbles in the channel. Interesting behavior arose at intermediate concentrations of surfactant as the total length of bubbles in the channel became the dominant contributor to pressure drop. It was observed that the shift to bubble length is also accompanied by an increase in flow of liquid through the "gutters" of the channel.

Cubaud and Ho investigated two phase flow in microchannels under various flow regimes (bubbly, wedging, slug, annular, and dry) created by varying the liquid fraction between liquid and gas.[33] They observed a thickening of film around the bubble as capillary number increased from 0.009 to 0.018. In partially wetting channels and when flow is primarily through the channel gutters or corners, local or global dry out can occur. Also, trends in slip behavior and bubble velocity remained consistent for the two square channel dimensions (200 and 525 microns), contrary to changes observed in larger channels.

Obstruction by gas bubbles is a common multiphase problem for liquid phase microscale-based devices. In hemodialysis, bubbles arise during normal setup and operation of the device and are present in all types of microchannel and hollow-fiber systems. Bubbles form in-device when dialysate fluid is heated during the dialysis process resulting in increased partial pressure of gases and when ultrafiltration control systems apply a negative pressure on the dialysate compartment to increase filtration [34]. Additionally, bubbles form in the blood compartment when the combination of high blood flow and small size needles create unsteady flow regions [35]. The presence of proteins in a blood stream stabilizes the bubble formation process. It is also postulated that gas could be transported from the dialysate fluid, across the dialysis membrane and into the blood compartment [34]. Ventilation valves, sudden changes in temperature, and negative pressure chambers are implemented to deaerate liquids and yet bubbles still persist in dialysis devices [34].

In a microchannel-based system, bubbles presence is a common challenge, becoming stationary within the channels and manifolds.[36]–[41] For microchannel-based dialysis, stationary bubbles reduce filtration surface area, creating stagnant regions, and disturbing designed flow distribution through the microchannel array. The consequences are decreased filtration performance and potential blood damage due to high shear zones created around bubbles or prolonged contact of a stagnant blood pool with the walls of the microdevice. Increasing flow velocity to purge bubbles is less feasible in hemodialysis due to a reduction in filtration rate and the potential to damage blood cells. Bubble traps are currently implemented in dialyser systems although they do not completely eliminate bubbles from entering the device nor do they impact bubble formation within the dialyzer. There is also motivation to minimize the use of bubble traps as they can promote clotting in heparin-free dialysis [34]. Our approach to counteract bubble obstruction is to improve mobility of bubbles passing through the device using surface modifications to alter the interfacial energies at the microchannel surface with the working liquid and gas bubble.

An understanding of the fluid dynamics in microchannel two-phase flow is necessary in order to understand the RTD behavior we expect to observe and to develop a proper numerical simulation of the relationships determining fluid behavior

and mass transfer within the device. For example, the studies discussed above show a variety of fluid flow conditions that may exist within a microchannel containing a bubble, even when the bubble is stationary. The film may move or remain stationary and there could be significant flow diverted to the gutters of the channel. These factors affect the RTD of the system as tracer may completely avoid a stationary channel or continue to flow around down the channel and around the bubble. There is a strong need for this proposed research as our understanding of two-phase fluid flow becomes increasingly clouded for a microchannel hemodialysis device which contains multichannel arrays, complex header designs, multiple laminae, and a complex fluid such as blood.

3.3 Polyethylene-oxide coatings

Various surface treatments can be applied to medical devices to reduce protein fouling as well as platelet adhesion and activation, and to deliver therapeutic molecules. In our previous work, the hydrophobic polycarbonate microchannel surfaces were treated with a triblock copolymer of polyethylene oxide – polybutadiene – polyethylene oxide (PEO-PB-PEO), creating a steric repulsive PEO brush-layer that masks the underlying polycarbonate from protein adsorption [42]. Theoretical and experimental evidence suggests that below the outer region of a PEO brush-layer there exists a hydrophobic, inner region that is favorable for protein adsorption [43], [44]. This is due to competitive interactions between solvent as well as proteins for the chain segments, and the ability of PEO to adopt higher order intra-chain structures. Thus the PEO brush-layer can also be 'loaded' with (sufficiently small) therapeutic peptides [45] as well as functionalized by chain end-activation and bioconjugation [13])

The PEO brush-layer is a complex coating. Lee et al. recently demonstrated that PEO chains are not hydrophilic when they are arranged in the polymer brush configuration[46]. They suggested that, at the high PEO chain concentrations consistent with brush formation, the specific configuration of the polymer that enables the hydrophilic interaction with water becomes disrupted, rendering the PEO

chain less soluble (or even insoluble) in water. Others groups have theoretically predicted [43], [47] and shown experimentally that beyond some threshold, PEO chain density the PEO brush would "collapse" owing to this effect [48]. While increasing chain density within a brush layer might eventually favor lateral compression, Lee et al. concluded that the widely observed, steric-repulsive character of PEO brushes is retained because the hydrophobicity of the brush (which favors compression) is not sufficient to overcome the opposing force of the chain conformational entropy (which resists collapse) [46].

With respect to bubble management, the PEO chains comprising the outer region lowers the interfacial energy between the microchannel surface and water which facilitates bubble movement through the device by maintaining a lubrication layer between the bubble and channel surface. Additionally, this PEO layer helps to mask surface defects such as burrs that are introduced during the microchannel lamina fabrication process. In our model, a two-phase system of water and air, the effects of the coating are most noticeable through the reduced contact angles resulting from the hydrated outer layer of the PEO coating [42]. The dynamics occurring at the hydrophobic inner layer play a lesser role for this study. Figure 1 illustrates the interaction of a bubble with various types of solid surfaces, the third scenario (C) being the PEO brush layer. The complex nature of the PEO brush layer will become even more significant when the coating is utilized in the presence of blood, which contains cells, proteins, and other constituents that will interact with the brush layer.

This investigation presents the effects of coating polycarbonate surfaces with a PEO brush-layer for managing gas bubble obstruction in a model air-water two phase flow through a microchannel array (microchannel dialyzer in our previous study [6]). In parallel, progress is made in the development of a numerical model, by Agnieszka Truszkowska, using Lattice-Boltzmann modeling approach that can properly simulate bubble-fluid-wall interaction, including behavior in a PEO coated microchannel. The simulation work uses contact angle as a "macroscopic" representation of phenomena occurring on microchannel walls, displaying the role of a thin liquid film surrounding the bubble on bubble mobility in a single microchannel.

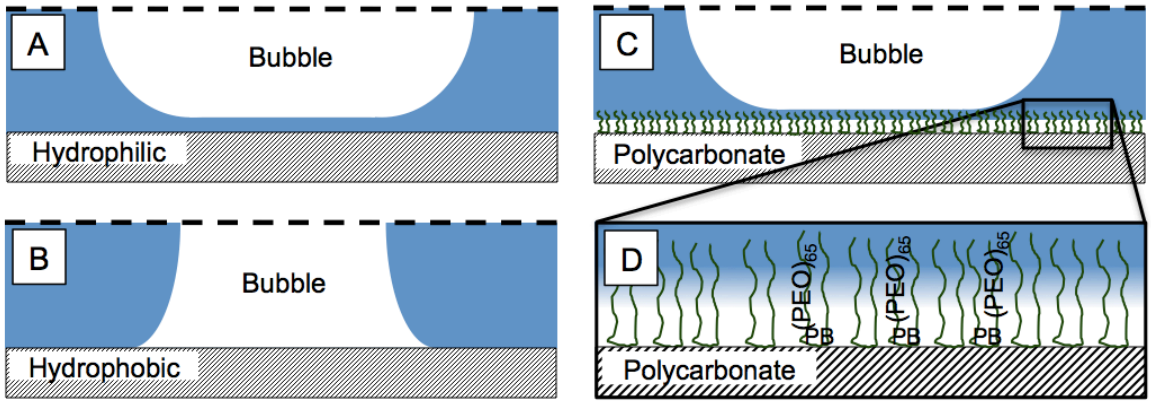

Figure 12. Illustration of bubble interaction with various microchannel surfaces: (A) thin water film formed between bubble and smooth hydrophilic surface, (B) bubble in direct contact with hydrophobic surface in water, (C) bubble repulsed from solid surface by the PEO chains creating a hydrated, steric barrier and (D) orientation of PEO-PB-PEO triblock polymer chain on a treated polycarbonate surface. Objects in the image such as the triblock brush layer in a microchannel are not drawn to scale. Dashed lines represent a line of symmetry across microchannel.

3.3 Residence Time Distribution Theory

Residence time distribution (RTD) analysis is a standard method for characterizing hydrodynamic behavior of flow systems. The residence time distribution describes the fluid age of a particular system.[49] It is used to determine if there are dead or stagnant flow regions, channeling or bypassing of fluid, recirculation of fluid, and develop and/or verify flow models.[50] The system under investigation could be as large as a river or as small as a blood capillary. Residence time distribution analysis has been used widely in chemical engineering on large reactors and only more recently on microscale systems. In our application, the system is the complete hemodialyzer: header regions, microchannel arrays, and connections.

The main principle for RTDs is that given a volume of fluid entering a system at time, t_0, that volume can be partitioned into smaller volumes that exit the system after t_0. Collectively, these partitions create a distribution, the residence time distribution, that can be plotted as mass fraction versus time. When described as a density function, the RTD is often denoted as $E(t')$. The moments of the distribution can be calculated, such as the first moment (mean), second moment (variance), third moment (skewness), and fourth moment (kurtosis or peakedness). The first and

second moments are particularly useful in anaylsi, as they describe the average age of the fluid exiting the system and variation of fluid age or dispersion.

Residence time theory applies to any conserved material in your system. Typical conserved materials include molecules, colloieds, Brownian particles.[51] The starting assumptions for a system are:

1. Steady state flow.
2. A single inlet and outlet.
3. The inlet and outlet are closed, flow across the system boundaries are unidirectional.
4. Homogeneous system.
5. Inert tracer can be used for experiments, does not disturb flow.
6. Isothermal.

As the field has progressed, new understanding and techniques have been developed that allow for relaxation of some assumptions. For example, tracer studies have been performed in environmental engineering applications were there may be multiple streams or outlet sources to measure.

Residence time theory is primary based around the convolution integral (Equation 7). The convolution integral involves redistributing an input $b(t\text{-}t')$ over a system response function $g(t')$ to arrive at the output $a(t)$. The system response is a function of t' which is not that absolute time but a relative time with respect to when a particular volume of tracer enters the system.

$$a(t) = \int_{-\infty}^{\infty} b(t - t')g(t')dt' \qquad \text{Equation 7}$$

The RTD is the system response funtion, $E(t') = g(t')$, and is related to the mixing and dispersion within a sytem. For example, a system with large dispersion will have a wide system function and a system with plug flow will have a sharp system function similar to or approaching a Dirac delta function. In the later case, the output response will look almost identital to the input response with only a shift in absolute time that is dependent on the location of the dirac delta on the t' time scale.

One simple way of conceptualizing the residence time distirbution is by looking at a special form of the distribution: the washout function, $W(t)$. Imagine your system with an inlet stream containing a salt concentration of zero and fixed flowrate. At time $t = 0$, the inlet stream is switched instantaneously and without disturbing the flow to a stream containing a salt concentration of 1 and the same previous flowrate. One could measure the outlet concentration of salt starting at $t = 0$ and a plot would follow some shape from zero to eventually 1 as all the 'old' fluid is replaced by the salt solution. If we were to take the derivative of this outlet concentration function with respect to time, we would arrive at the residence tim distribution. [49]

The behavior of the tracer patricle can be governed by multple sources such as convection, dispersion, molecular diffusion, and even electromagnetic fields, depending on conditions. A highly developed field of residence time theory is analysis of laminar flow through pipes. By calculating the Bodenstein number (Bo), one can use a map (see Figure 13) to determine which regime the system operates in and the appropriate relationship to use to develop the RTD. The Bo is a ratio of total momentum transfer to molecular mass transfer. From Figure 13, we see four major regimes: pure convection, pure diffusion, dispersion, and an intermediate regime.

Pure convection describes a system where movement of material is dictacted by convective forces and diffusion effects and back-mixing are nonexistant or neglible. Therefore in a laminar system, the shearing layers slide past each other without transfer of material. The RTD for pure convection of laminar flow through a tube is give by:

$$E(t') = \bar{t}^2/2t'^3 \quad \text{for} \quad t \geq \bar{t}/2 \ \text{ with } \ \bar{t} = V/Q \qquad \text{Equation 8}$$

Pure diffusion is on the opposite end of the spectrum when movement of material is solely dictated by diffusion.

The dispersion regime describes a system in which primary movement through the system is through convection but backmixing or diffusion can affect the concentration profile at the outlet. The axial dispersion model represents a system in which the primary source of transport is due to plug flow but axial or longitudinal

backmixing causes a variance in fluid age. At the macroscopic level, this backmixing could be partially attributed to turbulence variations (for applicable conditions) and general imperfections in fluid flow. It is described similarly to the diffusion coefficient *D* in Fick's law but with an analagous longitudinal dispersion coefficient **D**.[52] The resulting RTD is a more or less a gaussian distribution that is time shifted to reflect the average fluid age or mean residence time (MRT). Axial dispersion or diffusion in laminar system that are not plug flow (e.g. laminar flow through a tube) also results in increased broadening of the RTD profile, refered to as band broadening. Laminar flow in presence of radial diffusion but in the absense of axial dispersion/diffusion, results in reduced band broadening as the material samples a range of fluid moving radially and large differences in velocity at the center of the tube versus at the wall begin to approach an average.[53] Taylor-Aris dispersion describes the interaction between axial convection, axial diffusion, and radial diffusion to shape the age of fluid exiting the system.[54]

The fourth regime is an intermediate zone where neither of the three completely describe the fluid age of the system. It is recommended by Levenspiel that if presented with this case, solve for the two closest know regimes and expect a realistic result to exist somewhere between the solutions.[49] One of the challenges of larger complex microreactors is that the wide range in feature sizes spanning connection tubing, to headers, to microchannels, or even through porous layers can create the existance of multiple regimes within one device.

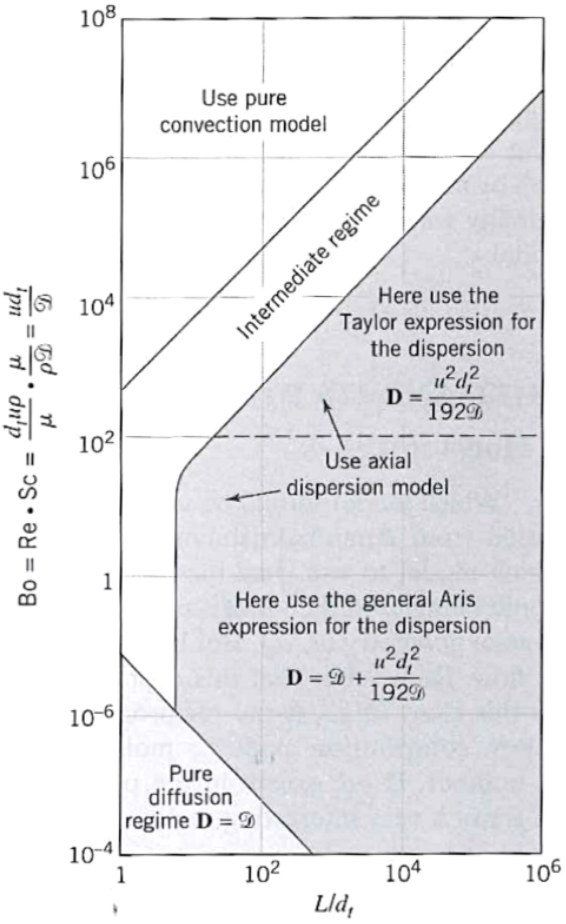

Figure 13. Map showing which flow model should be used for lamina flow through a tube. ***Source: Levenspiel, 1998.***

3.4 Pulse Response Measurement

Often, RTDs are developed by injecting a tracer solute into the system and measuring exit concentrations. The tracer can be salt as was used in the washout example from the previous section, in which conductance can be measured. It can also be a dye molecule, in which absorbance or flourescence is measured. Another method is injecting microspheres for particle tracking within the system or at the outlet using a particle image velocimetry (PIV) camera system.

With larger systems, the injection of tracer can be almost instantaneous or associated with a single time point (t_0) and the resulting outlet concentration curve is assumed to be the RTD. For our system and nearly all microscale systems, creating a near perfect pulse is virtually impossible due to the instant shear gradiants the pulse

encounters in the laminar fluid flow. Instead, the result is an input and output concentration profile or response profile. In order to arrive at the RTD, output response profile must be deconvoluted from the input profile. Regardless of the technique used to quantify tracer concentration at the inlet and outlet, certain criteria must be satisfied in order to confidently trust that previously listed assumptions are true and that the pulse response measurement will reveal the RTD.

One way to view the inlet and outlet concentration measurements are as two outlet measurements taken at different distances downstream from the tracer injection location. A flux measurement, also refered to as the mixing cup measurement, involves measuring the concentration of volume sample at the outlet that is well mixed and over a fixed time interval and therefore fixed volume. The total mass measured reflects the summation of spatial variations in mass flux at the outlet. This is the ideal approach assuming the sample interval is small enough to express all detail in the RTD profile because, theoretically, mass should be conserved through the system.

A planar measurement is the most common method for microfluidics because the low flowrates and small vessel volumes are not conducive to collecting discrete liquid samples for measurement. Instead, the planar measurement employs a through-the-wall technique such as placing a light souce on side of the outlet tube and and measuring absorbance level at a wavelength absorbed by a tracer dye on the direct opposite side of the tube. This method requires that concentration of tracer is nearly uniform in the radial cross-section that the measurement is taken. Because this measurement does not accurately reflect spatial variations in flux at the measurement, the mass balance may not close sufficiently in some case. There is a corrections for this discrepency found in Levenspiel's *Chemical Reaction Engineering*, but this for a circular pipe system.

3.5 RTD Analysis in Microreactors

We will examine various research in the field of RTD analysis in microreactor systems, including device geometry, measurement technique and model development.

Trachsel and colleagues developed a rather novel microfluidic system for measureing RTD through a single microchannel.[55] The tracer liquid is both stored and injected into the main stream and gas segmented into the main stream on the same microfluid plate allow for precises control of delivery into the system . Their residence times were on the order of several minutes for a serpentine channel design (400 μm wide and 115 μm deep) and chosen based on residence times used in various chemical microreactors. They determined the residence time distributions for single-phase liquid and segmented gas-liquid microflows, with RTD being significantly lower for the gas-liquid case.

Cantu-Perez and colleagues investigated residence time of a bare rectangular channel and one with herringbone structures to promote mixing.[56] The experimental results were also compared with numerical solutions employing coputational fluid dynamics and particle trakcing with random walk diffusion and they found good agreement between calculations and experiments for all of their cases. Their findings show that at low Peclet numbers, ($Pe < 100$), herringbone structures do not have a significant impact on RTD within a channel and at higher Peclet numbers, ($Pe > 100$), the channels with herringbone structures have a narrower RTD compared to a plain channel.

Cantu-perez published a more recent study in 2011 investigating RTD in microstructured reactors containing either straight channels or zig-zag channels.[57] The microchannel plates are shown below in Figure 14. The goal of this work was to examine RTD of systems that allowed for 3-dimensional flow variation. They were able to achieve good agreement between experimental data and numerical models (Figure 15). An LED-photodiode system was used for tracer measurement. Their findings show that as flow increased, RTD variation increased for all geometries. Single rectangular cross section channels had large variance compared to those with 3-dimensional flow but not much larger when considering the hydraulic diameter was 4 times larger and they attribute this to the low aspect ratio of the channel (wide and shallow). Although RTD variance increased for all structures with increasing flowrate, the change was smallest for the microstructured systems and specifically the zig-zag configuration.

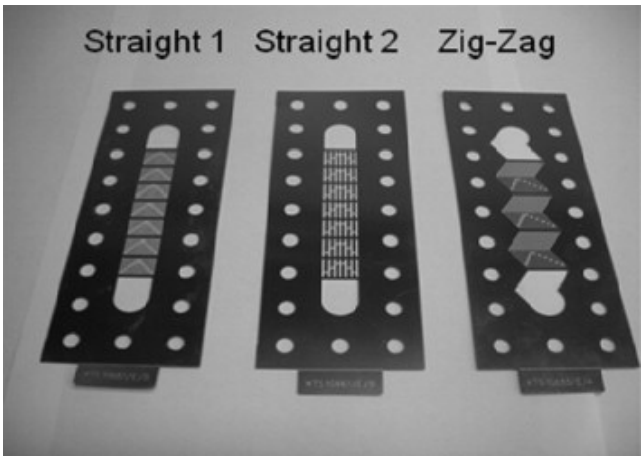

Figure 14. Sheet geometries employed for RTD measurements. "Straight 1" has channels with hydraulic diameter 0.7 mm, "Straight 2" 1.07 mm and "Zig-Zag" has channels with hydraulic diameters 0.75 mm and 0.84 mm (for 5 and 9 shims respectively). ***Source: Cantu-Perez 2011***

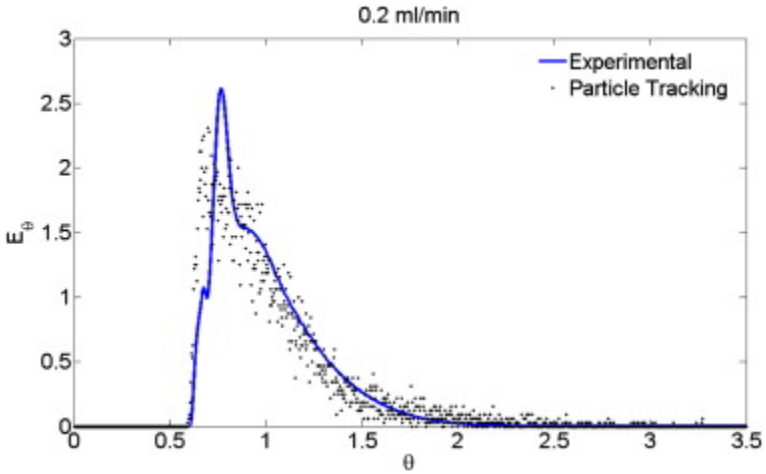

Figure 15. Comparison of experimental vs. numerical RTDs for a rectangular cross section channel. Width = 14 mm, height = 2.46 mm. ***Source: Cantu-Perez 2011***

Residence time distribution in a retention reactor and coaxial heat exchanger in a commerical micro reaction system was investigated in order to improve processing time control.[58] The method of measurement differed significantly from the previous studies. In this system, 30 g/L NaCl solution was used as a tracer in distilled water in a step function (washout function) instead of the more common impulse function. Their reasoning behind a step signal instead of an impulse is that a sharp step function introduces less variability into the measurement than a wide

impulse based on previous work by Reis and colleagues. [59] Conductivity measurements were recorded in that inlet and outlet and deconvolution was performed to arrive at the RTD. Their findings show that in the retention reactor, the RTD remained close to a plug flow behavior despite laminar conditions while the coaxial heat exchanger showed significant dispersion possibly due to it's complex geometry. The authors were unable to fully explain the physical causes behind their findings but make note that numerical modeling, which was not performed, may help to clarify the observed behavior.

Boskovic and Loebbecke investigated residence time distribution in three different micromixers.[60] They measured UV-Vis absorption using Basic Blue 3 dye in spectroscopic flow cells at the inlet and outlet. Variance and Skewness for each RTD were calculated for each micromixer at a range of flow rates and performanace was evaluated based on minimizing both values. They also found that time domain fitting led to best results when deconvoluting experimental pulse response data to obtain the RTD. Boskovic and colleagues followed this work with with an investigation of three microreactor designs that utilize difference passive mixing structures: a 3-D serpentine structure, a split-and-recombine structure, and a staggered herringbone structure.[61] Again, mixing performance was evaluated based on characteristic moments of the distribution. The serpentine reactor and split-and-recombine reactor showed similar, lower variance in the RTD and the authors ascribed this to improved convective mixing and the appearance of chaotic advection which improves transversal mixing.

Adeoson and Lawal investigated laminar flow mixing behavior in a T-junction microchannel using RTDs.[62] They used both numerical and experimental approaches. The experimental system measured the pulse response of uranine tracer via UV-Vis absorption spectroscopy in flow cell positioned at the inlet and outlet of the microchannel unit. Two flow models were used to deconvolute the inlet and outlet pulse response signals through parameter fitting and obtain the RTD: 1) the axial dispersion model (ADM), discussed previously, and 2) the semi-empirical model (SEM), used by Boskovic and Loebbecke [60] for RTD applications and developed by Ham and Platzer [63], which accounts for certain distribution asymmetries in real

flow systems. The SEM fitted experimental results better than ADM and the authors attributed that to the asymmetrical behavior of RTDs associated with strong laminar flow, a characteristic of microchannel systems. For the numerical simulation, flow was solved as stationary whereas tracer material balance was transient and the tracer was modeled as soluble dye with the convection-diffusion equation. The authors used a finite volume-based commercial CFD code of *FLUENT*. Out of six reported data sets, minimum relative error between experimental and numerical residence times was 12.81% and maximum was 21.84%.

Adeosun and Lawal followed this work with an investigation of mixing behavior in a MEMS-based mutilaminated/elongational flow micromixer (MEFM).[64] This was a more complex flow geometry than the T-junction micromixer. A similar experimental technique was utilized, along with similar deconvolution and numerical simulation. The authors considered the MEFM to show good mixing performance considering its narrow RTD with low values of coefficient of variation for the range of investigated flow rates.

Mendez-Portillo et al. performed a numerical investigation on the hydrodynamics of a split-and-recombination microreactor and multilamination microreactor.[65] Numerical simulations were performed using finite element method and the decoupled CFD-mixing approach.[66] This decoupling refers to generation of the computational grid and velocity and pressure field flow variables using CFD and then in the second step, using particle tracking of inert massless tracers in the velocity field to develop the RTD. Utilizing this approach for the complex geometry, out of 8 published datasets, minimum relative error between experimental and numerical mean residence times was 1.06% and maximum was 27.78%.

Table 1 Previous residence time distribution studies in microfluidics.

Reference	Tracer technique	System characterized	Phases	Measurement location
Trachsel et al., 2005	Fluorescence microscopy, 100 nl rhodamine B in EtOH	Single rectangular serpentine channel	Two	Entire chip in 2.5 x 1.5 mm FOV
Cantu-Perez et al.,	LED-photodiode system, parker blue	Bare rectangular channel and channel with herringbone	Single	On microfluidic chip, at outlet

2010	dye	structures		only
Cantu-perez et al., 2011	LED-photodiode system, parker blue dye	Multichannels, straight, zigzag and herringbone	Single	On microfluidic chip, at outlet header
Georget et al., 2013	Conductimetric sensors, NaCl solution step signal	Retention reactor and coaxial heat exchanger	Single	Inlet and outlet, off-chip
Boskovic et al, 2008	Absorption spectrometry using basic blue 3 tracer through flow cells	Three difference micromixers	Single	Inlet and outlet, off-chip
Boskovic et al., 2011	Absorption spectrometry via reflectance probes using basic blue 3 tracer	3-D serpentine structure, a split-and-recombine structure, and a staggered herringbone structure microreactor	Single	Inlet and outlet, on-chip
Adeosun and Lawal, 2009	Absorption spectrometry using uranine tracer through flow cells	T-junction micromixer and multilaminated/elongation flow micromixer	Single	Inlet and outlet, off-chip

Deconvolution is a technique widely used in electrical systems and spectroscopy in which the circuitry or spectroscopy tool convolutes the original signal before displaying the output. In order to determine the original signal profile or image, the system response function, otherwise refered to as the RTD, must be know. There are many approaches to deconvolution such as traditional linear, nonlinear, and fourier methods.[67]–[69] Each has their advantages and disadvantages and each requires a strong understanding of physical limitations of the system of interest.

Deconvolution approaches varied throughout the discussed studies. A very common approach is the utilization of Fourier Transformations, often Fast Fourier Transforms (FFT) along with noise reduction filters. The equation for transformation is show in equation 9, where both input and output profiles are transformed to the frequency domain before carrying out the division operation and then the inverse transformation is performed to return the signal to the spatial domain. The mathematical operations can be performed through built in operations in Matlab.

$$E_{k,deconv}(\theta) = FFT^{-1}\left\{\left|\frac{FFT\{E_{k,out}(\theta)\}}{FFT\{E_{k,in}(\theta)\}}\right|\right\} \qquad \text{Equation 9}$$

In the investigation by Georget et al., their previous work had shown that the RTD could be approximated by the modified Gaussian function with lag and diffusion incorporated (Equation 10). The variables α and η are solved for iteratively using a system of equations.

$$E(t') = \frac{2}{\alpha \cdot \sqrt{\pi}} \cdot e^{-\left[\frac{(t\prime+\eta)^2}{x^2}\right]} \qquad \text{Equation 10}$$

Another approach to deconvoluting the pulse response signal is to solve a linear set of equations. This requires building the convolution integral in matrices with known input and output vectors and an array containing variables representing the system function or RTD.[19] Using iterative techniques, the system function array is modified until the calculated output profile converges with the experimental output profile. This approach was utilized in the Master's work of Eric Anderson [19] and was chosen here because obtaining the RTD is approached without preconceptions of the profile shape, unlike parameter fitting of various models such as ADM or SEM. This is important in complex geometries where observed tracer behavior could be far different from expectations. This research expands upon his work, adding conditions to the solver that reflect the physical system.

4 EXPERIMENTAL MATERIALS AND METHODS

4.1 Lamina fabrication

Lamina designs were created in Solidworks and DXF files were sent to Great Lakes Engineering (Maple Grove, MN) to be fabricated via photochemical machining (PCM) into stainless steel plates (304 SST, 0.030" thick) to a feature depth tolerance of 90-120 micrometers (see Figure 16 for example of master plate). The 30 micrometer range was specified by Great Lakes Engineering. This resulted in a depth close to or slightly deeper than 100 micrometers. All lamina designs contained three fiducials features for aligning secondary laser etching. Figure 17 is an example of the DXF drawing that is sent out for fabrication and shows the location of fiducials. Once master plates were received, they were annealed in a vacuum furnace (CAMCo Furnace, Model J-12, San Carlos, CA) to reduce warping caused by the etching (potato chip effect). See Appendix A.1 for detailed description of annealing protocol.

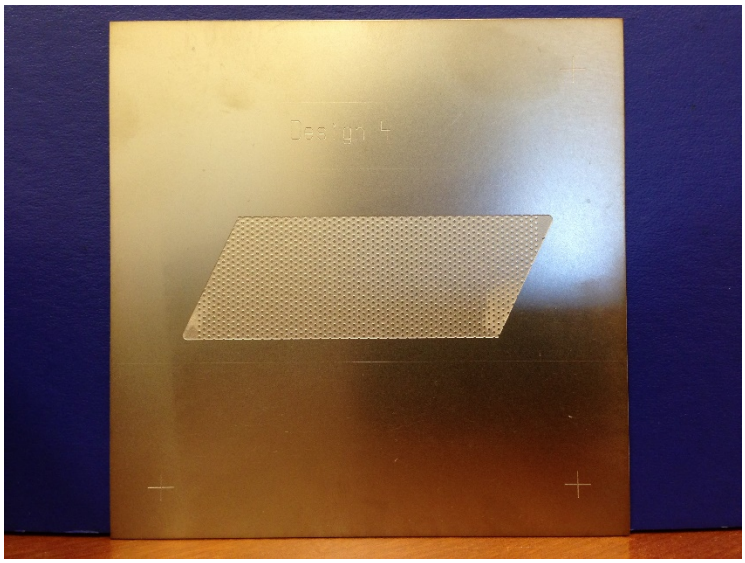

Figure 16. Example of a master plate fabricated by Great Lakes Engineering.

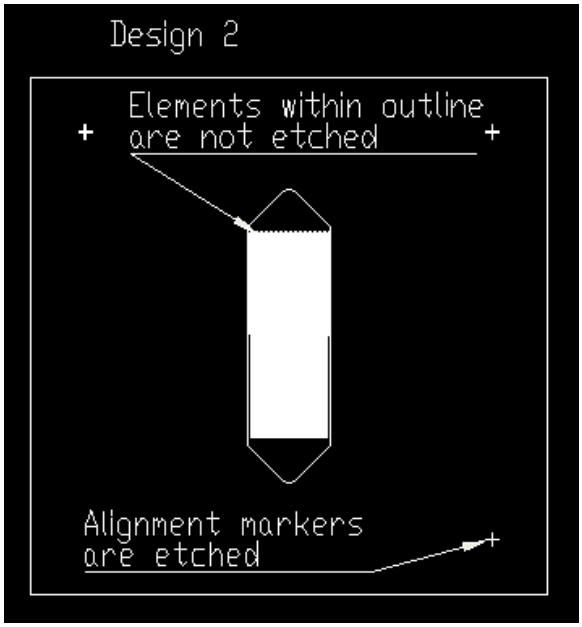

Figure 17. Example of dxf schematic used for PCM. Note alignment fiducials added in three corners that were also etched.

Stainless steel master plates were embossed (Jenoptik Nanoimprinter) into 1.2 mm polyetherimide (PEI) (McMaster-Carr) sheets to obtain a negative imprint of the master plate. Figure 18 shows the Jenoptik Nanoimprinter housed at the Microproducts Breakthrough Institute (Corvallis, OR). Macros for embossing protocols were developed to improve pattern transfer and reduce overheating of substrate polymer. See Appendix A.2 for a detailed description of the macro used for embossing. The arrangement of tool, substrate, and back plate are shown in Figure 19.

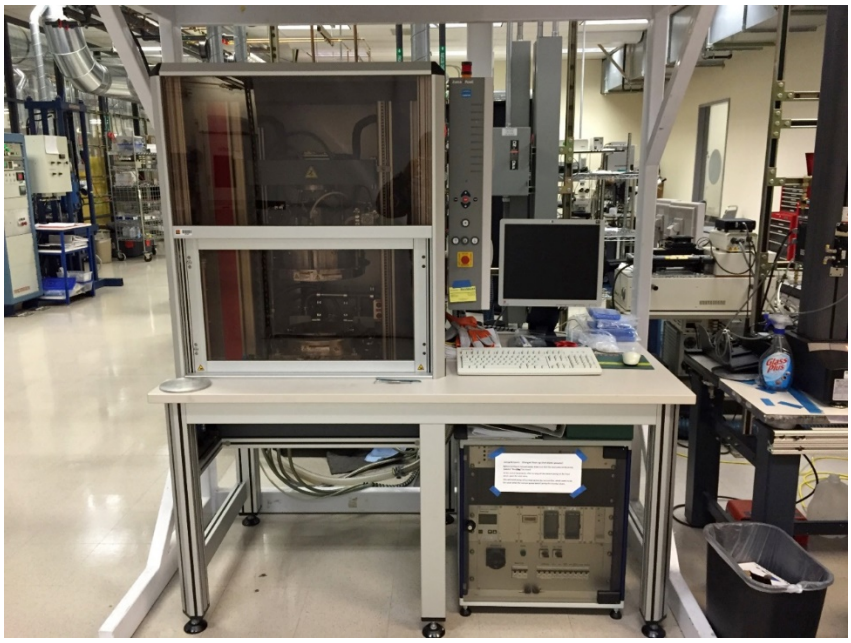

Figure 18. Jenoptik Nanoimprinter used for embossing into various polymers.

Master or tool
Substrate
Back plate

Figure 19. Arrangement of plate layers in embosser.

The PEI plate with negative pattern was trimmed on a ESI 5330 UV Laser μVIA Drill (ESI, Portland, OR) (see Figure 20) set at 532 nm wavelength. See Appendix A.3 for description of the laser settings for cutting PEI. Along with trimming, additional features such as sealing bosses can be ablated at this point, resulting in raised profile in the final lamina. Sealing bosses were not used in lamina for testing of the PEO-coating or the residence time distribution studies but utilized in other studies pertaining to this research for improving sealing ability of microchannel hemodialyzers[70].

Figure 20. ESI UV Laser Drill for trimming and ablating PEI and polycarbonate.

The trimmed PEI plate was placed in an ultrasonic bath containing Alconox solution for 10 minutes to remove burnt polymer residue and then rinsed with deionized water (DIW) and dried with air. The PEI plates were then embossed again into 0.5 mm thick polycarbonate (McMaster Carr) using the Jenoptik Nanoimprinter. See Appendix A.4 for protocol on embossing PEI into polycarbonate. The polycarbonate plate now contained the original pattern etched into the stainless steel master plates. They were trimmed and fluid through holes and alignment pinholes were cut using the ESI UV Laser again (see Figure 21 for example of polycarbonate lamina). Appendix A.5 lists the appropriate laser settings for cutting the 0.5mm thick polycarbonate. Finally, the polycarbonate lamina was ultrasonically cleaned as previously done with PEI plates and through holes were inspected and cleaned for any hanging burrs using a syringe needle. Figure 22 shows a general overview of the fabrication process described above. This includes the previously mentioned secondary features (sealing bosses) that were not utilized in these specific studies but could be present in a more finalized multilayer device.

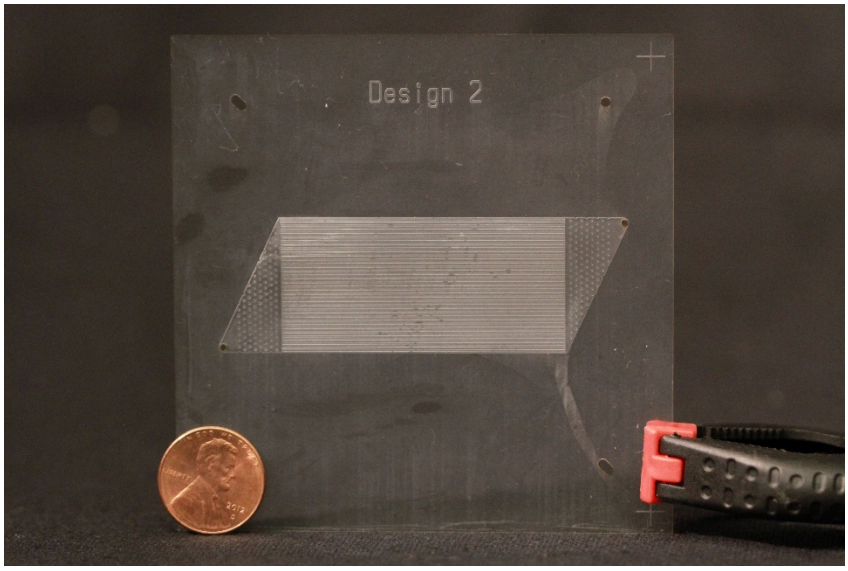

Figure 21. Example of final polycarbonate lamina. Note the alignment pin holes and fluid throug holes machined in final steps.

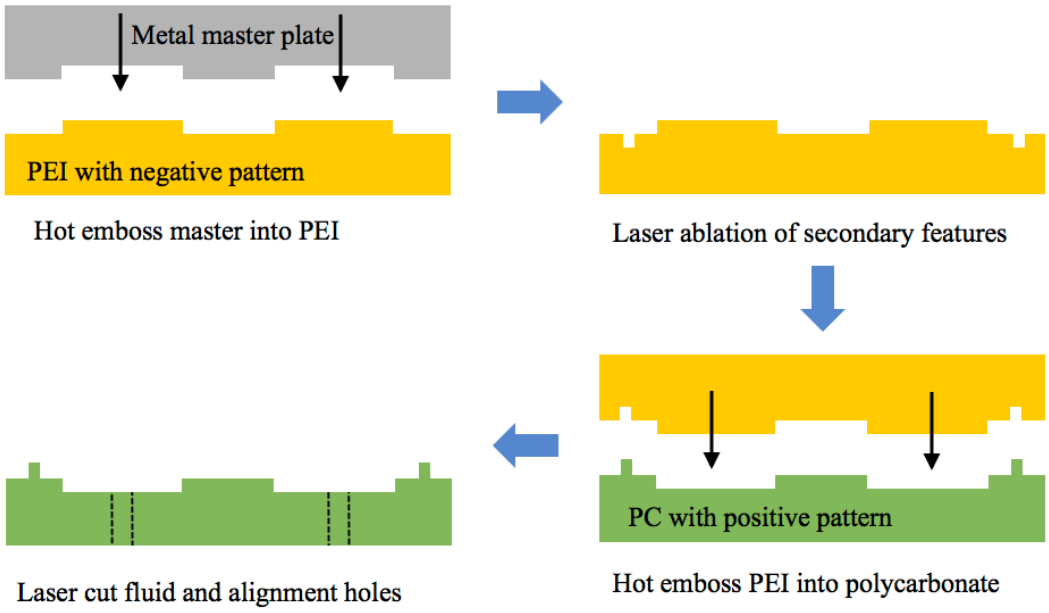

Figure 22. General overview of fabrication process from stainless steel (SS) master plate to final polycarbonate lamina.

4.2 PEO Surface Treatment

Hydroxyl-terminated PEO-PB-PEO triblock surfactants were purchased from University of Minnesota Polymer Synthesis Facility (Minneapolis, MN). The

triblocks consists of a polybutadiene centerblock (M_n = 620) and PEO side-chains of M_n = 2845 with a polydispersity index of approximately 1.11 (by size-exclusion chromatography)

Laminas were exposed to 20 mL of 1 mg/mL PEO-PB-PEO triblock copolymer in HPLC water for 12 hr at 20°C, on a shake-plate at 50 RPM to allow for self-assembly of triblocks on polycarbonate surface. Laminas were covered with foil during this incubation to minimize exposure to light. Laminas were then exposed to 0.3 Mrad of gamma-irradiation by a ^{60}Co source. Excess and unbound triblock copolymer was rinsed from the laminas with 10 mL of HPLC grade water (repeated three times on each side of the lamina). Laminas were stored in HPLC grade water for a maximum of 1 month, or until use. Before device assembly, laminas were dried with pressurized nitrogen.

The procedures for this PEO-PB-PEO surface treatment were developed through the master these work of Keely Heintz at Oregon State University. A detailed description of the protocol can be found in her thesis.[12]

4.3 Lamina Design for PEO-Coating and RTD Investigation

4.3.1 Lamina for PEO-Coating study

The polycarbonate lamina contained a 40-microchannel array with symmetric triangular headers on either end of the channels (Figure 23A). Each microchannel was 30 mm in length and ~250 μm wide and ~95 μm deep. Figure 23B shows the cross-sectional profile of two adjacent microchannels obtained on a Zemetrics Zescope Optical Profiler. This measurement was performed on the stainless steel master plate after embossing. This channel/header design was chosen for its simplicity. Our focus with the PEO-coating study was behavior of bubbles within the channel region therefore we chose a design that would be sufficiently easy to replicate multiple copies and we could guarantee proper sealing against the dialysis membrane.

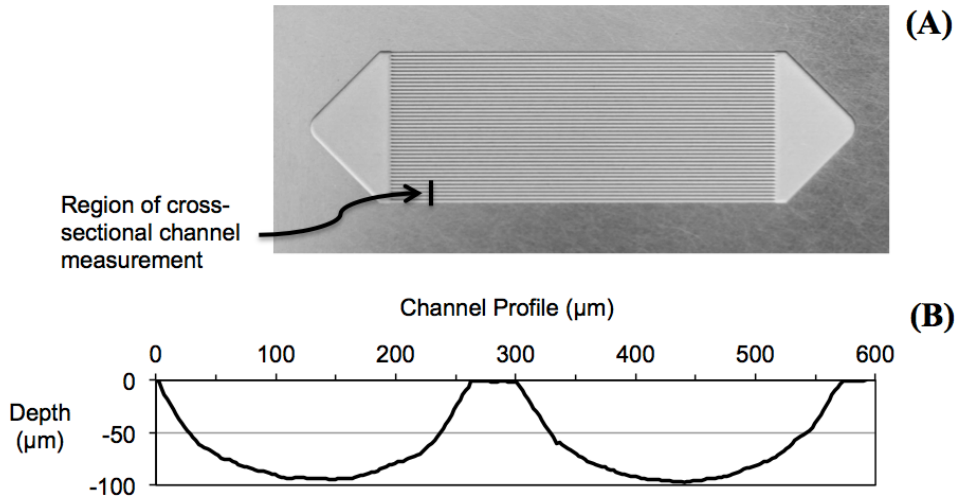

Figure 23. (A) Stainless steel master plate. (B) Cross-sectional profile of microchannels (µm).

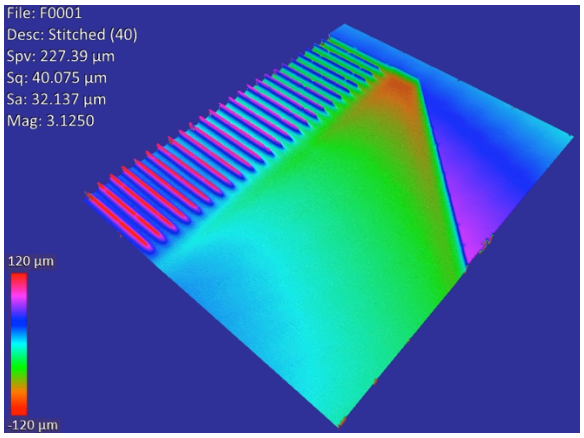

Figure 24. 3D profile of transition from header to channels, take on Zescope.

4.3.2 Laminas for RTD study

For the RTD investigation, the primary focus was the geometry of the flow region and not the surface/fluid interaction. This meant that we could seal the device more effectively against a PDMS layer acting as a gasket and therefore explore larger more complicated designs that are more representative of what would be found in a commercial device. Because of this, 4 designs were chosen for this study that contained 60 channels (20 more channels than PEO-coated lamina) or an equivalent length if no channels were used, along with asymmetrical triangular headers, with and

without micro-post support architecture. Table 2 lists four lamina designs used in this investigation, along with naming scheme used to improve clarity when conveying results and major architecture features that differentiate each design. Figure 25 shows the Solidworks drawings for the four different lamina designs, along with a naming scheme for clarity throughout this writing. In various images throughout this work, lamina may have a design number embossed on the polycarbonate surface. These numbers do not refer to the numbering scheme in Table 2 and were only used during the order process with fabricating the metal masters plates. The microchannel cross-sectional profile was similar to the PEO-coating lamina study at 0.02 mm^2 per channel with only small variance between master plates (< 2%). The microchannel wall/rib width was twice that of the PEO-coating lamina microchannel wall width.

Table 2 Characteristics of four laminas used in RTD study

Design	Name	Header width (from through hole center to edge of channel)	Micro-posts in header	Channel length
1	Slim-header	5 mm	No	6 cm
2	Wide-header	10 mm	No	5 cm
3	Wide-posts	10 mm	Yes	5 cm
4	All posts	10 mm	Yes	Equivalent to 5 cm geometry

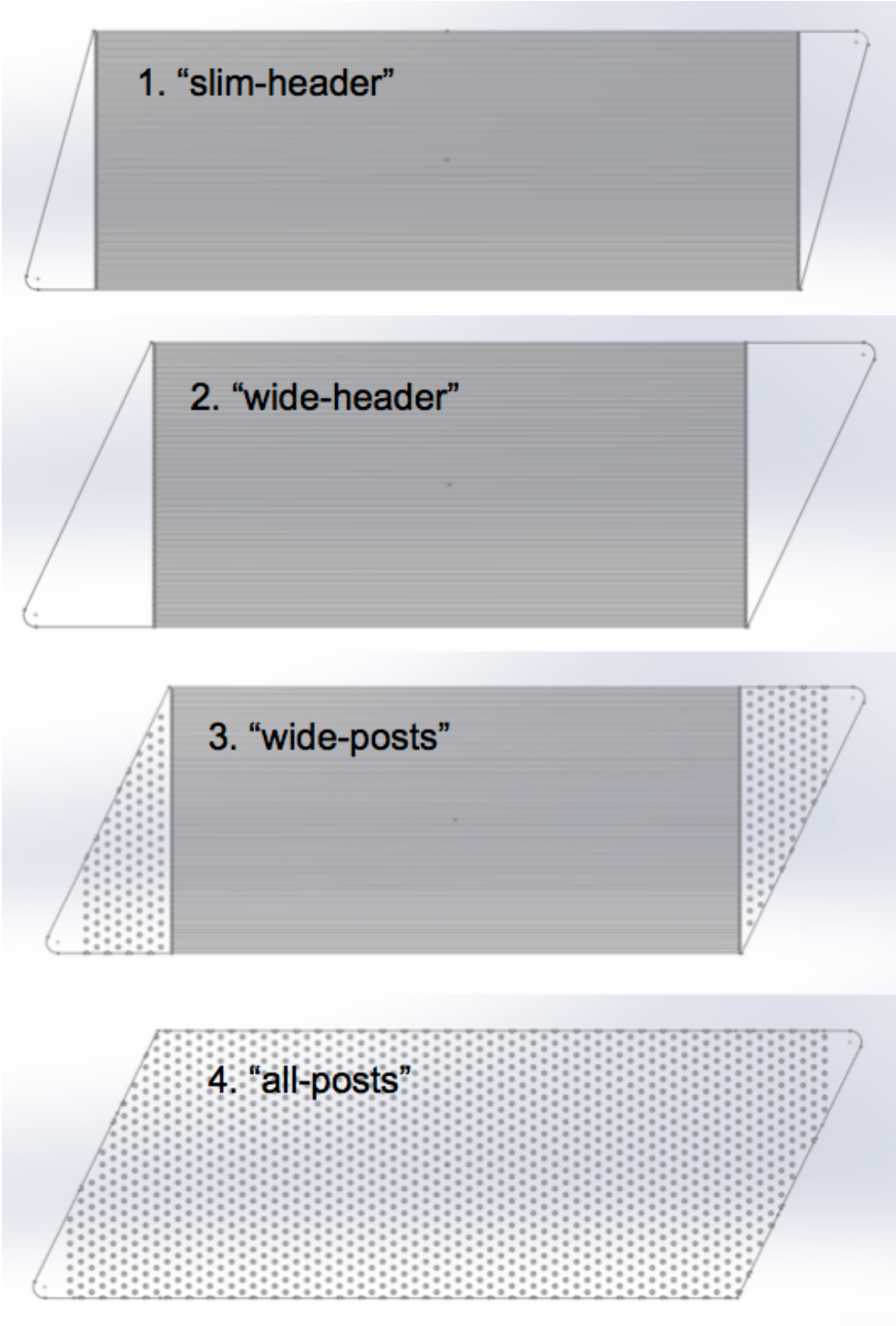

Figure 25. Four lamina designs used in the RTD investigation.

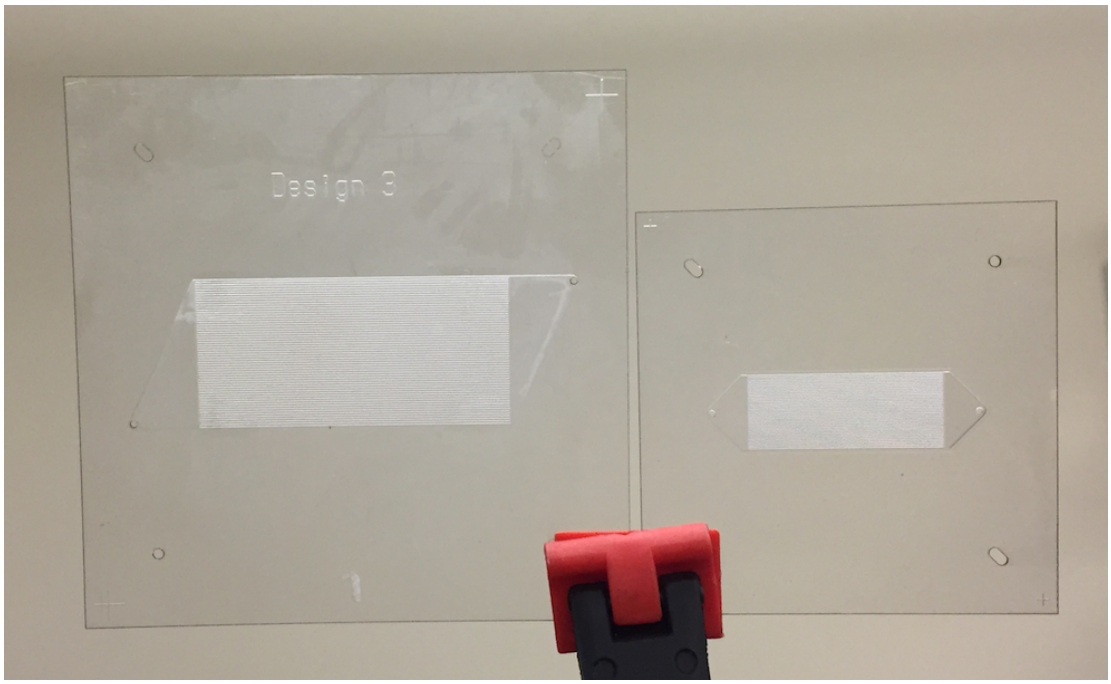

Figure 26. Comparison of laminas used for pulse response measurements (left) and PEO-coating study (right).

4.4 Enclosure Design and Assembly

4.4.1 Enclosure for PEO-coating study

The microchannel hemodialysis unit used for this investigation is primarily a polycarbonate lamina compressed against dialysis membrane. A single lamina was compressed against Gambro AN69 ST polyacrylonitrile (PAN) hemodialysis membrane (Home Dialysis Plus, Sunnyvale, CA) supported on 200 μm thick polycarbonate film to assist in laser trimming (ESI UV laser drill), handling, and sealing. Figure 27 shows the arrangement of lamina, membrane, and backing described above, along with an example of a possible arrangement in a fully functioning dialyzer. All three layers were aligned between 2 cm thick polycarbonate platens containing inlet and outlet fluid flow lines and alignment pinholes. For sufficient visual access to the microchannels and headers, and because filtration was not the focus of this study, only a single lamina was utilized instead of multiple laminae required for dialysis. This also allowed for improved sealing, as no fluid would be able to exit via the lamina side that was not under investigation.

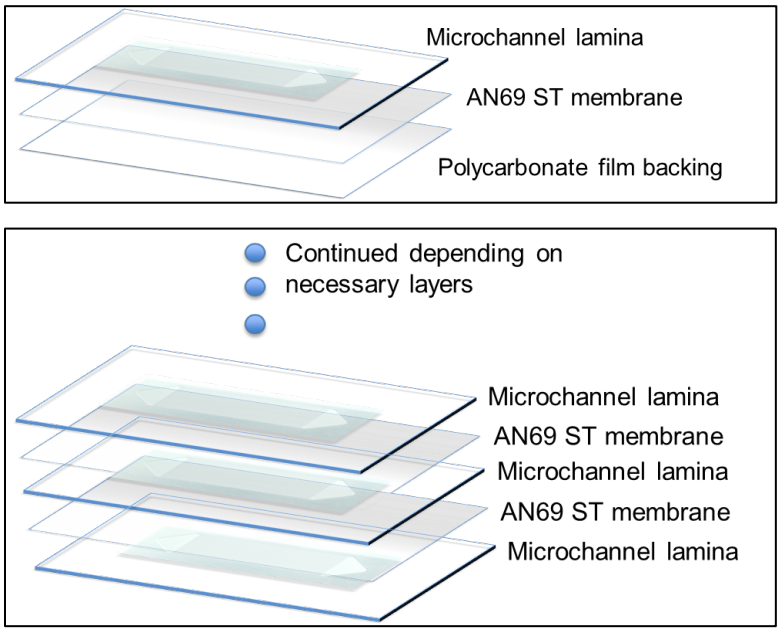

Figure 27. (Top) Arrangement of lamina, dialysis membrane, and backing material for PEO-coating study. (Bottom) Arrangement of laminas and dialysis membranes for application in a functioning hemodialyzer.

The entire stack was compressed between aluminum platens and a 0.500" BISCO HT-800 cellular silicone layer (Rogers Corporation, Carols Stream, IL). The large elastic region of the silicone layer distributes force more uniformly by reducing the parallelism effect and thickness tolerances of the rigid enclosure components. The aluminum platens contained viewing windows from both top and bottom to allow front or back lighting of the system. Figure 28 is an exploded schematic of the components listed above comprising the enclosure and Figure 29 is an image of the fully assembled device. The original design for enclosure assembly was developed by Spencer Porter and modified for this work. Further description of the enclosure and design process is detail in his Master's thesis.[71]

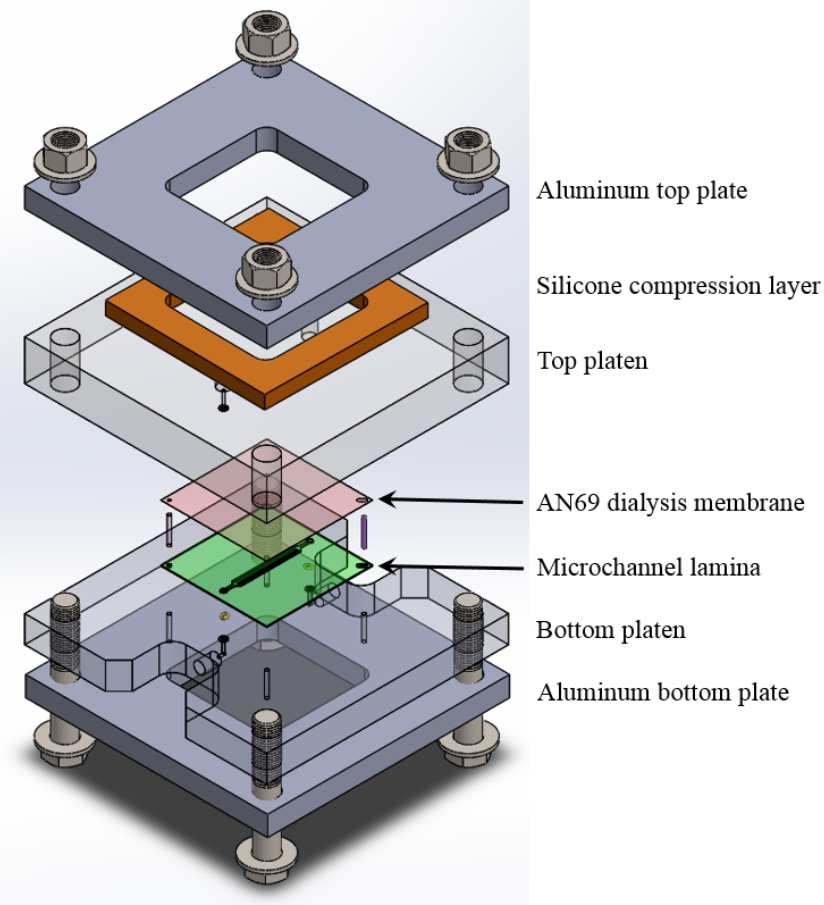

Figure 28. Exploded 3D schematic of the dialysis enclosure used for the PEO-coating study.

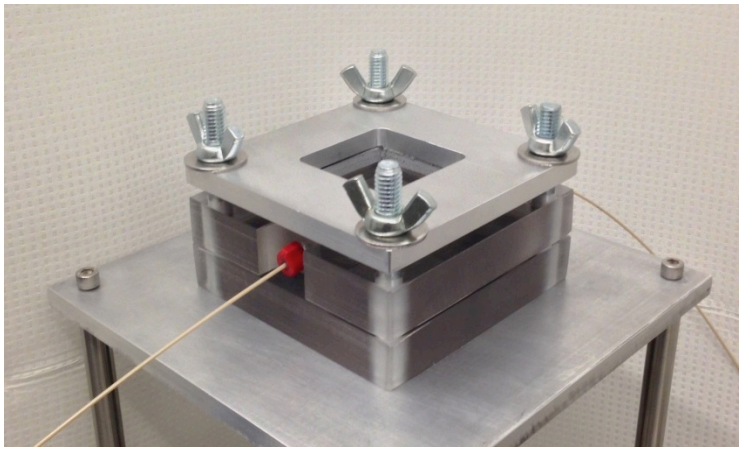

Figure 29. Fully assembled device enclosure for PEO-study.

4.4.2 Enclosure for RTD study

The device enclosure used in the RTD study was based on the PEO-coating enclosure but redesigned to seal the larger lamina and also allow for visual access to the microchannel geometry. Figure 30 shows lamina situated between the two large platens and the larger viewing window cut into the aluminum compression plate.

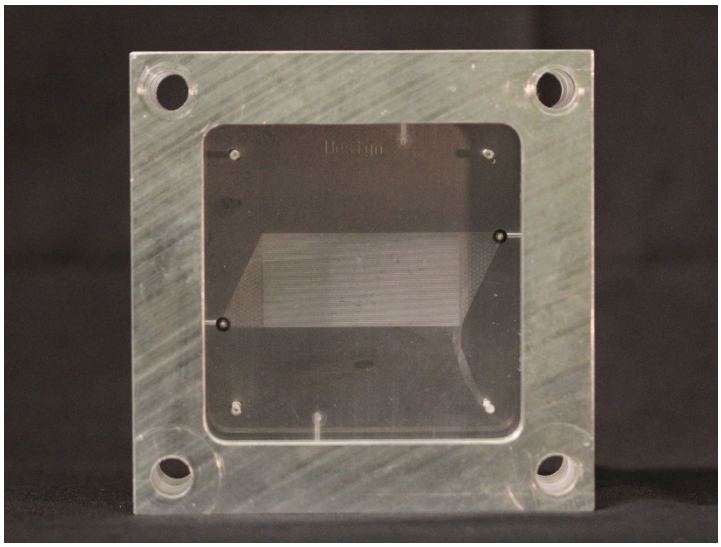

Figure 30. "Wide-posts" lamina situated between platens and behind aluminum compression plate with viewing window.

Thicker and multiple silicone pad layers were used to assist in uniformly compressing the larger area of the lamina. During developmental work and parallel research investigating improvement in sealing devices, conducted by Dusty Ward and Patrick McNeff, force sensors were utilized in the system to ensure uniform clamping

force at each corner bolt. We achieved a satisfactory level of hermetic sealing and removed the force sensors during data collection experiments. For further information on the application of force sensors to control clamping force, see Dusty Ward's Master's Thesis (Oregon State University). [72]

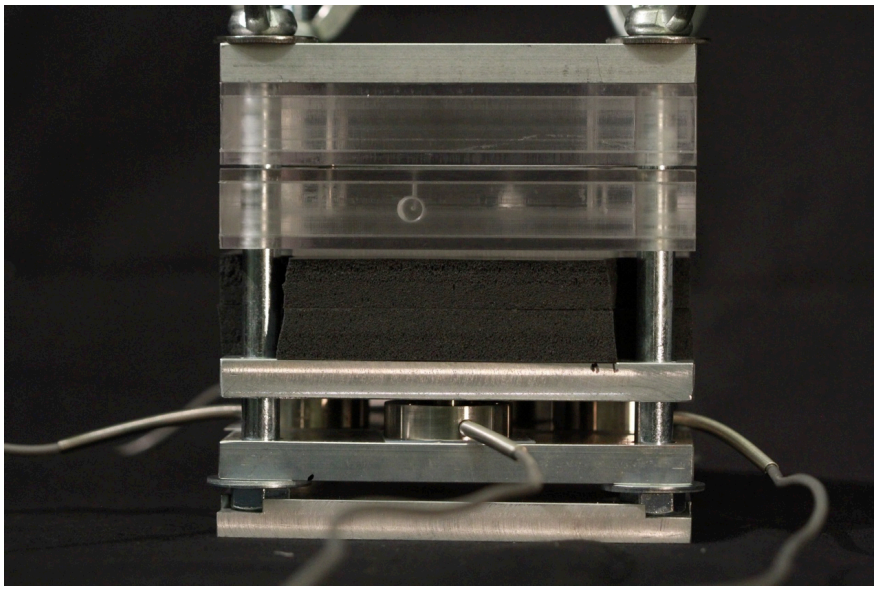

Figure 31. Fully assembled enclosure with added force sensors used in developmental work but removed for data collection experiments.

As noted in the lamina design section (4.3.2), the AN69 ST dialysis membrane was not used in this study because general fluid flow geometry was a focus instead of surface/liquid interactions. Because of this, to assist in sealing, the lamina was sealed against a thin film of PDMS.

Sealing of the device was achieved by turning all four nuts onto the bolts until light resistance was felt and rotating each nut one quarter turn, cycling clockwise through each nut five times.

4.5 Imaging System and Procedures for PEO-coating study

The enclosure described in section 4.4.1 was mounted on a lifted platform that allowed for visual access and lighting of the microchannel lamina. Images were captured using a LaVision Imager sCMOS camera coupled with an AF micro-Nikkor 60 mm f/2.8D lens. The camera has a sensor resolution of 2560 x 2160 pixels with a 16-bit grayscale level. A prism was placed below the viewing window to allow the

camera next to sit next to the enclosure and platform instead of underneath or above it. A 40W incandescent bulb provided backlighting from the top-viewing window. The system utilizes shadowgraphy based on differences in refraction between air and water to distinguish interfaces. Gas bubbles were introduced to the system by injecting air into the main flow line (0.25 mm I.D. Radel tubing) at a T-junction using a 1.0 ml syringe. The air entering the main line is sheared off into a train of bubbles that flow into the device. Figure 32 is a schematic of the test system and image of the lamina enclosure with camera, light, and syringe for injecting air. Figure 33 is an image of the experimental setup as it was in the laboratory. This imaging setup was built and assembled by Mahshid Mohammadi and a detailed description can be found in her Ph.D. dissertation.[73] The sCMOS camera can be replaced with a Canon 7D digital SLR camera fitted with a Canon Macro Lens EF 100 mm for color images and videos.

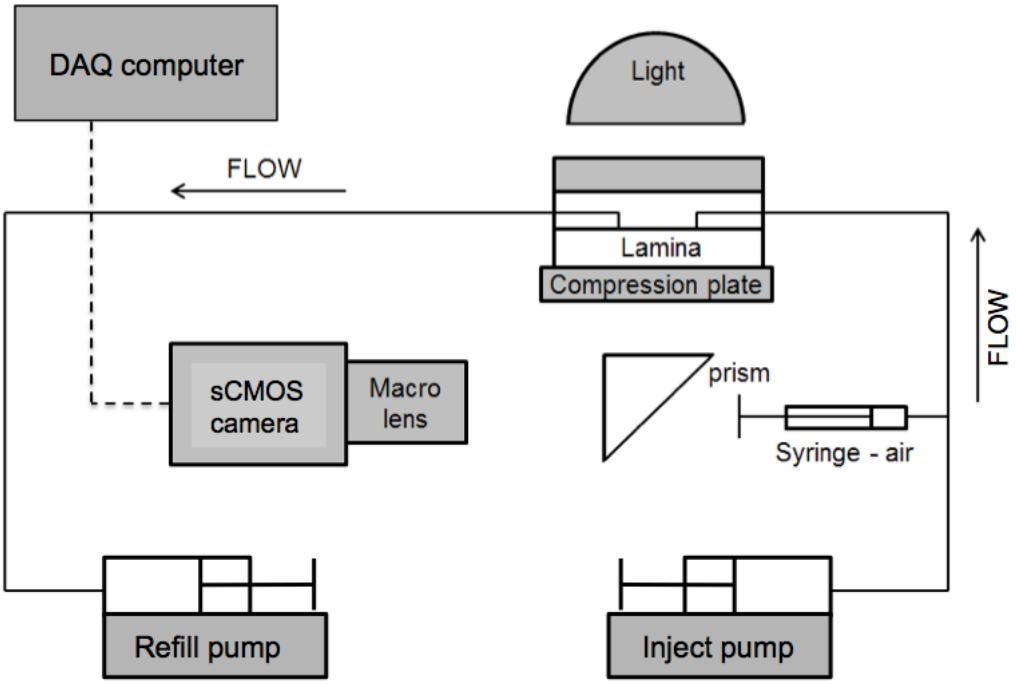

Figure 32. Schematic of test system. Injection syringe pump feeds fluid into the dialyzer housing, which contains the microchannel lamina. Air was injected at a T-junction. Images were captured by sCMOS camera positioned beneath the microchannel housing.

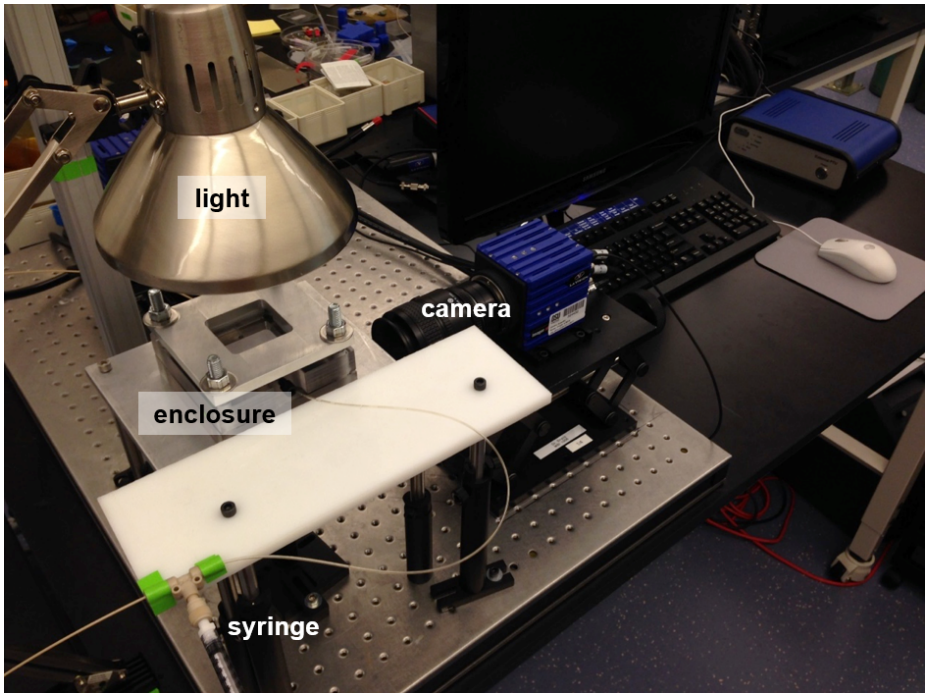

Figure 33. Image of experimental system for PEO-coating study

After assembling the lamina and dialysis membrane within the device enclosure, image recording was initiated, followed by priming the microchannels with deionized water. After the initial priming event, a train of air bubbles was injected into the system after which the system was allowed to stabilize for 1-2 minutes (stabile considered when the remaining bubbles in the microchannels are stationary) and then the number of channels obstructed by bubbles were recorded. Channel blockage was reported as percent blocked channels, which refers to percentage of channels (out of 40) that contain at least one bubble spanning the entire width of the microchannel. Another train of bubbles was introduced into the system and another measurement was record.

At least 9 measurements were recorded for each test group. There were 16 test groups: uncoated and coated lamina under flow rates of 0.5, 1, 1.25, 1.5, 2, 3, and 4 ml/min. The flow rates corresponded to average fluid velocities through the microchannels of 0.9, 1.8, 2.25, 2.7, 3.6, 5.4, and 7.2 cm/s respectively for an unobstructed system, referred to as average nominal velocity. The fluid used for these

experiments was deionized water. Water was chosen instead of blood or protein rich plasma because the associated interfacial energies between polycarbonate, water, and air create a poor environment for bubble movement through the microchannels, similar to what exists in the dialysate compartment of a hemodialysis device.

4.6 Pulse Response Test Loop

A test loop was developed for measuring the pulse response of a dye injected into the microchannel device for the RTD study. Below is a description of the test loop, followed by improvements made to the system and their justifications.

4.6.1 Design and Layout of Pulse Response Test Loop

Deionized water (DIW) was pumped into the system through a syringe pump (Harvard Apparatus PHD-2000) through 0.76 mm ID Radel tubing (for visibility) past a shut off valve and into a Y-junction. Another duplicate syringe pump fed isopropyl alcohol (IPA) in through a check valve, a shut-off valve, and then into the other arm of the Y-junction. The IPA is used to assist in priming the device due to its lower surface tension that can mobilize stagnant air bubble. The shut off valves and the check valve is used to ensure that DIW does not enter the device during priming and more importantly that IPA does not enter the DIW syringe during priming and the device during a pulse response measurement test. The exit arm of the Y-junction connected to a 4-port low pressure HPLC injector with 2.0 µl sample loop (VICI Valco Instruments Co., Houston, TX).

The sample loading port of the HPLC injector was extended with Radel tubing to move the loading syringe receptor away from the microchannel enclosure. This allowed for filling of the sample loop without disassembling the top of the enclosure each time. In general, a major consideration during design and assembly of the test loop was avoiding potential disturbances to the microchannel system between experiments in order to improve precision.

The inlet port of the microchannel device was connected to the outlet port of the HPLC injector via a 0.1 mm I.D. Radel tubing with a custom machined absorbance flow cell attached. Radel tubing (0.2 mm I.D.) with another absorbance

flow cell attached was connected to outlet port of microchannel device and fed into a waste container.

A halogen light source (AvaLight-Hal) fed light through a fiber optic cable to a splitter that then fed into each flow cell where it passed through the tubing and any fluid in the light path. The path length for absorbance is equivalent to the inner diameter of the tubing. The light then travelled through another fiber optic cable and into separate UV-Vis spectrophotometers (AvaSpec-Dual Channel USB-2) for the inlet and outlet measurements. The light source and spectrophotometers are from Avantes USA (Broomfield, CO). The spectrophotometer saves readings directly to the onboard ram, allowing for high speed sampling rates (minimum sampling interval of 1.05 ms). We did not necessarily require such a high sampling rate, which fills the ram storage too quickly to record the entire absorbance signal, so a light attenuator (Avantes) and reflective neutral density filter (Thorlabs) has been built into the light source to control light intensity and modify detector integration time to a more suitable sampling rate.

Figure 34 is a schematic of the test loop that has been assembled and Figure 35 shows the fiber optic flow cells in closer detail. A Canon 7D digital SLR camera fitted with a Canon Macro Lens EF 100 mm for color images and videos was positioned over the device enclosure to record tracer dye flowing through the microchannel lamina. Figure 36 shows the entire test loop as it was set up in experiments with the camera situated over the device.

All syringe pump used in this study and the PEO coating study were calibrated by collected samples at fixed times and various flow rate settings to determine tool drift. These corrections were applied to the pump settings during experiments to ensure accurate flow rate.

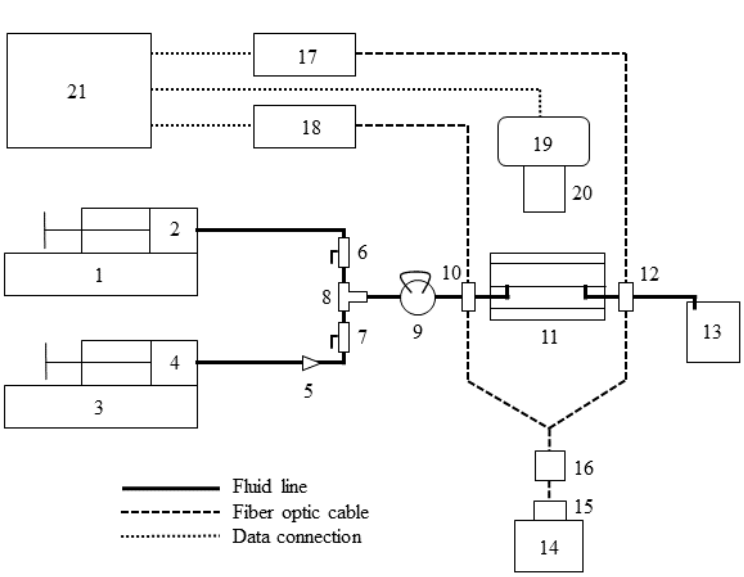

1	Pump
2	Syringe – DIW
3	Pump
4	Syringe – IPA
5	Check valve
6	Shut-off valve
7	Shut-off valve
8	Y-connector fitting
9	HPLC fitting
10	Absorbance flowcell
11	Microchannel device
12	Absorbance flowcell
13	Outflow container
14	Halogen light source
15	N.D. filter
16	Attenuator
17	Spectrophotometer
18	Spectrophotometer
19	DSLR camera
20	Macro lens
21	Data acquisition computer

Figure 34. Schematic of pulse response test loop with inlet and outlet absorption measurement.

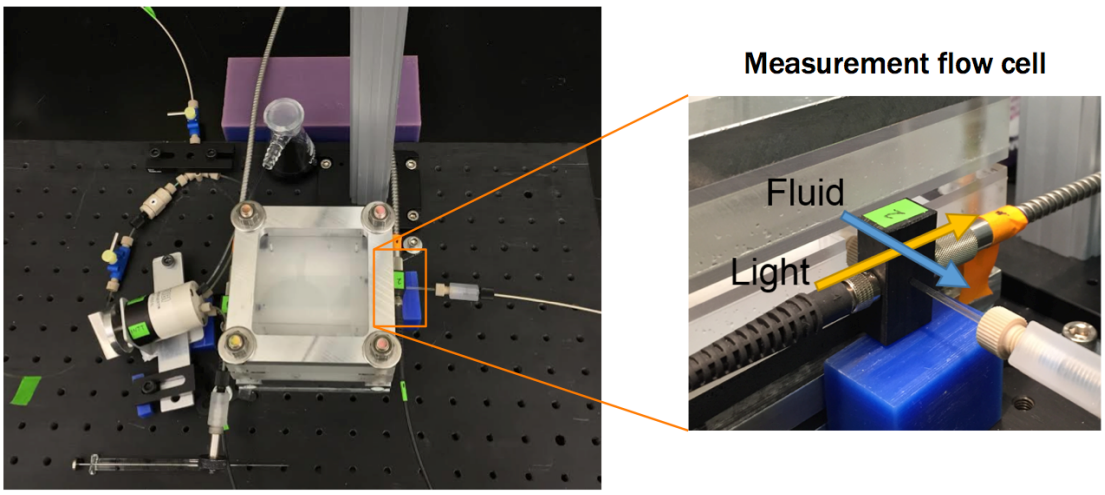

Figure 35. Flow cell used for spectrophotometric measurements.

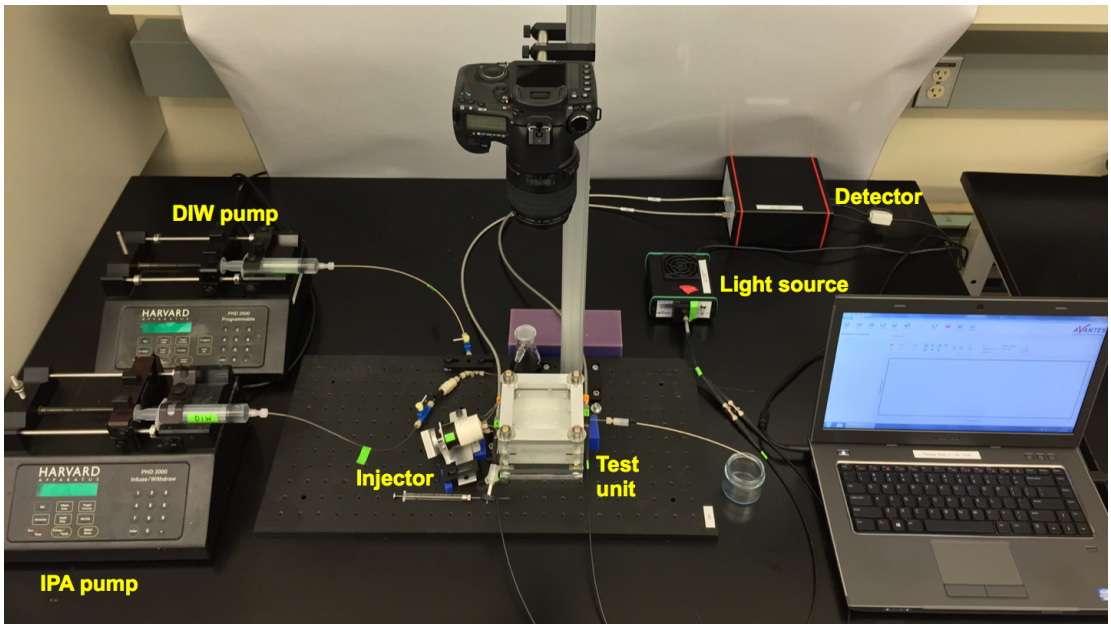

Figure 36. Pulse response test loop as it was arranged during experiments for this work.

4.6.2 Dye Tracer and Absorbance Calibration

The tracer dye used was Coomassie Brilliant Blue with a diffusion coefficient of 0.568×10^{-9} m^2/s.[74] This has shown a satisfactory linear trend in relating concentration to absorbance at a wavelength of 630 nm. Dextran Blue was used as a tracer dye in previous work by Eric Anderson for his Masters work.[19] Coomassie brilliant blue was chosen instead of dextran blue because at the shorter absorbance path lengths of the flow cells, higher dye concentrations were necessary, leading to high density variation between DIW and dye solution which caused sinking of the tracer as it flowed through the system. Coomassie brilliant blue is a smaller molecule and more potent dye allowing for lower concentrations in the tracer solution.

A calibration curve was developed for each flow cell relating absorbance level to dye concentration. This was data was used to determine the linear response range of the dye corresponding to Beer-Lambert law. The inlet flow cell had a linear response range maximum at ~1.3 absorbance units. After that, the absorbance values began to plateau as concentration was increased (higher concentration values are not shown). The inlet flow cell dictated the maximum dye concentration that would be injected into the system because by the time the dye reaches the outlet flow cell,

dispersive effects have lowered the concentration well below the outlet flow cell maximum concentration limit. The maximum allowable dye concentration was used in all experiments in order to increase the measured signal of the output.

Additionally, the slopes of the curves were used to verify that both flow cells behaved as expected by comparing the ratio of the absorbance path-lengths (tubing I.D.) with the ratio of the slopes for the fitted line in the calibration data. The difference was satisfactory at ~1% error and allowed us to confidently convert absorbance values to concentration values in order to inspect the mass balance over the system during experiments.

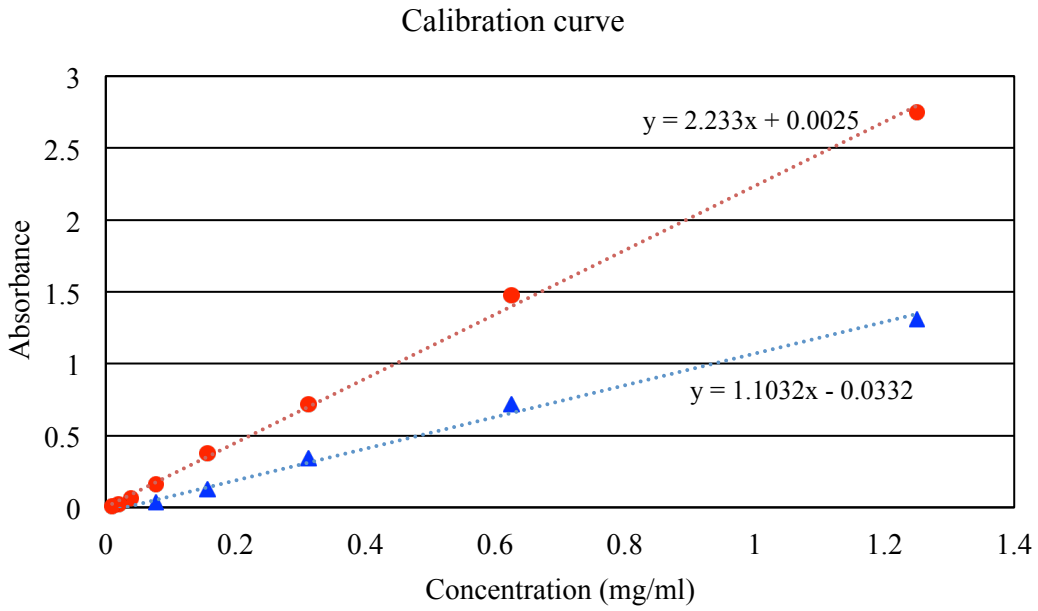

Figure 37. Example of calibration curve for inlet [●] and outlet [▲] flow cells.

4.7 Experimental Procedures and Groups for Pulse Response Measurements

The following are procedures for measuring the pulse response of a tracer dye through the microchannel device using the test loop described in the previous section 4.6.

4.7.1 Pulse Response Measurement Procedures

Lamina and PDMS for sealing were placed in an ultrasonic bath of diluted Alconox solution for 15 minutes, followed by thorough rinsing with DIW. This cleaning was performed before each experiment set (new assembling of device) to remove any residue from fabrication or dust particles collected during storage. If any debris or residue persists, a small brush was used to clean the microchannel surface with isopropanol and then rinsed with DIW again. Lamina was finally inspected under a stereoscopic microscope to verify sufficient cleaning. These steps were repeated until lamina was clean. This was important to ensuring repeatability of measurements of the same lamina between assemblies of the device.

Polycarbonate platens for alignment and fluid through holes were cleaned with isopropanol and DIW and fluid through holes were inspected for any obstructing debris. Lamina, PDMS layers and platens were immediately assembled within the enclosure following cleaning to minimize the probability of dust settling on lamina. Even if we did not take measurements immediately the device was still assembled immediately following cleaning.

After assembling the device, the absorbance flow cells were inspected to make sure their edge butted up against the enclosure edge and that the fiber optic cable heads were pushes in far enough that they were touching the radel tubing within. The HPLC injector was set to the “load injection loop” position.

The valve for the DIW fluid line was closed and the microchannel lamina was flushed with IPA to remove air bubbles at 1-2 ml/min. The IPA fluid line valve was closed and DIW valve was opened. The lamina was primed with DIW at 0.768 ml/min for at least 2 minutes, until scope reading on the spectrophotometers stabilized, and until the droplet forming at the outlet tubing stabilized in shape (varying concentration of IPA in DIW creates a varying surface tension that causes the droplet to “shake” as it grow before dropping).

After priming, the injection loop was loaded with coomassie brilliant blue dye solution. A reference measurement was recorded via the Avantes software bundled with the spectrophotometers. A dark measurement was also recorded. The store to ram parameters dictate the

Set the integration time based on the appropriate sampling rate and adjust light source to accommodate this scope sensitivity.

To initiate the pulse response measurement, video recording was started on the DSLR camera, measurement recording on the spectrophotometers was initiated, and then injector was switched from the load position to the inject position.

After measurement was complete, the DIW syringe pump was set to off and system was allowed to rest for 1 minute before switching injector back to the load position. This pause was added to minimize the presence of bubbles forming in the injector as the pressure is settling. After reloading the injector with dye and before taking another pulse response measurement, fluid flow was started again and the system was allowed to run for 1 minute to ensure fully developed flow and to inspect for bubbles that may have entered the system.

As mentioned above, video was recorded for each experiment but due to the low dye concentrations necessary to avoid over saturating the absorbance measurement, the dye coloration was faint in the lamina volume. An addition experimental run was conducted at 5x the normal dye concentration for visualizing purposes. The flow patterns of the stronger dye recordings matched well with the original experiments, which is to be expected because increasing dye concentration only shifts the concentration higher in the pulse response without altering the normalized distribution of dye through the device. A significant change in flow pattern or distribution would arise only if the fluid properties are dramatically altered as a result of injecting more dye into the system.

4.7.2 Creating Controlled Defects in Microchannel Lamina

Defects were simulated in the microchannel device for pulse response experiments. These controlled defects simulated deactivated regions of the fluid flow volume that could be a result of stagnant bubbles, incorrectly fabricated lamina, or debris blocking microchannels. In order to achieve this, microchannels or micro-post regions were filled with Critoseal vinyl plastic putty. This is a product originally intended for sealing capillary tubes. The putty blockage can be easily removed using

a small brush with isopropyl alcohol; ensuring lamina could be reused for different blockage conditions.

Initially, only one portion of each channel was blocked. This caused an air bubble to remain stagnant in the channel on either side of the obstruction. During operation for experiments, the bubble would expand into the header region altering the measurement. Priming was insufficient at dislodging the bubbles. In an actual event of a air bubble obstructing a channel, there would be liquid filling the rest of the microchannel and this additional problem wouldn't exist. It was decided that the entrance and the exit of each microchannel must be blocked to control the air bubble, two blockage locations. Figure 38 shows the entrance obstructions of two blocked channels for a design 1 "slim-header" lamina. It was verified via Figure 39 that when a stagnant bubble obstructs a microchannel, the liquid flow is essentially shut off from the channel. Note the lack of blue tracer in the channels containing bubbles (flow from left to right). Additionally, the bubbles hanging from the channels in the upper portion of the right header give an example what was similarly observed with the single obstruction method.

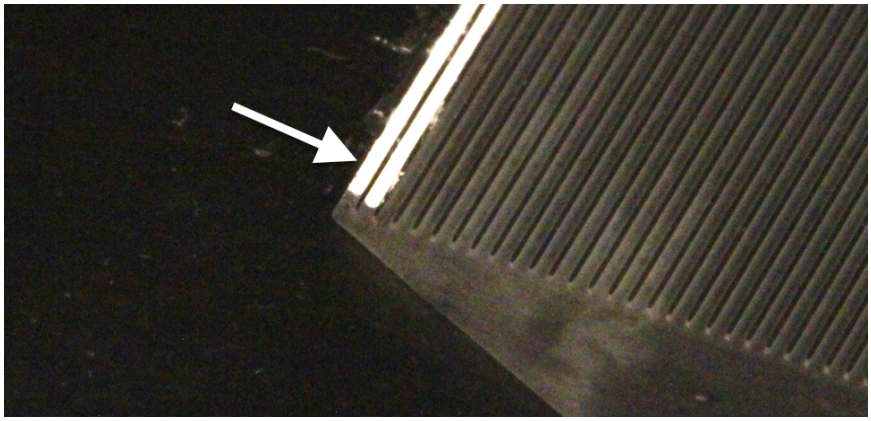

Figure 38. Two microchannels on the edge of a channel array have been blocked or sealed close with Critoseal putty.

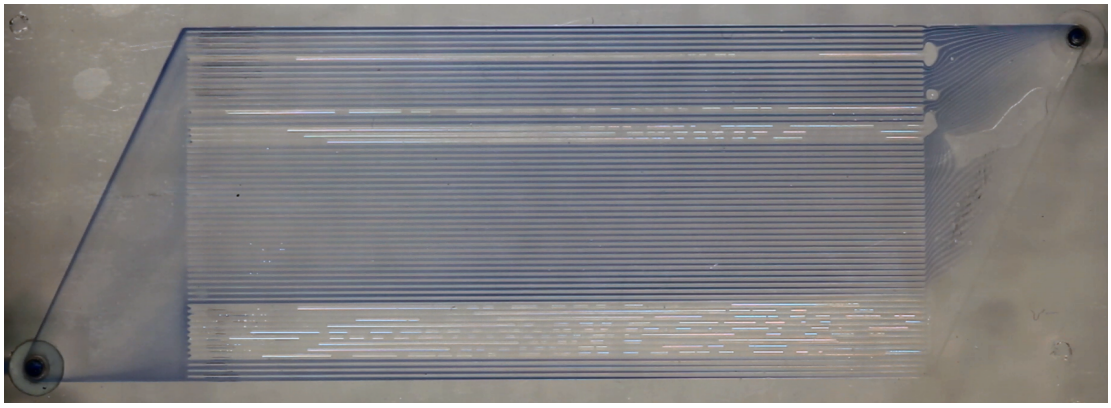

Figure 39. Dye flowing through an improperly primed lamina. Note the lack of dye flow in channels with obstructed by bubbles. Flow from left to right.

4.7.3 Experimental Groups for RTD Study

The RTD study was separated primarily into two investigations: 1) determine the sensitivity of the pulse response measurement method for detecting defects via shifts in the mean residence time from the normal value and 2) determine how lamina design and defects influence the residence time distribution through the device. To accomplish both objectives, four types of lamina were fabricated as discussed in section 4.3.2.

To determine the measurement sensitivity of the pulse response test loop, design 1 (slim-header) and design 2 (wide-header) tested under a range of blockage conditions: 0, 4, 8, 16, 24, and 32 blocked channels. The outermost microchannels were blocked on each side of the channel array, e.g., for the 8 blocked channels

condition, the 4 topmost channels and 4 bottommost channels were obstructed. Each lamina design and blockage condition was measured in 3 separate assemblies and 3 measurements per assembly. The flow rate was 0.768 ml/min for all pulse response experiments. This flow rate equates to a nominal average fluid velocity of 1.0 cm/s through the microchannels for the slim-header, wide-header, and wide-post lamina design.

To determine the impact of lamina design and defects on residence time distribution through the dialyzer device, all four lamina types were tested. Data collected from the pulse response sensitivity method were utilized for the slim-header and wide-header lamina designs. The wide-post lamina design was tested at 0, 4, 8, 16, and 24 blocked channels conditions and the all-posts lamina design was tested at no blockage, a blockage with volume similar to 4, 8, 16, and 24 blocked channels for the wide-posts lamina design. For these experiments, only one assembly was made for each design, followed by 3 measurements, as apposed to 3 assemblies in the previous study. This was because testing the variation between assemblies of the same lamina and condition were important to determining the sensitivity and ability to replicate measurements in validating the pulse response test loop but beyond that, to determine the residence time distribution of the lamina, it was not necessary to again verify the assembling process. Again, all experiments were conducted with deionized water at a flow rate of 0.768 ml/min.

4.8 Bringing Pulse Response Test Loop into Statistical Control

Development of the pulse response test loop required bringing the measurement system into statistical control to a tolerable level that would allow us to proceed into the investigation of sensitivity levels and lamina designs.

4.8.1 High Special Cause Variation

The first problem that was addressed was the high level of special cause variation between measurements. Process variation can be classified into two types: special cause and common cause. Common cause variation results from situations within the system and processes that are ongoing, chronic and persistent. This is the

random variance that is unavoidable in all instrumentation and process. Special cause variation is a result of sentinel events, one-time occurrences, or unique out-of-the-ordinary circumstances. These are events or process that that were not intended in the design of the system. Some examples include operator error or misalignment of parts resulting in bias.

Preliminary tests of the slim-header and wide-header design gave a mean residence time of 14.7 seconds and 15.1 seconds, respectively. Table 3 shows the average mean residence time (MRT) for both designs, along with the average range per assembly. The mean residence time was too high with respect to the time occupied by the lamina flow. Additionally, the high average range per assembly limits the sensitivity of the test loop. In order to have a significant difference in mean residence time distribution between control and defect conditions, approximately 30% of microchannels would need to be blocked, based on volume/flow rate calculation predictions. Another sign that the system is operating with special cause variation is the non-normal distribution shape of their histograms (Figure 40).

Table 3 Preliminary measurements of average mean residence time and average range for design 1 and design 2.

	Design 1	*Design 2*
Average MRT for assemblies (s)	14.7	15.1
Average range per assembly (s)	2	1.4

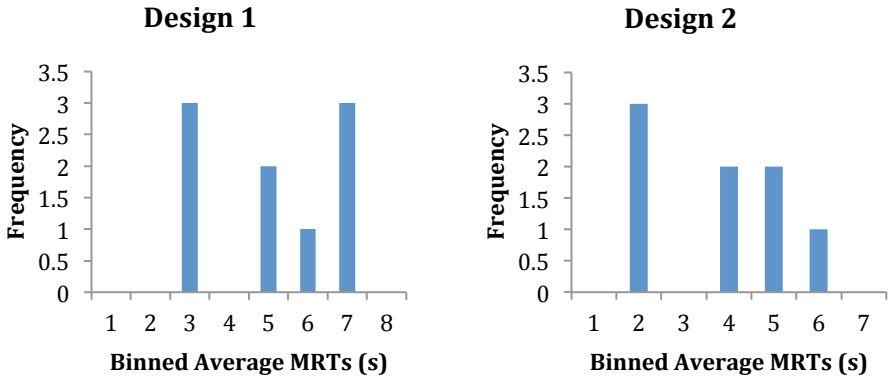

Figure 40. Histograms of slim-header (design 1) and wide-header (design 2) average MRT values.

The high mean residence time can be attributed to a large amount of extraneous or noncritical volume in the test loop. Extraneous volume is unavoidable in a system such as this where the full device is "plugged in" to the test loop instead of building measurement techniques into the lamina and device. Instead, we must minimize the extraneous volume. A proposed solution was replacing the original glass capillary tubes with Radel tubing and to move the fitting nut into a nested position within the platen via a counterbore-type feature. The capillary tubes would often break during assembly and disassembly, requiring their replacement. This led to slight variations in inner diameter and alignment that affected volume and flow path of tracer between assemblies. The capillary tubes were also restriction to one large inner diameter (~1mm) resulting in a significant portion of system volume existing outside of lamina resulting in dampening of the "critical" volume or signal. We were constrained with capillary size in order to 1/16" fittings used in out device. The Radel tubing comes in smaller inner diameter sizes while still retaining the same outer diameter in order to fit properly through the flow cells. They are also physically strong, with similar properties to PEEK, and therefore the chance of breakage is eliminated, providing consistent assembly. There is a compromise in transparency of Radel versus glass but this was tolerated and ultimately did not hinder the absorbance measurement. These two changes resulted in a 3.6 second reduction in mean residence time from 14.7 to 11.1.

4.8.2 Tubing Size Selection for Flow Cells

A question that arose from these modifications was which type of inner diameter tubing should be used in the inlet and outlet flow cells and should they be the same. We chose 0.01" I.D. for the inlet flow cell in order to limit the time between injector and device but also to reduce the axial laminar dispersion and increase radial diffusional dispersion. This promotes a more uniform dye concentration across the cross section of tubing that the absorbance measurement is taken, resulting in a more accurate measurement and ultimately the ability to close the dye mass balance on the system. At the outlet flow cell we tested 0.01" or 0.03" I.D. tubing. The 0.03" I.D. tubing provides higher absorbance sensitivity due to a longer path length across the tubing but at a cost of increased extraneous volume to the system.

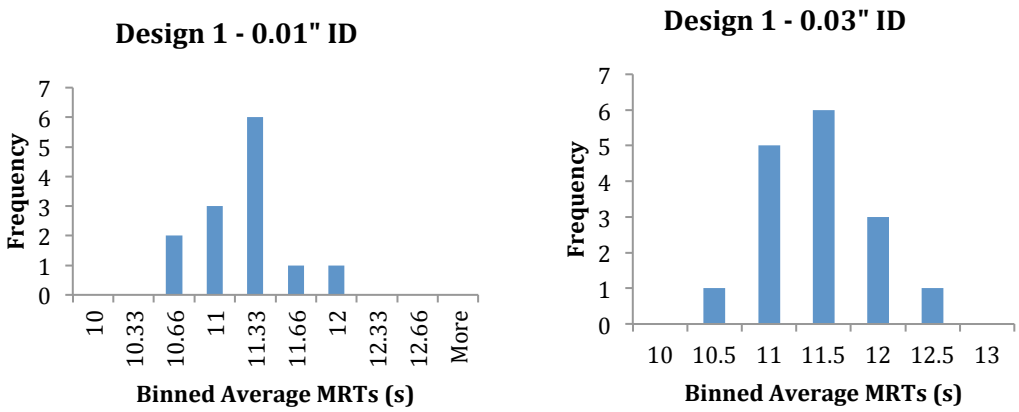

Figure 41. Histograms of slim-header (design 1) average MRTS for 0.01" and 0.03" I.D.

Based on histograms of pooled results from multiple assemblies and multiple days of experiments, even though we see variance in MRT between assemblies or experiment days, the 0.03" I.D. flow cell results show more of a bell shape in variance, which is indicative of common variation as apposed to special variation. The smaller 0.01" I.D. was more difficult at accurately aligning with fiber optic heads. 0.03" ID shows improved sensitivity in reading absorbance and scales linearly by a factor 2.9 with 0.01" I.D. as predicted (~3). We were also constrained to 0.03" I.D. for the outlet due to leaking that was observed from 0.01" ID as it increased

pressure drop at the outlet. Ultimately, we were able to acquire 0.02" I.D. tubing that served as a compromise between the other two tubing sizes.

After incorporating the Radel tubing and sinking the tube fittings into the platen, the range was still higher than what would qualify for a controlled process. Average MRTs (4 measurements taken per assembly) from assembly to assembly varied outside of the control limit range for the 0.03" ID tubing suggesting that there was still unknown special cause variation occurring between experiments. We could determine that this variance was related to assembly because range values for assembly data sets fall within their control limits. Additionally, the standard deviation for assembly MRT averages could be reduced, bringing the test loop system into better control for experimental measurements.

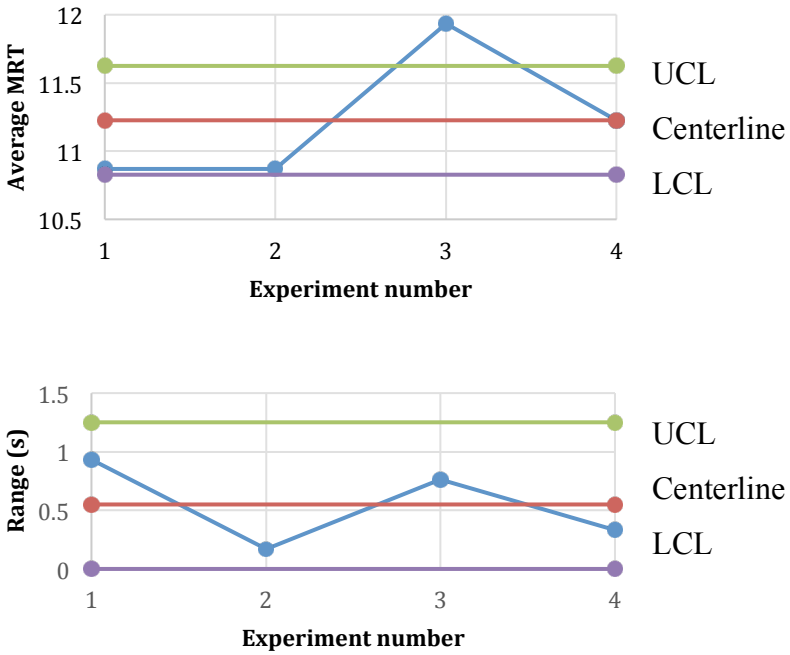

Figure 42. The results for average MRT and ranges for design 1 are overlayed with their respective control limits to determine if the process is operating within control.

Now that the system utilizes radel tubing in the flowcells, the only parts disassembled between experiments were lamina and PDMS sealing layers. By using commercial grade PDMS (controlled thickness and slight opaqueness) the PDMS layers could be laser trimmed to contain alignment holes and more precisely aligned and sized fluid through holes. After assembling PDMS on PC platens, they were not

removed between runs and only rinsed clean with isopropanol and water. This also minimized misalignment of through holes in PC platen, PDMS and PC lamina.

Although the bottom PDMS, between platen and non-channel side of lamina, seemed to help fluid flow, sagging of the top PDMS into the header region repeatedly occurred, inhibiting measurement of an ideally operating system. This is because the thinness of the PDMS allowed pooling of small air pockets (unavoidable when system is not under sealing pressure) into the non-clamped header region on the non-fluid side of the top PDMS layer. By switching to a thicker lab-made PDMS, it provided a smoother surface (fewer air pockets) and stiffer formulation to minimize sagging. Because the top layer doesn't contain fluid through holes, this does not impact improvements gained by the laser trimmed bottom PDMS. Figure 40 shows the assembly with sagging PDMS layer and non-sagging PDMS layer in the header region with blue dye injected into the fluid flow.

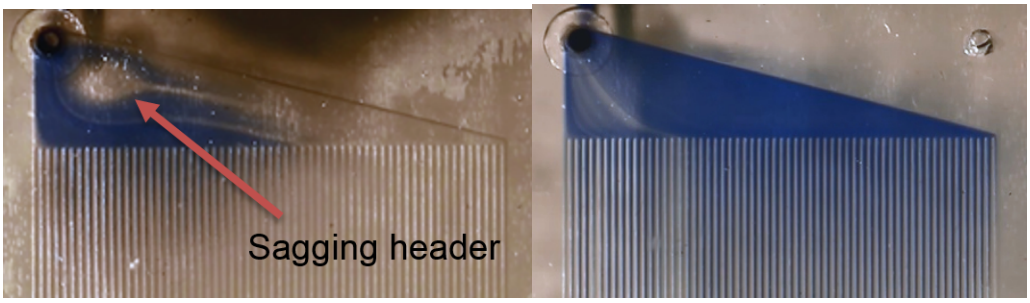

Figure 43. The sagging header on the left is with the thinner PDMS layer sealing against the header. The functional header on the right is with the thicker PDMS layer to correct for sagging. Note the difference in flow path of blue tracer dye.

After incorporation of these design improvements as a result of the PDMS layers, the range for average MRTs for design 1 and 2 decreased to more acceptable values. The average MRT for Design 1 still breached the upper control limit but by 0.01 seconds as apposed to 0.31 seconds in the previous test loop iteration. The assembly-to-assembly standard deviation in average MRT was reduced from 0.503 to 0.302 sec for Design 1 and is now 0.114 sec for Design 3.

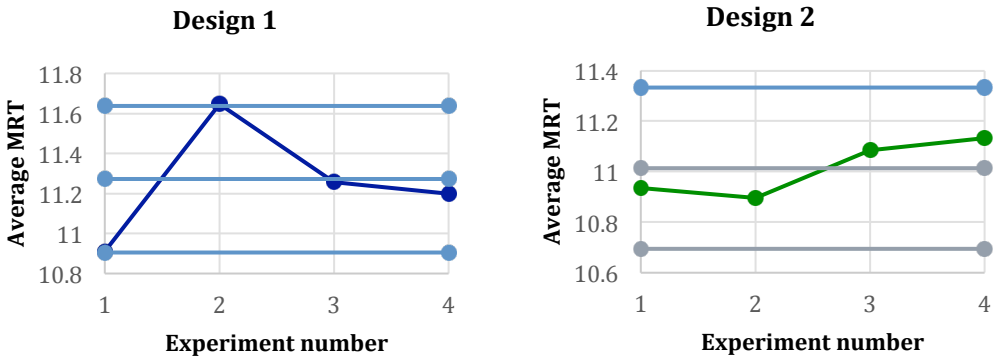

Figure 44. The average MRTs for design 1 and 2 in comparison to their control limits.

Collectively, all of these design changes discussed above resulted in decreased mean residence times due to decreased extraneous volume. There was also a decrease in the predicted sensitivity of the pulse response method for detecting blocked channels (channel/St.Dev. +10%) from 17 channels for design 1 and 24 channels for design 2, down to 4 channels for both designs. The P-value with respect to the impact of assembly of device was 0.17456, up from 0.0003, and with respect to lamina design, the P-value was 0.02361, down from 0.175. This indicates that the lamina design itself is has a more significant role in dictating the change in values of MRTs versus special cause variance that arises from assembly of the device.

5 NUMERICAL POST PROCESSING AND ANALYSIS

5.1 Normalization and Noise Reduction of Pulse Response Measurements

Signal noise arising from the spectrophotometers increased noise present in the deconvoluted residence time distribution as a result of increasing the ill-posedness of the linear equation. Before deconvoluting, noise reduction filters were applied to pulse response data: inlet and outlet data sets.

Negative values and those approaching zero were rounded to zero. Theoretically, the absorbance measurement should not yield negative values based on the experimental system. Negative values arose from noise variation straying large enough to cross below zero. In order to round these values to zero, a threshold level was set to 0.01% of the maximum value in the data set that revalued them as zero. Appendix B.3 lists an example of the Matlab code used for this procedure.

After setting baseline values to zero, the inlet and outlet data sets were renormalized to account for any variation in the integral of the inlet and outlet profiles. A difference in the area under the curve of these profiles would essential create a loss or creation of mass between the data sets, violating the closed system assumption. This would then be reflected later in the residence time distribution accounting for more or less than 100% of the mass.

Normalizing data was accomplished by multiplying each value in the inlet and outlet data arrays by their respective time step, followed by summing the resulting arrays separately (inlet and outlet) and dividing the original data array values by this sum (see Equation 11). Appendix B.4 shows an example of the Matlab code used to calculate this procedure.

$$normalized\ value\ (i) = \frac{original\ value\ (i)}{\sum original\ value * time\ step} \qquad \text{Equation 11}$$

Process for normalizing data sets

```
% calculate DeltaTime, the time step for inlet (1) and the outlet
(2)
DeltaTime1 = time1(2)-time1(1);
DeltaTime2 = time2(2)-time2(1);

% define the denominator
D1 = abso1*DeltaTime1;
D2 = abso2*DeltaTime2;
Denom1 = sum(D1);
Denom2 = sum(D2);

% normalize density (E1 & E2)
E1 = abso1/Denom1;
E2 = abso2/Denom2;
```

The processed data up to this point was utilized for calculating mean residence time (MRT) of the various pulse response measurements for the study regarding the effectiveness of the test loop and method for defect detection. This is because the MRT does not necessarily need the residence time distribution in order to calculate the value although the MRT does arise naturally from the RTD.

Before using pulse response results for deconvolution, the input and output signals were filtered in order to reduce the level of noise that would arise in the RTD. Again, this reduction in noise does not remove important feedback from the system, only instrument noise, as any high frequency information from the pulse response test loop is already dampened out by the effect of dye diffusion through the system. The filter implemented was a standard floating average filter (smooth) built into Matlab that was adapted for the input (sharper peak) and output (wider shape) to minimize over dampening. A slope fitting function (polyfit) was used to determine the "steepness" of the data at individual points and then widen or shrink the span length of the smoothing filter accordingly. For the inlet profile, a local slope (comprising an 8 unit span length linear regression centered from the specific point) was determined and if the slope was less than -0.25 and/or point was left of the profile peak, the absorbance value was left as is. If the slope was greater than -0.25 and right of the

profile peak, the absorbance value was replaced with the filtered value (floating average, span length = 7 units). For the outlet profile, if the slope (linear regression over span length of 14 units) was less than -0.012, the data point was filtered with a floating average filter spanning 9 units and above -0.012, with a floating average filter spanning 41 units. This is because as the tail of the profile moved towards the end and became flatter, the noise begins to dominate the signal itself and needs to be more aggressively filtered. An example of the Matlab code is shown below and a full copy of the code is listed in

Example of filtering absorbance data before deconvolution

```
% abso1 is the inlet data;
% abso2 is the outlet data;
%define length of absorbance arrays
L1 = length(abso1);
L2 = length(abso2);
% determine maximum peak location
[h1,i1] = max(abso1);
[h2,i2] = max(abso2);
% define slope width
m = 4;
n = 7;
L3 = 1+n;
% renamed to avoid errors
abso1s = abso1;
abso2s = abso2;
% filtered data sets formed which will then be selected from for
final
% arrays
abso1_s7 = smooth(abso1,7);
abso2_s9 = smooth(abso2,9);
abso2_s41 = smooth(abso2,41);
% inlet
for j = i1+m:L1-m;
    slope1 = polyfit (time1(j-m:j+m),abso1(j-m:j+m),1);
    if slope1(1,1) < -0.25
        abso1s(j) = abso1(j);
```

```
    else
        abso1s(j) = abso1_s7(j);
    end
    if abso1(j) < 0
        abso1s(j) = 0;
        else
    end
end
%outlet
for g = 1:L2-n;
    if g > n
        if g > i2+(30+n)
            slope2 = polyfit (time2(g-n:g+n),abso2(g-n:g+n),1);
            if slope2(1,1) < -0.012
                abso2s(g) = abso2_s9(g);
            else
                abso2s(g) = abso2_s41(g);
            end
        else
            abso2s(g)=abso2_s9(g);
        end
    else
    if abso2(j) < 0
        abso2s(j) = 0;
        else
    end
    end
end
```

5.2 Deconvolution

In order to generate the residence time distribution profile, the pulse response measurement, consisiting of an input and output concentration profile, must be deconvolved. Equation 7 is the convolution integral stated earlier and redisplayed here for convenience. Remember that $a(t)$ and $b(t\text{-}t')$ represent the output and input functions/profiles respectively.

$$a(t) = \int_{-\infty}^{\infty} b(t - t')g(t')dt' \qquad \text{Equation 7}$$

If $g(t')$ is a instantaneous pulse (dirac delta function) occuring at t_0, $a(t)$ and $b(t\text{-}t')$ take on similar shapes, with only the magnitude of $a(t)$ changing to account for $g(t')$. If $g(t')$ is not a dirac delta function and instead a different function, ex. gaussian profile, $a(t)$ is the summation of the convolution of the family of instantaneous pulses that could be imagined to form the $g(t')$ profile. Equation 7 is the convolution stated in a continuous form and is useful for many applications. This work involves discrete data sets collected experimentally and thus a more applicable form of the convolution integral is the matrix form below (Equation 12):

$$o = \boldsymbol{s} \cdot i \qquad \text{Equation 12}$$

where 'o' is a column vector containing the output response profile, '$\boldsymbol{s}$' is the coefficient matrix containing the system response function, and 'i' is the column vector containing the input profile. Due to the communicative property of the convolution integral, 's' convoluted with 'i' yields the same result as 'i' convoluted with 's'. This is useful because it allows equation 12 to be rearanged so that the coefficient matrix is composed of the known input profile values and the system response becomes a variable column vector that can be solved for (see Equation 13).

$$o = \boldsymbol{i} \cdot s \qquad \text{Equation 13}$$

We are now presented with a very familiar linear set of equations. The $\boldsymbol{i}$ matrix is a toeplitz matrix with the maximum value of the input profile aligned at the $\boldsymbol{i}$ (1,1) position and continuing down the column. This modification increases the diagonal dominance of the matrix but also requires the output vector to be shifted down so that the initial sampling points are completely convoluted. A reasonable approach would be to invert the '$\boldsymbol{i}$' matrix and take the dot product of $o*\boldsymbol{i}^{-1}$ to arrive at

'*s*' but due to experimental noise and the matrix lacking complete diagonal dominance, iterative techniques must be employed to arrive at a converging solution.

The Gauss Seidel iterative solving method (Equation 14) was employed. The Gauss Seidel method, also know as a point successive relaxation method, solves each equation set in terms of the variable associated with the diagonal coefficient.[75] This is similar to the Jacobi method but the Gauss-Seidel method differs by constantly updating the old values of 's' with the most recent new guesses instead of sweeping through the entire equation set and then updating values.

$$s_i^{(k+1)} = s_i^{(k)} + \frac{1}{s_{ii}}\left(o_i - \sum_{j \geq i} i_{ij} s_j^{(k)} - \sum_{j<i} i_{ij} s_j^{(k+1)}\right), \quad i = 1,2,\ldots, n$$

Equation 14

A Condition statement has been defined in the solver to constrain solutions based on our physical understanding of the test loop system. The condition is 'no negative values' based on the assumption that mass is not destroyed in the system. If the solution drift into the negative values which can occur in ill-conditioned problem sets, especially when the noise increases, those values are reset to zero and the solver continues computing. Below is the Matlab code for running this iterative solver. This code does not include the matrix transformations discussed above (that Matlab script can be reference in Appendix B.6).

Main portion of modified Gauss-Seidel interative solver

```
...
% loop will run until one criteria in last 'if' is satisfied
while (1)
    %separating old and new x values
    xold = x;
    for i = 1:n
        % ex.: x1 = b1/a1 - a2*x2/a1 - a3*x3/a1 -...
        x(i) = d(i)-C(i,:)*x;
        % condition: no negative values
        if x(i)< 0
```

```
            x(i)=0;
        end
        % calculating error and storing value
        if x(i) ~= 0
            ea(i) = abs((x(i) - xold(i))/x(i))*100;
        end
    end
    % bump iteration # up 1 each cycle
    iter = iter+1;
    % criteria: maximum error equal or less than error specified
    % iteration number reaches maximum
    if max(ea)<=es || iter >= maxit, break, end
end
...
```

The input and output response profiles were resized with respect to array length in order to be of matching sizes. This is necessary to solve the linear equation set. Their variance in length is a result of small differences between the two spectrophotometers that require different integration times to maximize the sensitivity of each detector. In all cases for this work, the longer data set was resized to the smaller data set and no further in order to minimize information loss. This was performed via the built-in "interp1" Matlab function that uses linear regression to resize a matrix. This was incorporated into the deconvolution function code listed in Appendix B.7.

The maximum number of iterations was set at 200 cycles as it was observed that if a solution did not converge below the error threshold of 0.01, the system plateau at a close approximation of the solution with noise slowly increase with each iteration.

5.3 RTD Characterization Values

Moments of the RTD were calculated from the pulse response measurements and residence time distributions to determine the sensitivity of the test loop and compare experimental groups. The three primary values calculated were mean

residence time, variance of the residence time distribution, and skewness of the residence time distribution.

The mean residence time (MRT) or 'τ' is calculated by the first moment of the distribution and was calculated from both pulse response data and residence time distribution. The equation for mean residence time is:

$$\tau = \frac{\sum t_i C_i}{\sum C_i} \qquad \text{Equation 15}$$

For the pulse response data, the MRT was calculated for both input and output data and then difference of the two values gives the MRT of the system. Calculating the MRT by both methods arrives at approximately the same value, with differences arising due to effects from filtering or inability of a specific linear equation set to fully converge.

The variance ($\sigma(t)^2$) is equivalent to the second central moment in the distribution and was calculated by the following equation:

$$\sigma(t)^2 = \frac{\sum (t_i)^2 C_i}{\sum C_i} - \tau^2 \qquad \text{Equation 16}$$

The variance can only be calculated from the residence time distribution and was used to compare dispersion within the system for different lamina and blockage conditions. Using the variance and MRT, a dimensionless variance ($\sigma(\theta)^2$) can be calculated that quantifies variance with respect to average fluid age (see Equation 17). This allows for comparison between the different lamina designs as each had slightly different total volumes for the fluid flow path.

$$\sigma(\theta)^2 = \frac{\sigma(t)^2}{\tau^2} \qquad \text{Equation 17}$$

Another value calculated from the RTD is the skewness 's' of the profile. The equation for skewness is shown below (see Equation 18). It is a value that describes the asymmetry of a distribution. There are varying definitions of how to calculate the value and it can be a misleading value when presented with special conditions such as

multiple peaks. For most of the RTD's measured in this study, the distribution consists of a tall single peak and therefore the skewness is appropriate to use but there are scenarios when a hemodialyzer can show multiple peaks in the RTD, such as when two discrete flow paths exists due to obstruction.

$$s = \frac{\sum((t_i - \tau)^3 C_i}{\sigma^3 \sum C_i} \qquad \text{Equation 18}$$

6 MATHEMATICAL MODEL DEVELOPMENT AND SIMULATION

Modeling studies were done in collaboration with colleague, Agnieszka Truszkowska and credit goes to her for model and code development and performing simulations. The methods for developing the mathematical models and simulations are shared here.

6.1 Lattice Boltzmann Model Development

A mathematical model was developed that would allow for numerical simulation of a bubble passing through a single microchannel with characteristics of PEO coated and uncoated lamina. Simulation results were compared with experimental results from the PEO coating study to determine the influence of liquid film between bubble and channel walls on two-phase flow through a single microchannel.

Numerical simulations were based on Lattice Boltzmann Modeling (LBM) method; specifically, the Shan and Chen multicomponent multiphase method was utilized [76]. Investigation of wall wettability on the two-phase flow using LBM modeling method was also previously conducted by Fei et al. [77]

The discrete Boltzmann equation for the density distribution of each species ξ is given by:

$$\underbrace{f_a^{\xi}\left(\mathbf{x}+\mathbf{e}_a\Delta t, t+\Delta t\right)=f_a^{\xi}\left(\mathbf{x},t\right)}_{\text{Streaming}}-\underbrace{\frac{\Delta t}{\tau_{\xi}}\left[f_a^{\xi}\left(\mathbf{x},t\right)-f_a^{\xi,eq}\left(\mathbf{x},t\right)\right]}_{\text{Collision}} \quad \text{Equation 19}$$

With the equilibrium distribution function defined as:

$$f_a^{\xi,eq}\left(\mathbf{x},t\right)=\omega_a\rho_{\xi}\left[1+\frac{\mathbf{e}_a\cdot\mathbf{u}_{\xi}^{eq}}{c_s^2}+\frac{\left(\mathbf{e}_a\cdot\mathbf{u}_{\xi}^{eq}\right)^2}{2c_s^4}-\frac{\left(\mathbf{u}_{\xi}^{eq}\right)^2}{2c_s^2}\right] \quad \text{Equation 20}$$

Macroscopic density and velocities are computed as:

$$\rho_{\xi}=\sum_{a=0}^{8}f_a^{\xi} \quad \text{Equation 21}$$

and

$$\mathbf{u}_{\xi} = \frac{1}{\rho_{\xi}} \sum_{a=0}^{8} f_a^{\xi} \mathbf{e}_a \qquad \text{Equation 22}$$

Equilibrium velocity in the Equation 23 incorporates composite velocity resulting from presence of the two fluids and forces acting on them;

$$\mathbf{u}_{\xi}^{eq} = \mathbf{u}' + \frac{\tau_{\xi}}{\rho_{\xi}} \left[\mathbf{F}_{a,\xi} + \mathbf{F}_{r,\xi} + \mathbf{F}_{ads,\xi} + \mathbf{F}_{ext,\xi} \right] \qquad \text{Equation 23}$$

Forces represented in the Eq. 5 are: attraction and repulsion force, [$\mathbf{F}_{a,\xi}$] and [$\mathbf{F}_{r,\xi}$] respectively, between species present in nodes, interaction force with solid wall, [$\mathbf{F}_{ads,\xi}$], and external force [$\mathbf{F}_{ext,\xi}$] such as gravity. Properties of species (water and air) as well as their interactions with solids were adopted from Huang et al. [31] A two-dimensional D2Q9 lattice model was implemented, using the same characteristic channel dimension as in performed experiments. Values of contact angles used in this LBM simulation match closely water/ PEO and water/polycarbonate static contact angles, which was verified through numerical calibrations. In all cases when a liquid film was initialized between the bubble and the channel wall, Equation 24 was used based on a relation provide by Aussillous and Quéré [76].

$$h = \frac{0.67 Ca^{2/3}}{1 + 3.35 Ca^{2/3}} D_H \qquad \text{Equation 24}$$

The above relation for film thickness also provides a guideline for computational grid choice. We used uniform, rectangular grid with varied grid size as needed in any particular simulation. Grid size for each simulation was guided by Equation 24 to provide at least three grid elements across the lubrication film. The height of the 2-D microchannel was 154 micrometers to match the hydraulic diameter of the lamina microchannels.

6.2 Multi-Segmented CFD Simulation of Pulse Response Tracer

A mathematical model for RTD analysis was developed based on first principles and the numerical simulations were computed using *COMSOL* Multiphysics software. The equations and assumptions applied are listed below. Due

to the complexity of the hemodialyzer geometry, even after applying the following assumptions, the numerical model remains complex.

Assumptions

1. Fluid velocity is at steady state (all derivatives with respect to time are zero).
2. Mass transfer is transient.
3. Fluid is at constant density, viscosity and temperature.
4. No slip condition applied to the channel wall.
5. Negligible contribution of gravity to fluid flow and can be ignored in mass transfer (neutral densities of tracer solution and DI water).
6. Fluid flow occurs in x, y, and z-directions.
7. Mass transfer occurs in x, y, and z-directions.
8. No reactions occur

Mathematical Model

The Navier-Stokes equations for the rectangular coordinate system (x, y, z) are as follows:

x component (Equation 25a):

$$\rho\left(\frac{\partial u_x}{\partial t}+u_x\frac{\partial u_x}{\partial x}+u_y\frac{\partial u_x}{\partial y}+u_z\frac{\partial u_x}{\partial z}\right)=-\frac{\partial P}{\partial x}+\mu\left(\frac{\partial^2 u_x}{\partial x^2}+\frac{\partial^2 u_x}{\partial y}+\frac{\partial^2 u_x}{\partial z^2}\right)+\rho g_x$$

y component (Equation 25b):

$$\rho\left(\frac{\partial u_y}{\partial t}+u_x\frac{\partial u_y}{\partial x}+u_y\frac{\partial u_y}{\partial y}+u_z\frac{\partial u_y}{\partial z}\right)=-\frac{\partial P}{\partial y}+\mu\left(\frac{\partial^2 u_y}{\partial x^2}+\frac{\partial^2 u_y}{\partial y}+\frac{\partial^2 u_y}{\partial z^2}\right)+\rho g_y$$

z component (Equation 25c):

$$\rho\left(\frac{\partial u_z}{\partial t}+u_x\frac{\partial u_z}{\partial x}+u_y\frac{\partial u_z}{\partial y}+u_z\frac{\partial u_z}{\partial z}\right)=-\frac{\partial P}{\partial z}+\mu\left(\frac{\partial^2 u_z}{\partial x^2}+\frac{\partial^2 u_z}{\partial y}+\frac{\partial^2 u_z}{\partial z^2}\right)+\rho g_z$$

Due to the model having 3-dimensional flow, the only terms that can be removed from Equations 25(a-c) are those with respect to time based on Assumption

#1 and the gravity body force terms based on Assumption #5. Assumption #1 is based on our understanding that tracer will enter a system with fully developed flow. This yields Equations 26(a-c).

x component (Equation 26a):

$$\rho\left(u_x\frac{\partial u_x}{\partial x}+u_y\frac{\partial u_x}{\partial y}+u_z\frac{\partial u_x}{\partial z}\right)=-\frac{\partial P}{\partial x}+\mu\left(\frac{\partial^2 u_x}{\partial x^2}+\frac{\partial^2 u_x}{\partial y}+\frac{\partial^2 u_x}{\partial z^2}\right)$$

y component (Equation 26b):

$$\rho\left(u_x\frac{\partial u_y}{\partial x}+u_y\frac{\partial u_y}{\partial y}+u_z\frac{\partial u_y}{\partial z}\right)=-\frac{\partial P}{\partial y}+\mu\left(\frac{\partial^2 u_y}{\partial x^2}+\frac{\partial^2 u_y}{\partial y}+\frac{\partial^2 u_y}{\partial z^2}\right)$$

z component (Equation 26c):

$$\rho\left(u_x\frac{\partial u_z}{\partial x}+u_y\frac{\partial u_z}{\partial y}+u_z\frac{\partial u_z}{\partial z}\right)=-\frac{\partial P}{\partial z}+\mu\left(\frac{\partial^2 u_z}{\partial x^2}+\frac{\partial^2 u_z}{\partial y}+\frac{\partial^2 u_z}{\partial z^2}\right)$$

The velocity field map is solved initially; separate from mass transfer, as water is the continuous medium in a single species system. Decoupling the fluid dynamic problem from the mass transfer problem decreases the computational strain of the model, as the fluid velocity map is not resolved with each time step. The velocity map can then be overlaid on the transient mass transfer problem, which is then solved. The mass conservation equation for the mass transfer model contains all terms except reaction.

$$D_{21}\left[\frac{\partial^2}{\partial x^2}C_2+\frac{\partial^2}{\partial y^2}C_2+\frac{\partial^2}{\partial z^2}C_2\right]-\left[u_x\frac{\partial}{\partial x}C_2+u_y\frac{\partial}{\partial y}C_2+\ u_z\frac{\partial}{\partial z}C_2\right]=\frac{\partial}{\partial t}C_2$$

Equation 29

Throughout all of the simulations, the density of water was set to 999.62 kg/m^3 and the viscosity set to 1.0093 Pa-s. The diffusion coefficient of the tracer solute was set to $0.568x10^{-9}$ m^2/s based on Coomassie Brilliant Blue.

In order to compare simulation results with experimental results and determine validity of the model, we must model the entire test loop geometry between the inlet flow cell and outlet flow cell. A schematic of the dimensions of the

extraneous tubing and connections are shown in Figure 45. The resulting computational geometry was too complex for any the available computing resources to manage. It was decided to segment the model into three portions:

1. The inlet tubing from the inlet flow cell to the entrance hole to the lamina. (See Figure 46)
2. The microchannel lamina, including headers.
3. The outlet tubing consisting from the exit hole in the lamina to the outlet flow cell.

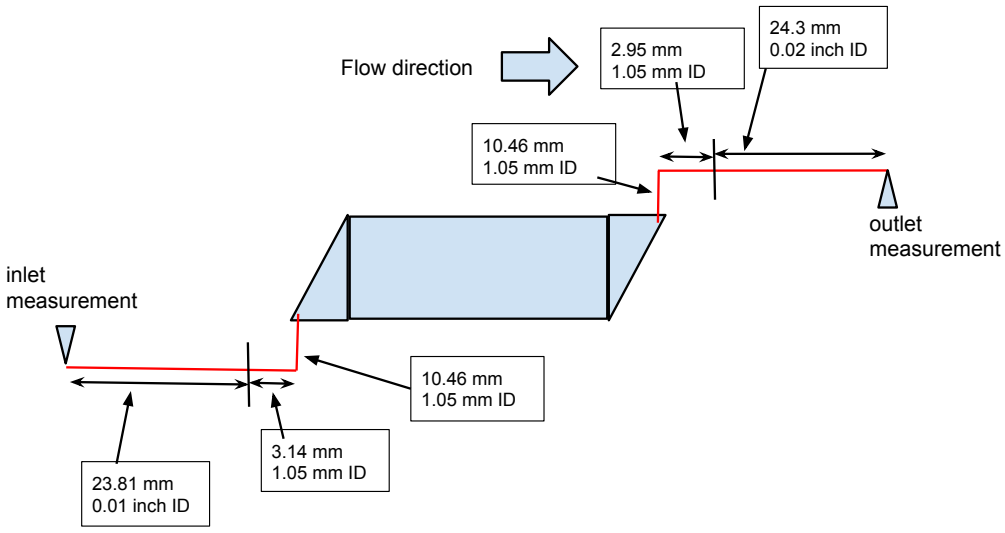

Figure 45. Schematic of the connecting tubing between the inlet flow cell to the lamina and from the lamina to the outlet flow cell.

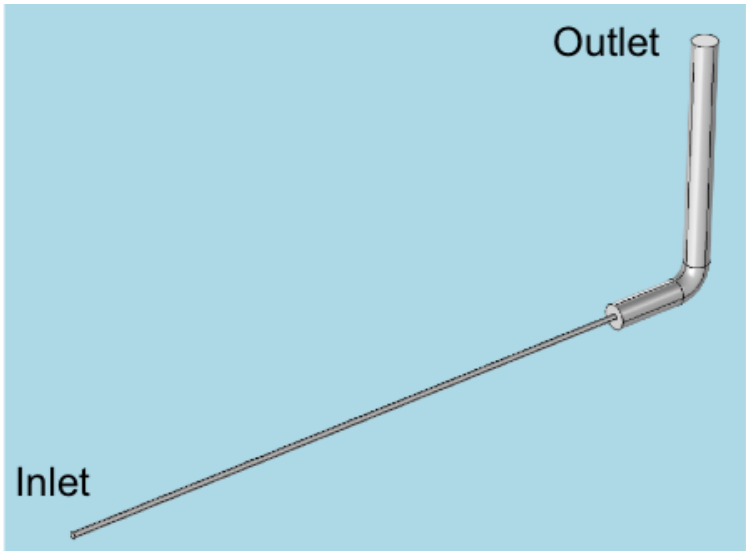

Figure 46. Example of 3-D entrance tubing geometry for first stage of numerical simulation. ***Image courtesy of Agnieszka Truszkowska.***

Unfortunately, even after simplification of the model into three discrete parts, segment 2, the lamina, was still too complex, resulting in unreasonably long solving time (estimated at multiple months). It was decided to apply the assumption of Hele-Shaw flow to the lamina geometry, moving from a 3-D model to a 2-D approximation. After this, all three parts of the model were now solvable within a week with available computing resources. Figure 47 is an image of the design 2 wide-header 2-D approximation geometry, showing that the model retains the same proportions and features sizes in the X-Y plane.

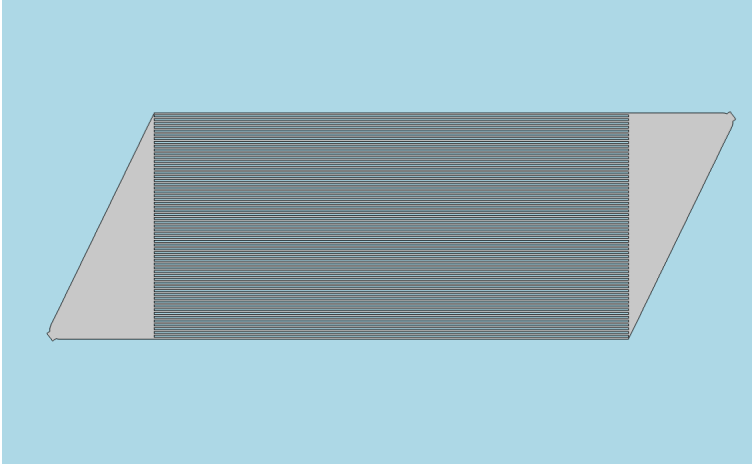

Figure 47. Example of 2-D lamina (design 2, wide-header) geometry for second stage of numerical simulation. ***Image courtesy of Agnieszka Truszkowska.***

COMSOL handles the 2-D approximation by adding a term to the right hand side of the Navier Stokes equations. The entire equation with the additional term stated below in vector notation for brevity (Equation 30).

$$\rho \mathbf{u} \cdot \nabla \mathbf{u} = -\nabla P + \mu \nabla^2 \mathbf{u} - 12 \frac{\mu \mathbf{u}}{h_z^2}$$

Equation 30

There are two transition regions between the three model segments. The first is at the end of the 3-D entrance-tubing model and the inlet hole of the 2-D lamina model. The second is at the outlet hole of the 2-D lamina model and the beginning of the 3-D exit-tubing model. At the outlet of one segment, the average tracer concentration was calculated at each time step and then that those averages were distributed uniformly across the inlet of the following segment.

There are two options for introducing 'tracer' into the numerical model. First, the tracer can enter the system as a Dirac delta function, which is feasible when working with computer models, and the outlet concentration is the RTD without the necessity to deconvolute. A second approach is to create the tracer profile by matching the concentration at the inlet of the model with respect to time to the experimentally measured inlet profiles. In this manner the outlet concentration can be directly compared to the experimental outlet concentration. We decided to utilize the second approach because it allows us to directly compare the model with

experimental results from the pulse response measurements without the added complexity of the deconvoluted RTDs.

The mean residence times were calculated using Equation 15 from Section 5.3. The material balance was calculated as relative difference between the total mass at the inlet and the outlet of each model segment and of the entire model as a whole. Total mass (m_{tot}) was obtained from *COMSOL* as the time integral of normal mass flux, Φ_n, across the inlet and outlet surfaces (S) (see Equation 31).

$$m_{tot} = \int_0^{t_f} \left(\int_S \Phi_n(t) dS \right) dt \qquad \text{Equation 31}$$

7 RESULTS

7.1 Effect of PEO Coating on Bubble Blockage in Microchannel Lamina

The percentage of obstructed channels for PEO-coated and uncoated lamina were measured at flow rates between 0.5 and 4.0 mL/min, corresponding to average nominal velocities between 0.9 and 7.2 cm/s for an unobstructed system.

The initial priming events for both coated and uncoated lamina were similar with nearly all microchannels channels filling with water and a few bubbles located in the exit manifold (Figure 48(B) and Figure 48(C)). This is attributed to the uniform filling of microchannels that occurs during priming, allowing for sufficient pressure to push air out of all of the channels. Figure 48(A) is an image of the microchannel system during priming. The dark region in the image is the gas phase and the lighter shade region is water entering the device. Notice that the microchannels fill somewhat simultaneously. Priming events for all flow rates tested were observed to follow this general behavior.

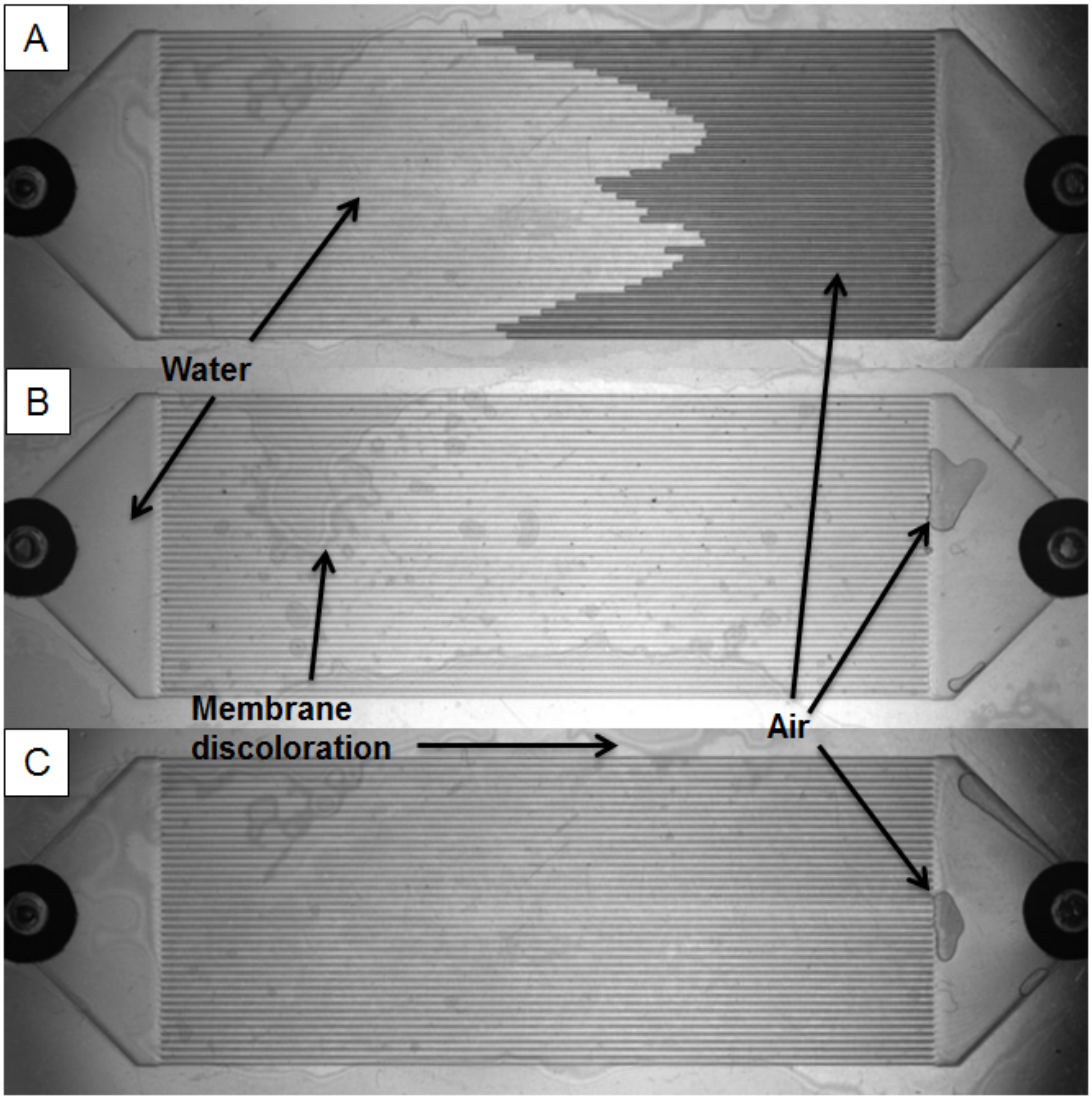

Figure 48. Priming the microchannel system at 0.9 cm/s average channel velocity for (A) coated lamina mid-priming event; (B) uncoated lamina after priming event, and (C) coated lamina after priming event. Fluid flow from left to right

Air bubbles introduced to the system entered the manifold and sectioned off into the microchannels (Figure 49(A)). This in turn restricted water flow path through the device and increased the pressure drop across the system, forcing bubbles to move through the channels. Compared to the more uniform channel filling occurring in priming, the injected bubbles would enter the manifold and microchannels in a disordered manner and various channels would clear out bubbles before other channels, resulting in a more gradual decrease in pressure drop across the system. This resulted in a few channels with bubbles remaining in them and

insufficient force from the liquid flow to continue moving the bubble to the exit manifold (see Figure 50).

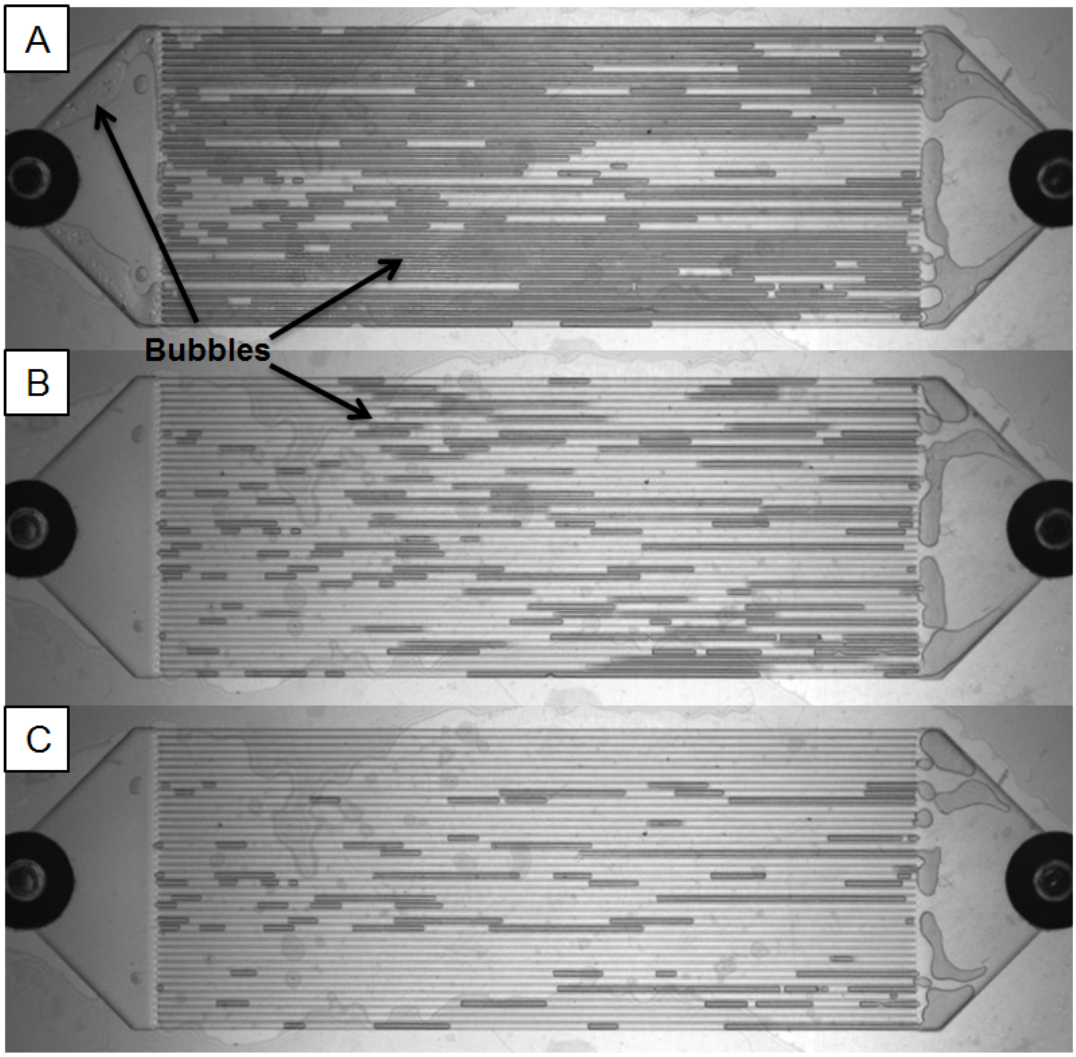

Figure 49. Train of bubbles injected into microchannel array. Uncoated lamina at 2.7 cm/s average channel velocity. (A) initial bubble injection; (B) 1 second after injection, and (C) 2 seconds after injection. Fluid flow from left to right

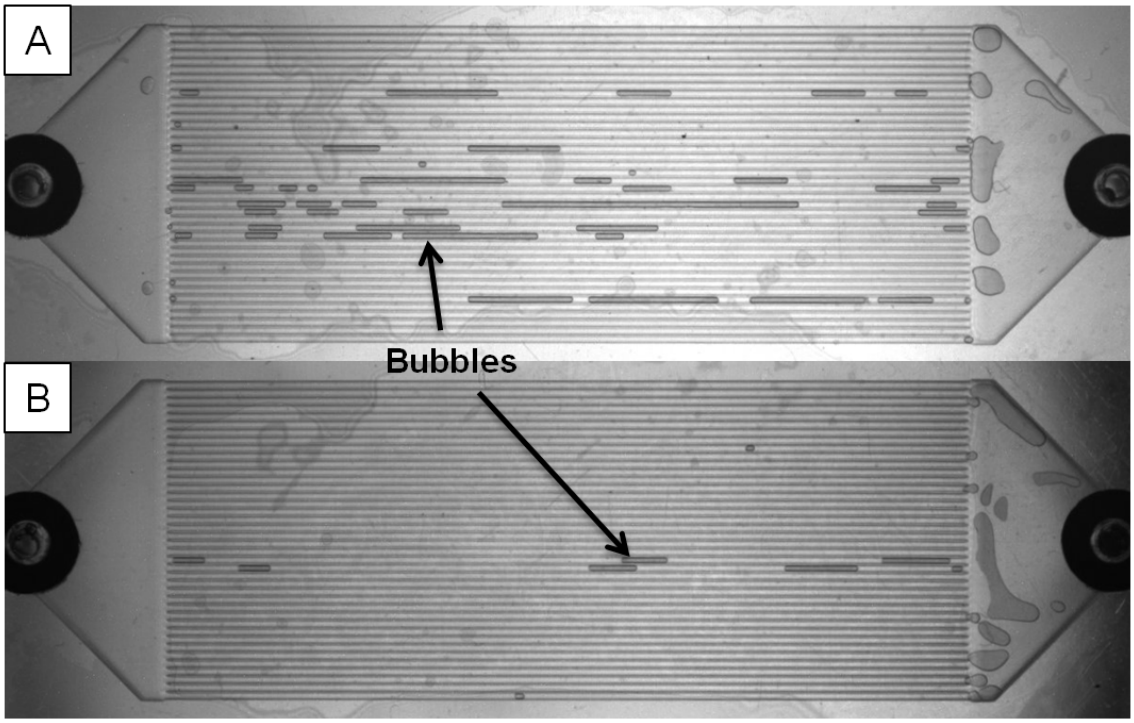

Figure 50. Channels obstructed by bubbles after allowing systems to stabilize, at 1.5 ml/min flow rate or 2.7cm/s average channel velocity for (A) uncoated lamina, and (B) coated lamina. Fluid flow from left to right

A higher number of bubbles were observed in the exit header versus the inlet header. This is due to the curvature of the bubbles in the z-direction (perpendicular to the lamina surface). The distance between the header bottom and membrane top is smaller near the inlet and outlet ports due to a sealing force applied at those regions. The sealing o-rings are two black circles in every photo of the lamina. The change in bubble curvature as it moves through the header has a beneficial effect in the inlet header and inhibits bubble movement in the exit header. This change in header depth can be remedied by incorporating support structures in the header.

Microchannel obstruction from bubbles decreases with increasing flow rate for both uncoated and coated lamina (Figure 51). This change is most dramatic between the average nominal channel velocities of 0.9 cm/s to 3.6 cm/s for both uncoated and coated lamina with the coated lamina showing fewer obstructed channels compared to uncoated lamina at these lower velocities.

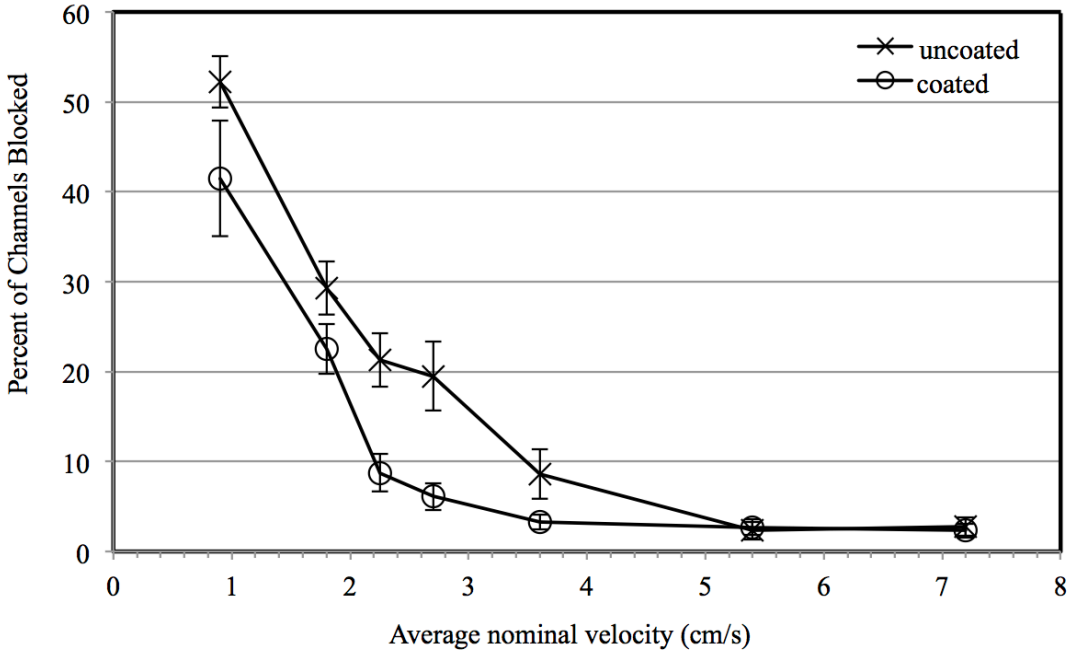

Figure 51. Percent of channels blocked by bubbles with respect to average channel velocity (cm/s) for uncoated (X) and coated (O) lamina. Error bars indicate one standard deviation

Using a student t-test, a significance level of α=5%, and $H_o: \mu_{uncoated} = \mu_{coated}$ the difference in mean channel blockage is statistically significant for the average channel velocities of 1.8, 2.25, 2.7, and 3.6 cm/s. Both uncoated and coated lamina systems achieve similar microchannel clearance at an average nominal channel velocity of 5.4 cm/s and both uncoated and coated lamina systems appear to reach a maximum microchannel clearance of approximately 39 cleared channels or 1 blocked channel out of the 40 microchannels. Complete bubble clearing occurs at much higher flow rates for both uncoated and coated lamina but leakage would occur in our system. Location of obstructed channels was also recorded. No discernible trend was found with respect to bubbles preferentially occluding specific channels.

7.2 LBM Simulation of Bubble Behavior in Microchannel

Numerical investigation of coating and corresponding contact angle influence on bubble mobility was accomplished by using a fixed pressure drop in both coated and uncoated channels, and by measuring the differences in resulting bubble velocities. Results complement experimental findings, indicating that the liquid film

formation facilitates faster bubble flow through the microchannel. To aid the analysis and assist in qualitative understanding, *model-pairs* (hydrophilic and hydrophobic model pairs) were created. The LBM-based simulation of each model-pair was performed at the same Reynolds number based on fluid velocity obtained in the hydrophilic modeling result.

Additionally the presence of a liquid film adjacent to the channel wall for hydrophilic channels and its absence in hydrophobic channels was confirmed by "challenging" the performance and stability of the model. In both cases, simulations were initialized counter to the anticipated result: i) a bubble was positioned away from the wall in a hydrophobic channel; and, ii) a bubble was positioned adjacent to the wall in a hydrophilic channel. Both simulations performed correctly by placing the bubble in contact with the hydrophobic channel wall and away from the wall in the more hydrophilic channel, at the end of the numerical simulation run when a steady state condition is approached.

Figure 52A and Figure 52B are graphical representations of the results obtained for the lowest velocity (pressure drop) simulation corresponding to Re = 1.7. The magnified views of the channel wall show either absence or presence of the liquid film as anticipated and confirmed earlier. Figure 52C and Figure 52D show graphical results from a higher fluid velocity (pressure drop) simulation, Re = 5.8. Again, a thin liquid film persists between the bubble and channel wall only for the hydrophilic condition. At this higher velocity, the bubble deforms into a bullet shape for both channel conditions. Finally, at even higher liquid velocity, a liquid film surrounds the bubble in both the hydrophilic and hydrophobic channel condition. This leads to a negligible difference in bubble velocities and shapes in between the two conditions. Table 4 summarizes bubble velocities obtained the eight simulations.

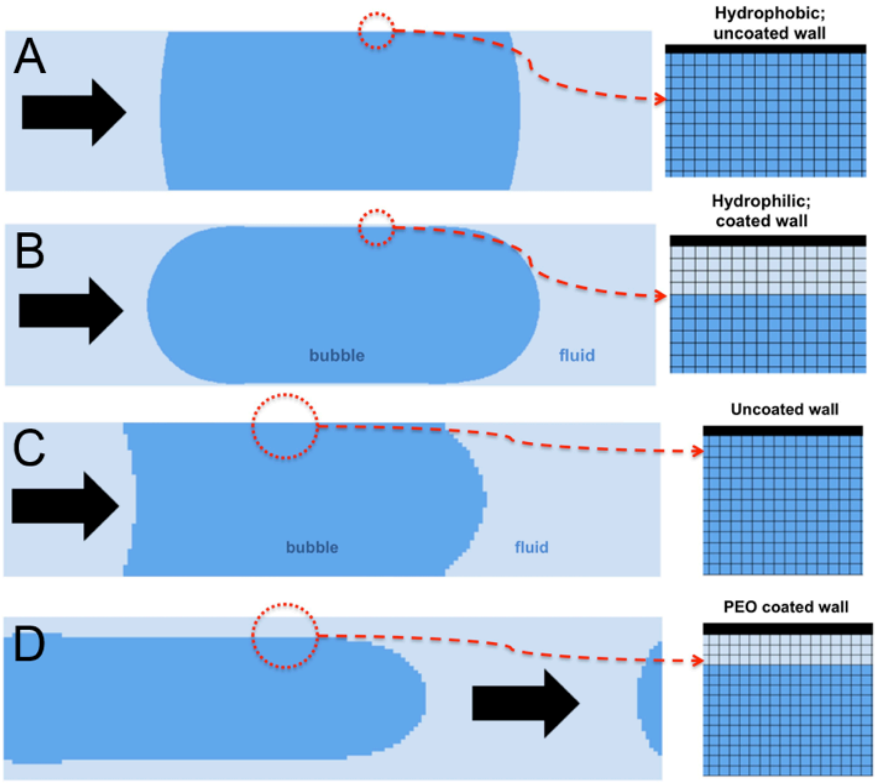

Figure 52. Bubble flowing through an (A) uncoated and (B) coated microchannel at Re=1.6 and Re=1.7, respectively. In the right, the area adjacent to the wall (black line) is highlighted. In the uncoated microchannel, the bubble is adjacent to the wall whereas in the coated microchannel a stable 4-grid cells thick liquid film forms. Further down, a bubble flowing through an (C) uncoated and (D) coated microchannel at higher Re = 4.7 and Re 5.8, respectively. On the right, the area adjacent to the wall (black line) is highlighted. In the uncoated microchannel, the bubble is adjacent to the wall whereas in the coated microchannel a visible liquid film has developed spontaneously without previous initialization. *Image courtesy of Agnieszka Truszkowska*

Table 4 Bubble velocity (cm/s) and corresponding Re through a single hydrophobic or hydrophilic microchannel for various conditions (pressure drop).

Condition	1	2	3	4
Hydrophobic channel Bubble velocity (cm/s), Re	1.0 Re=1.6	2.0 Re=3.1	3.1 Re=4.7	5.1 Re=7.8
Hydrophilic channel Bubble velocity (cm/s), Re	1.1 Re=1.7	2.3 Re=3.6	3.8 Re=5.8	5.1 Re=7.8
Relative difference, %	6.3	16.1	23.4	0

The shape of the front and trailing end of a bubble obtained in numerical simulation showed close likeness to the shape of slow and fast moving bubbles experimentally observed in our microchannel system (Figure 53). Both the numerical

simulation and experimental results show that at higher velocities the bubble begins to deform and take on a more bullet-like profile. The most exact comparison is possible only if the Reynolds number in every microchannel in the experimental microchannel array is correctly estimated due to redistribution of fluid flow among microchannels in the array.

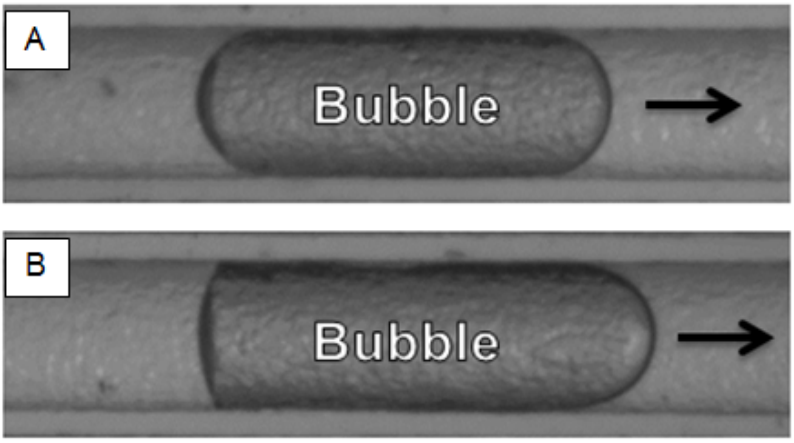

Figure 53. (A) Slow (Re < 2) and (B) fast (Re >2) moving bubble through water in the microchannel system.

7.3 Tracer Dye Flow Pattern through Laminas

The following images are captured from video recordings of the tracer dye flowing through the 4 different microchannel laminas at various obstruction conditions. All of the images in this section show flow from left inlet hole to right outlet hole of the dye either entering the lamina, flowing down the main portion (microchannel array or micro-post grid), or exiting the lamina. The dye concentration is higher in these experiment images to improve visual contrast but their flow patterns match very similarly with the dye concentration used for the pulse response measurements, which is expected. For each of the four lamina designs there are three images of the tracer flowing through the unblocked, control condition at different moments, along with an image of tracer flow through two different blockage conditions.

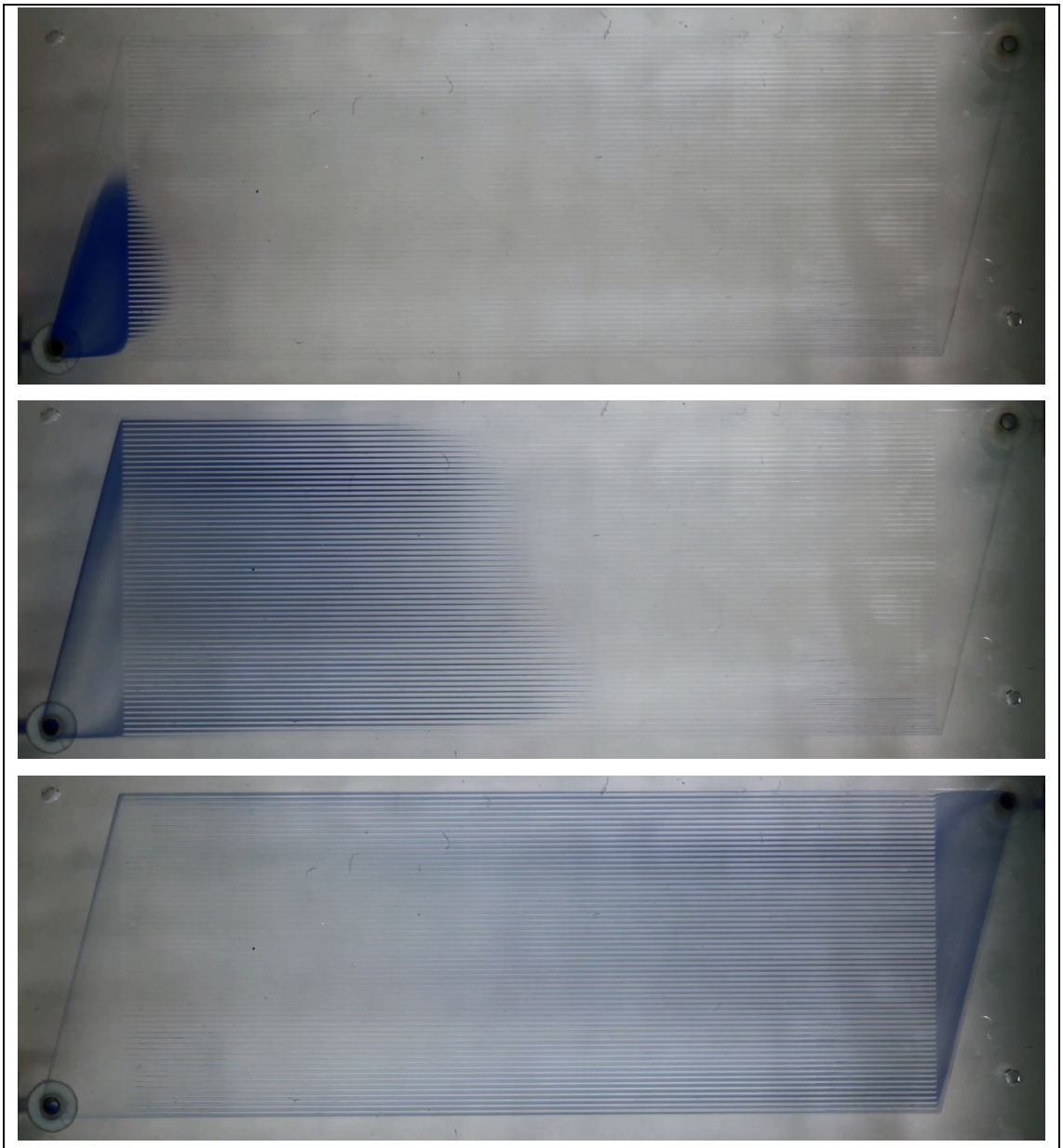

Figure 54. Design 1 Slim-header lamina with no blockage at 0.768 ml/min. (Top) Dye initially entering the lamina. (Middle) Bulk of the dye flowing down the channel array. (Bottom) Dye beginning to exit lamina. Flow from left to right.

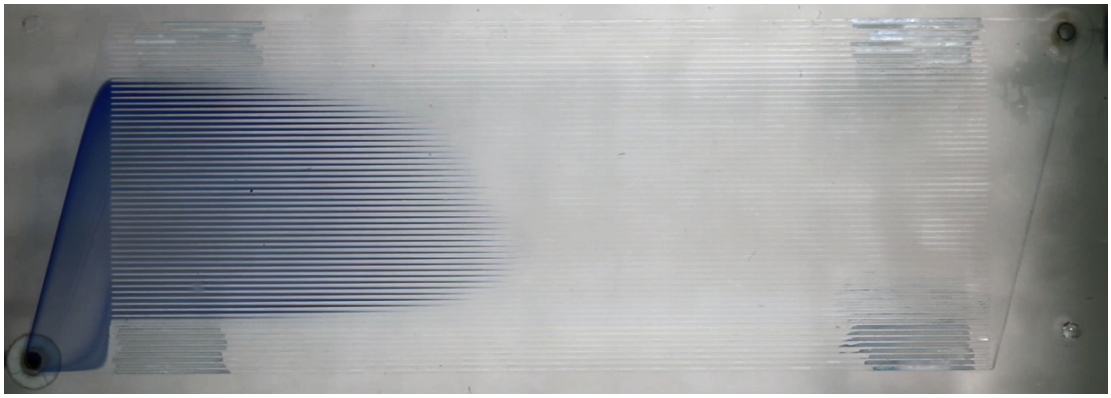

Figure 55. Design 1 Slim-header lamina with 16 blocked channels at 0.768 ml/min as the dye begins to flow down the microchannels. Flow from left to right.

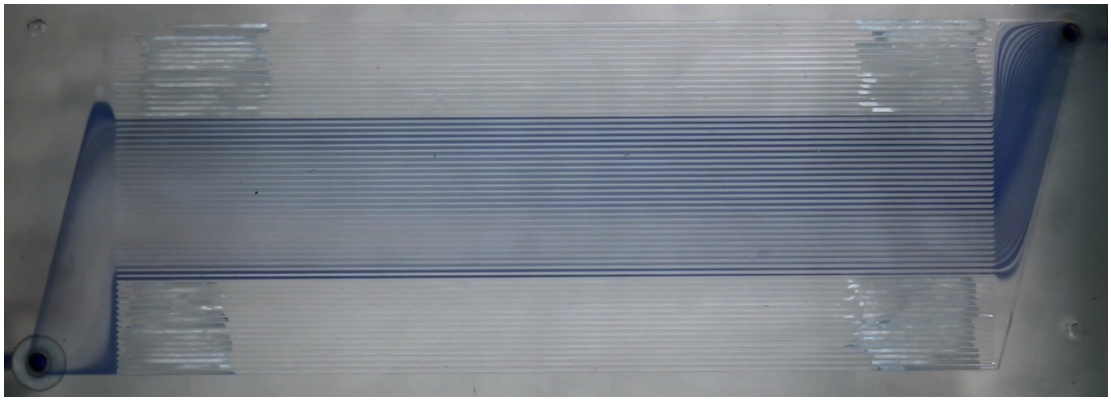

Figure 56. Design 1 Slim-header lamina with 32 blocked channels at 0.768 ml/min as the dye begins to exit. Flow from left to right.

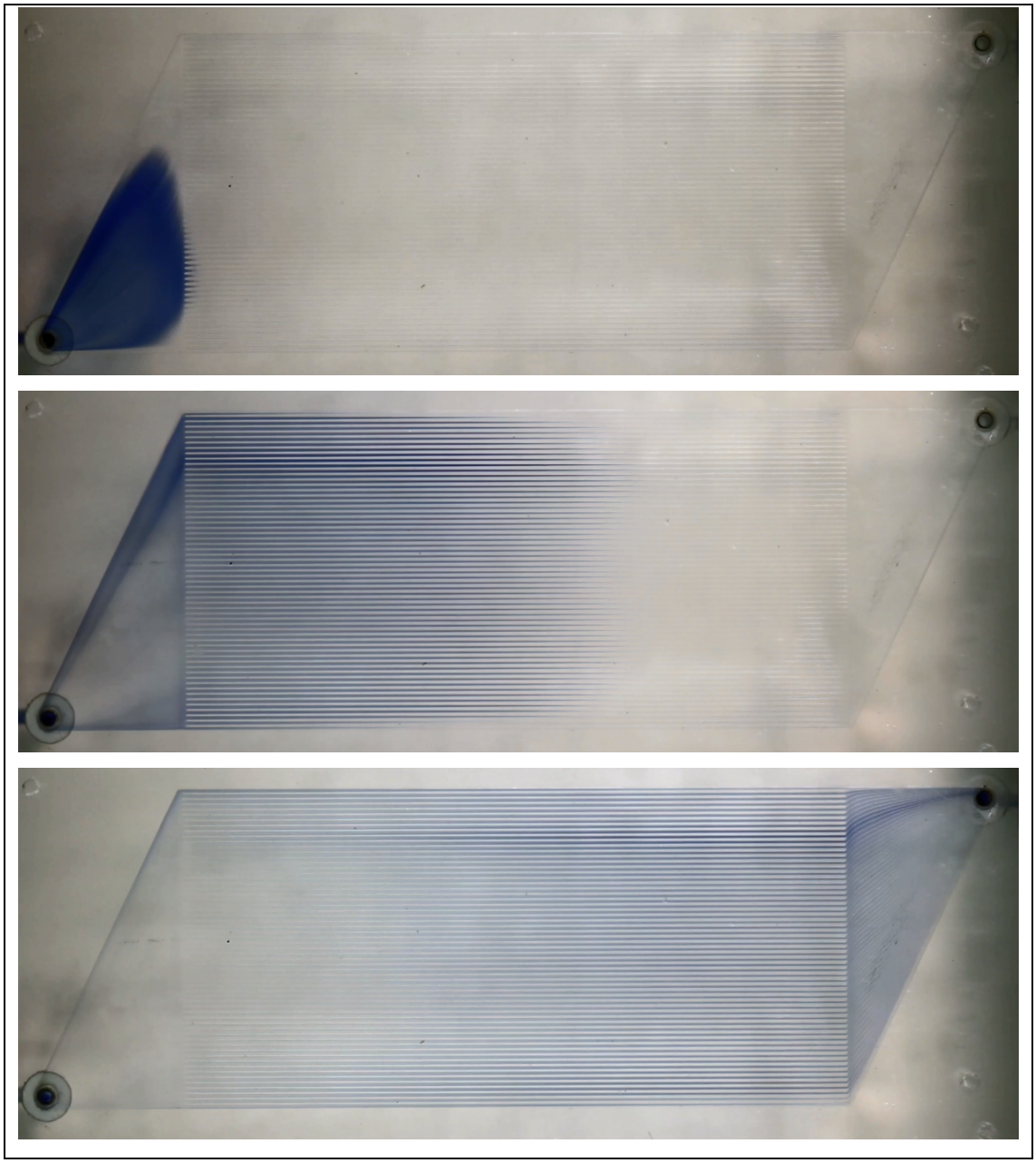

Figure 57. Design 2 Wide-header lamina with no blockage at 0.768 ml/min. (Top) Dye initially entering the lamina. (Middle) Bulk of the dye flowing down the channel array. (Bottom) Dye beginning to exit lamina. Flow from left to right.

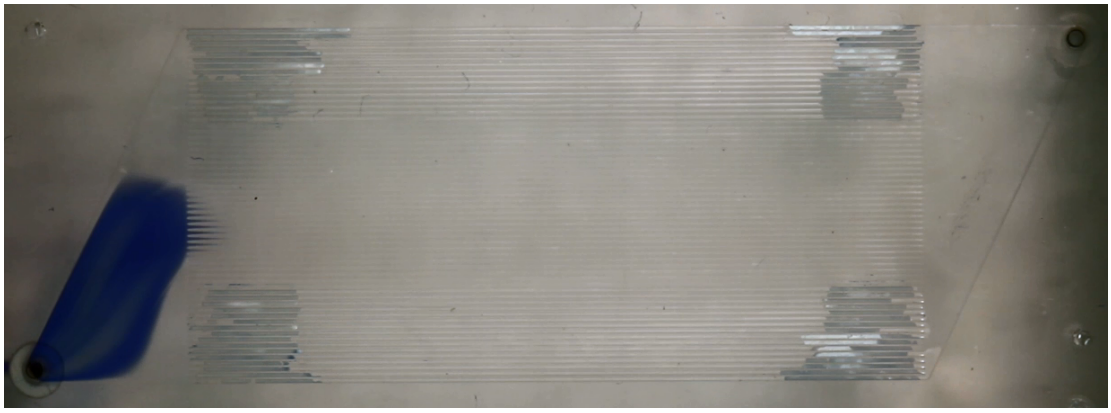

Figure 58. Design 2 Wide-header lamina with 32 blocked channels at 0.768 ml/min as the dye enters the lamina. Flow from left to right.

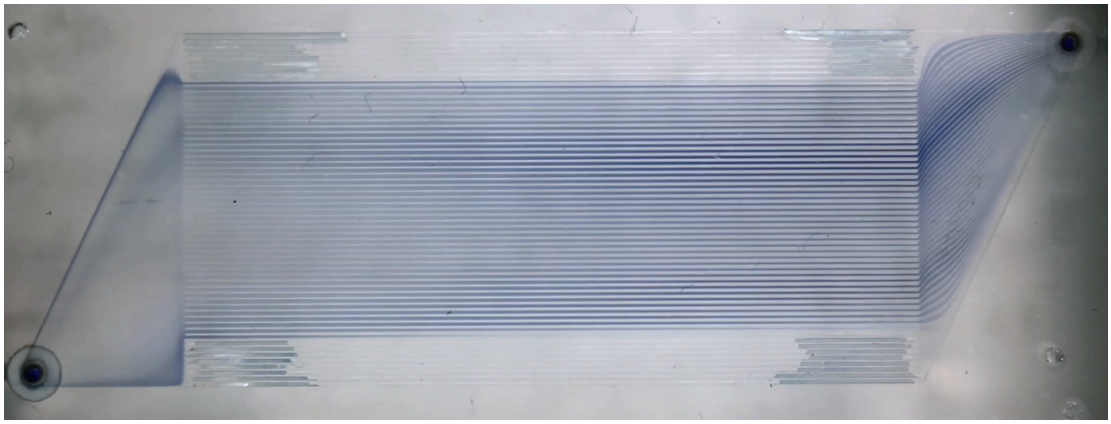

Figure 59. Design 2 Wide-header lamina with 16 blocked channels at 0.768 ml/min as the dye begins to exit. Flow from left to right.

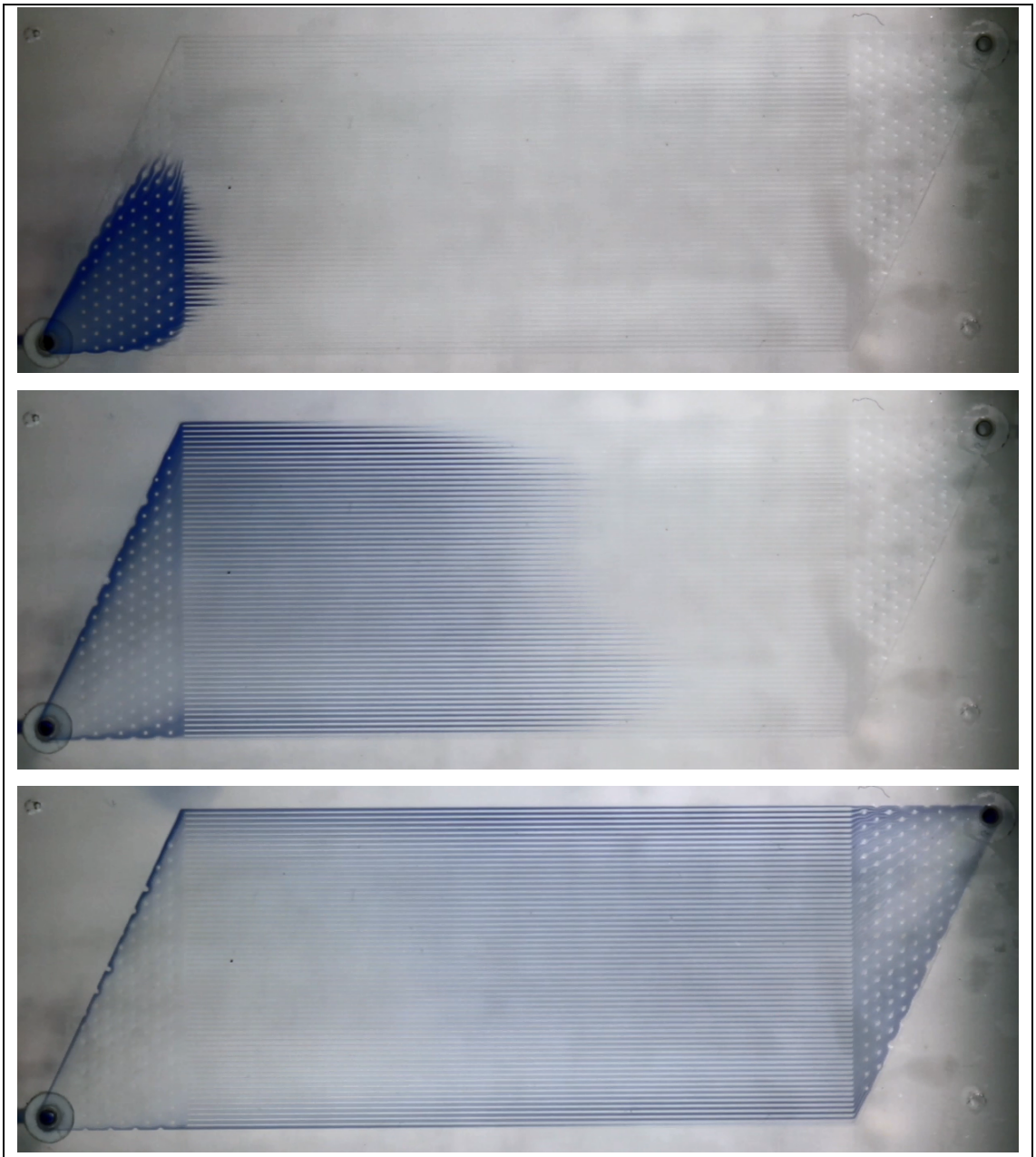

Figure 60. Design 3 Wide-posts lamina with no blockage at 0.768 ml/min. (Top) Dye initially entering the lamina. (Middle) Bulk of the dye flowing down the channel array. (Bottom) Dye exiting the lamina. Flow from left to right.

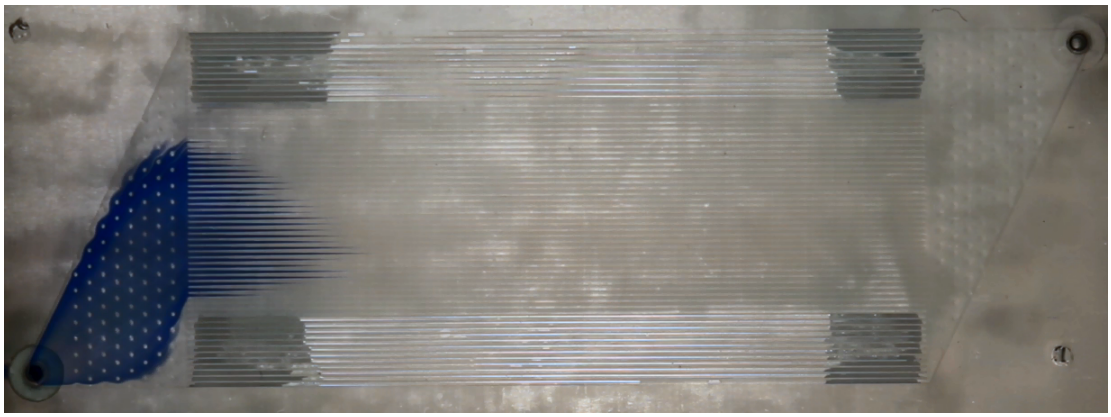

Figure 61. Design 3 Wide-posts lamina with 24 blocked channels at 0.768 ml/min as the dye enters the lamina. Flow from left to right.

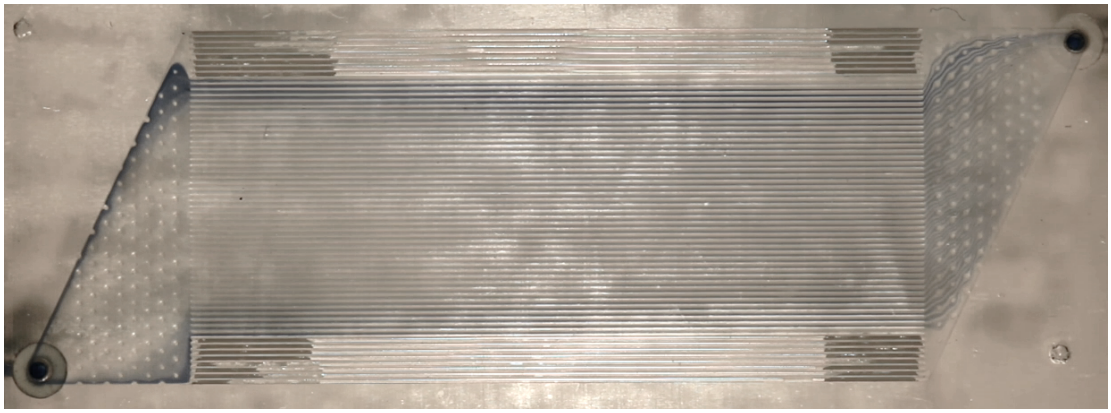

Figure 62. Design 3 Wide-posts lamina with 16 blocked channels at 0.768 ml/min as the dye begins to exit. Flow from left to right.

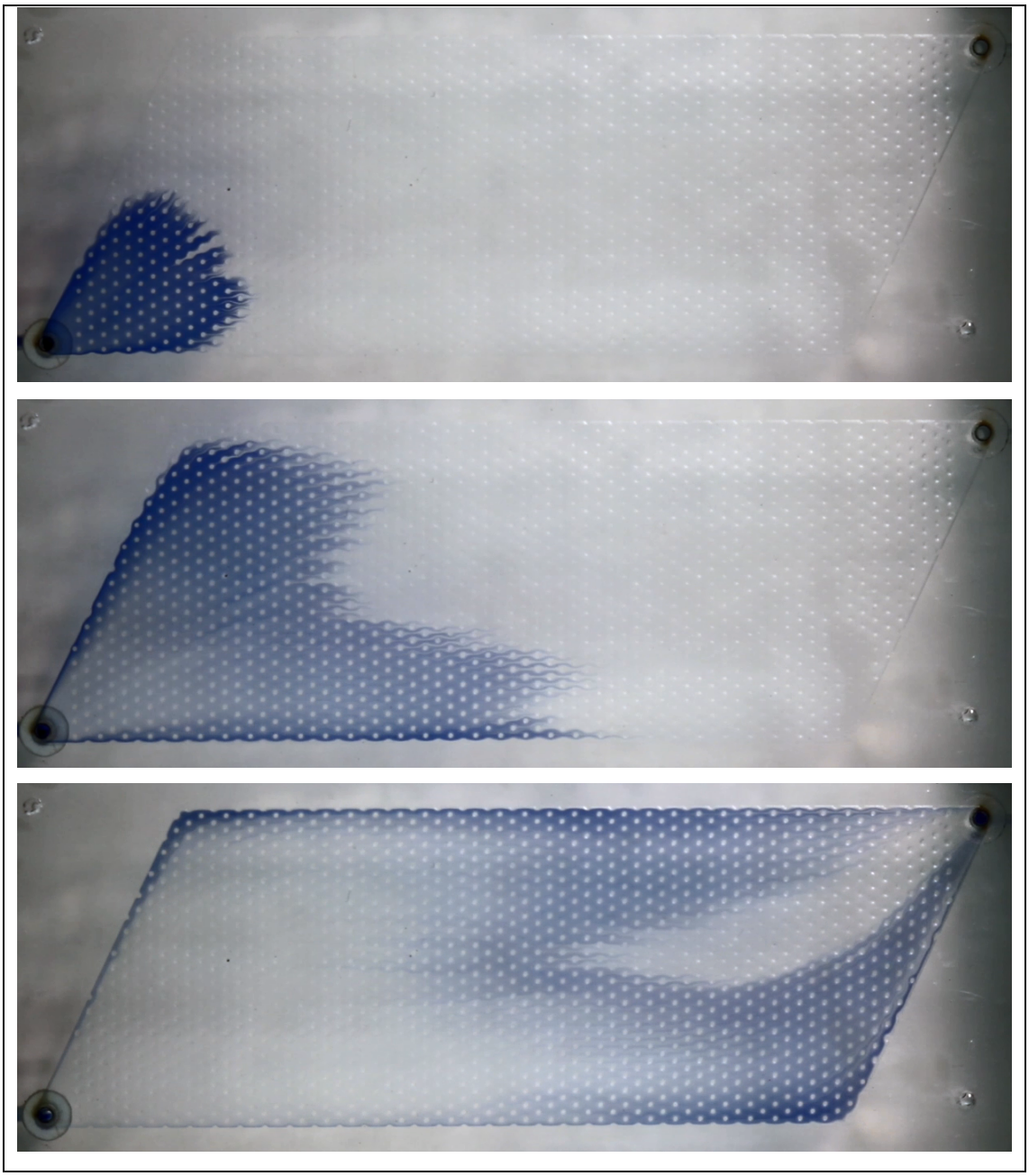

Figure 63. Design 4 All-posts lamina with no blockage at 0.768 ml/min. (Top) Dye initially entering the lamina. (Middle) Bulk of the dye flowing down main portion of micro-post grid. (Bottom) Dye beginning to exit lamina. Flow from left to right.

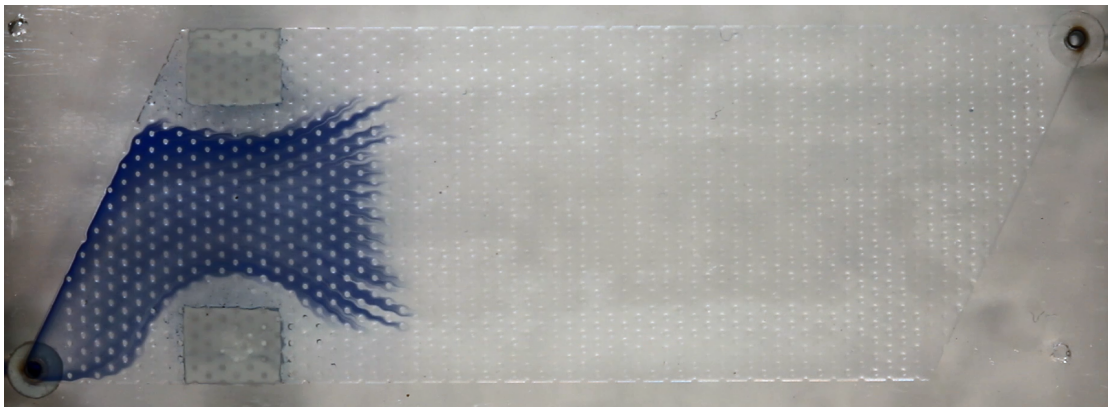

Figure 64. Design 4 All-posts lamina with a simulated 24 blocked channels at 0.768 ml/min as the dye enters the main portion of the micro-post grid. Flow from left to right.

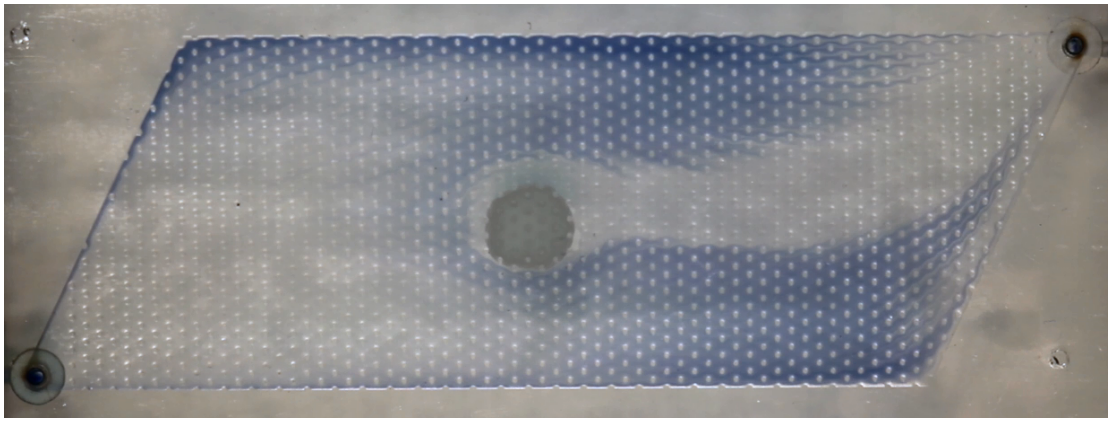

Figure 65. Design 4 All-posts lamina with a center obstruction at 0.768 ml/min as the dye begins to exit. Flow from left to right.

7.4 Pulse Response Measurements

The mass balance between the inlet concentration profile and the outlet concentration profile was closed to approximately 2.5% mass lost at the outlet flow cell. For some measurements, the mass balance was closed to less than 1% mass loss. This is a satisfactory level for continuing with the pulse response study. There was a large amount of variance between measurements due to the alignment of the fiber optic cable heads and the Radel tubing. For example, some measurements showed a mass balance discrepancy of 20-30% but after normalizing the pulse response profiles, their results match up similarly with measurements that showed less than 1%

loss (see Figure 66). This is due to the Radel tubing and fiber optic cable heads not being permanently secured in the flow cell, a design constraint to allow for disassembly and switching parts. As the light path shift across the tubing cross-section, the absorbance path length shifts and that in turn shifts the absorbance profile up or down while still maintaining the same shape. The radial concentration is assumed to be uniform in the flow cell due to the tubing's small diameter and fast dye diffusion times. Uniform radial concentration is an important criterion to meet in the flow cell and was a primary factor in not being able to close the mass balance properly in early iterations of the flow cell design.

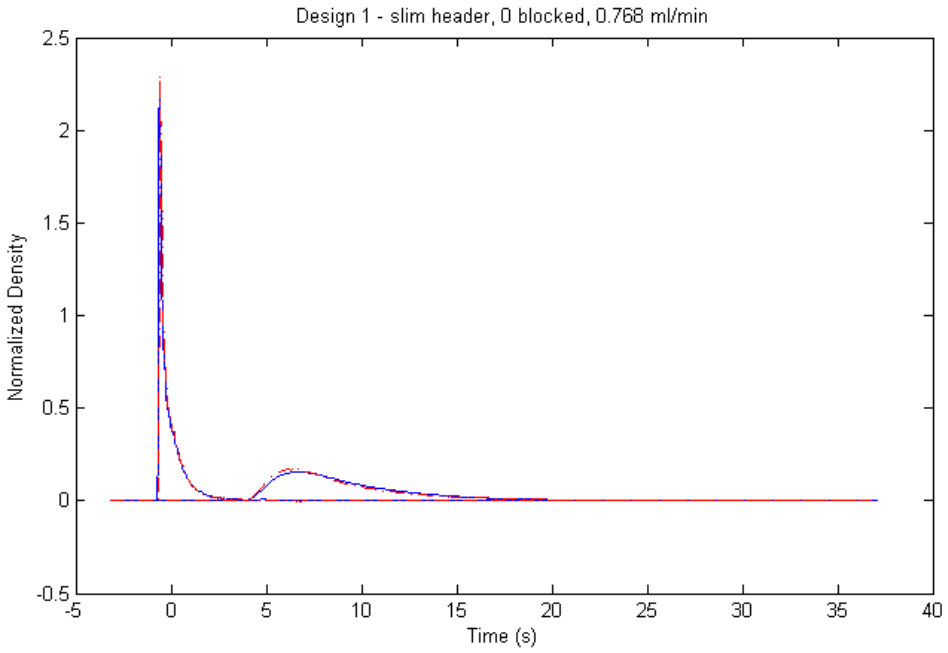

Figure 66. Absorbance profiles for microchannel array at inlet and outlet after tracer injection. 17% mass loss (solid blue line) versus 0.6% mass loss (dashed red line).

The inability to prevent or predict small shifts in the mass balance between the inlet and outlet flow cells prevented a study of leakage conditions where mass is leaves the system. This mass loss could be in the form of improper sealing, which would classify as external leakage, or through a puncture in the dialysis membrane to the opposite lamina channels (e.g. blood crossing to the dialysate compartment), which is classified as internal leakage. Without being able to predict the shifts in mass

balance due to alignment, we would not be able to confidently attribute mass lost at the outlet profile to leakage.

7.5 Measuring Channel Blockage in Devices Using MRT

Two lamina designs were compared to determine the sensitivity of the test loop system for detecting changes in mean residence time 'τ' as a result of defects, specifically, obstructed microchannels.

Each channel blockage condition was compared with a corresponding V/Q predicted value (predicted mean time = fluid volume space / volumetric flow rate). For design 1, with the slim header, the averages of the mean residence times for 0, 4, 8, 16, 24, and 32 blocked channel conditions are shown below. The no blockage condition matches closes with the predicted value and then difference between the two values increases with increasing channel blockage.

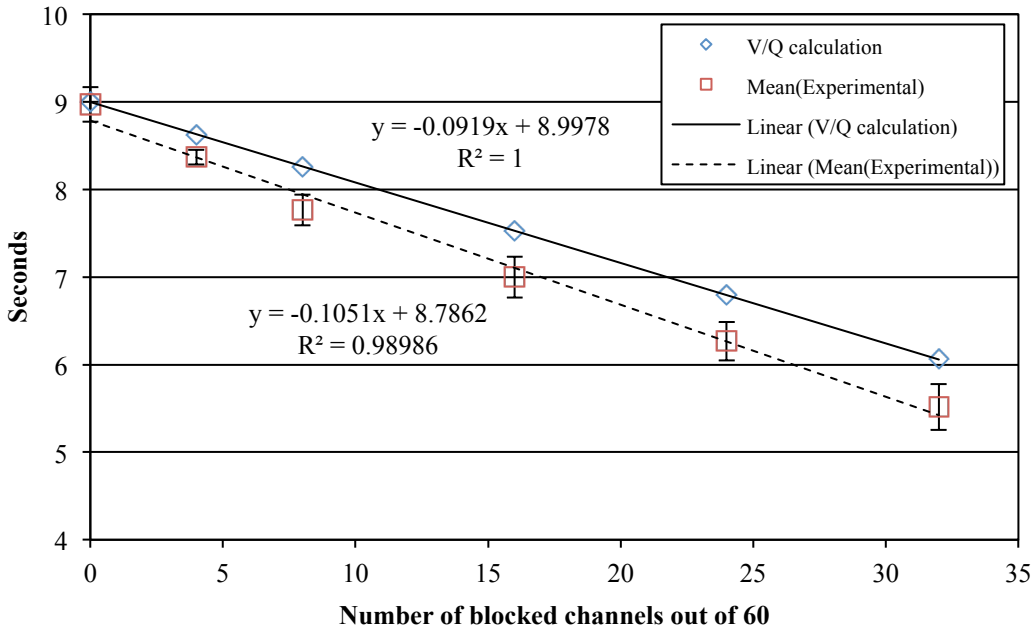

Figure 67. Average mean residence times for design 1 (slim-header) with error bars (1 standard deviation) plotted with V/Q predicted values.

The averages for the mean residence times of the blockage conditions (0, 4, 8, 16, 24, and 32 blocked channels) for lamina design 2 (wide-header) are plotted with

the V/Q predicted values in Figure 68. For the wide header lamina design, measured mean residence times are lower for all conditions, including the zero blocked condition. In addition, the difference between measured and predicted values is more consistent over all cases instead of the wide header design, which increased with increasing channel blockage.

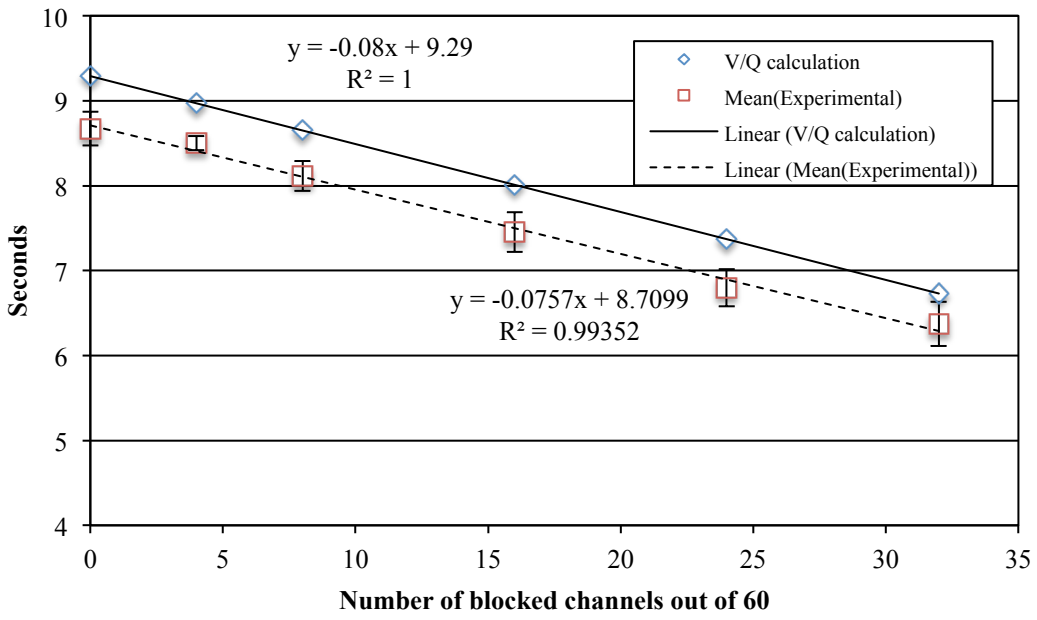

Figure 68. Average mean residence times for design 2 (wide-header) with error bars (1 standard deviation) plotted with V/Q predicted values.

The Student's T-test was used to determine whether the difference between predicted and measured MRT values are significantly different, Ho: mean(V/C – exp. results) = 0. For design 1 (slim-header), the z-score was -10.7, which equates to a probability of $5x10^{-27}$. For design 2 (wide-header), the z-score was -17.7, which equates to a probability of $3x10^{-70}$. This shows that for both designs, the data sets, when taken collectively, are significantly different than predicted values. This may be due to unutilized volume in the system for fluid flow or a variation between calculated volume and that of the experimental system.

The terms of the linear regression lines ($y=b_1x+b_0$) fitted to predicted values and measured values were tested using the Student's T-test with a null hypothesis Ho:

$b_n(V/C) = b_n(\text{exp. result})$. For design 1 (slim-header), the slope terms b_1 had a similarity probability of 0.48 and the y-intercept b_0 had a similarity probability of 0.18. For design 2 (wide-header), the slope terms b_1 had a similarity probability of 0.49 and the y-intercept b_0 had a similarity probability of 0.003. The y-intercepts for design 2 were significantly different ($\alpha = 5\%$) showing that even at the zero blocked condition there is a discrepancy between predicted and measured MRT values. This is in agreement with the findings above.

7.6 Effect of Header Rake and Channel Length on MRT

From the results in Section 7.5, the sensitivity of the test loop for design 1 (slim-header) and design 2 (wide-header) can be calculated using a Welch's T-test. The Welch's T-test is used to check the hypothesis that two populations' means are equal when the variance for both populations is different and unknown. Because each channel blockage condition introduces new flow patterns and potential dead regions, it cannot be assumed that the variance level remains constant over experimental groups. The probability values are plotted in Figure 69 and values are listed in Table 5.

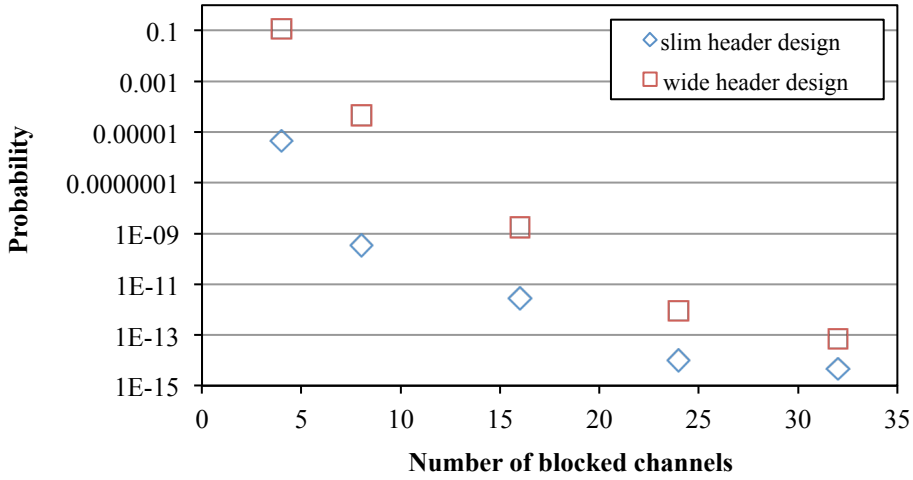

Figure 69. Probability of equal means for mean residence times of zero blocked channels versus various channel blockage conditions for design 1 (slim-header) and design 2 (wide-header).

Table 5 Probability of equal means for mean residence time measurements between no blockage condition and 5 blockage conditions.

Blocked	Design 1	Design 2
4	4.39E-06	0.118
8	3.36E-10	4.53E-05
16	2.72E-12	1.69E-09
24	9.83E-15	8.62E-13
32	4.75E-15	7.09E-14

The pulse response test loop detected a statistically significant difference (α = 0.05) in mean residence time down to 4 blocked channels versus no blocked channels for design 1 (slim-header) and 8 blocked channels versus no blocked channels for design 2 (wide-header). The probabilities show that design 1 (slim-header) reached the predicted sensitivity of the pulse response test loop at 4 blocked channels and could detect potentially fewer blocked channels although that was not tested. Section 4.8.2 discussed predicted sensitivity values. At 4 blocked channels in the slim header design, that equates to 6.7% channels blocked (4 of 60 channels) and 4.1% of the total volume (including extraneous volume of test loop system). The results of Design 2 (wide-header) were short of the predicted sensitivity with 4 blocked channels failing to satisfy the rejection level (0.12 versus α=0.05) but it did show a significant difference in mean residence times at 8 blocked channels. Eight blocked channels for the wide header design equates to 13% of channels blocked and 7.1% of the total volume deactivated in the test loop system. The true level of sensitivity may exist at a level between 4 and 8 blocked channels and without the additional testing could potentially be interpolated from this data although that would require assuming no unique flow behavior arises between the range of 4 and 8 blocked channels.

The difference in sensitivity of detecting changes in mean residence time from channel blockage between the two lamina designs can be partially attributed to the difference in sizes of headers and length of channels. Because design 1 has a slimmer header and as a result longer channels, each channel occupies a larger percentage of

volume in the entire test loop system, leading to a larger change in mean residence time with each blocked channel versus design 2.

The sensitivity for both designs may extend below these measured channel levels if other channels are blocked, e.g. in a more random order instead of the outside most channels. The outside most channels were selected for this study because of the symmetry that will not favor either entrance or exist header and least likely to create separate flow paths through the lamina.

7.7 Effect of Header Support Structures on RTD

Design 3 (wide-posts) was nearly identical to design 2 with the wider header, with the exception of added micro-posts architectural features in the header that would assist in supporting the dialysis membrane in a fully functioning device. Pulse response measurements were recorded for 0, 4, 8, 16, 24, and 32 blocked channels and at the same 0.768 ml/min flow rate as previous tests. The results, along with predicted mean residence times are plotted in Figure 70. Individual measured values are in Appendix C.3. The mean residence times for design 3 are in closer alignment with predicted values in comparison to design 2 (wide-header) which were uniformly lower than predicted values and design 1 (slim-header) which drifted increasingly lower with increasing channel blockage.

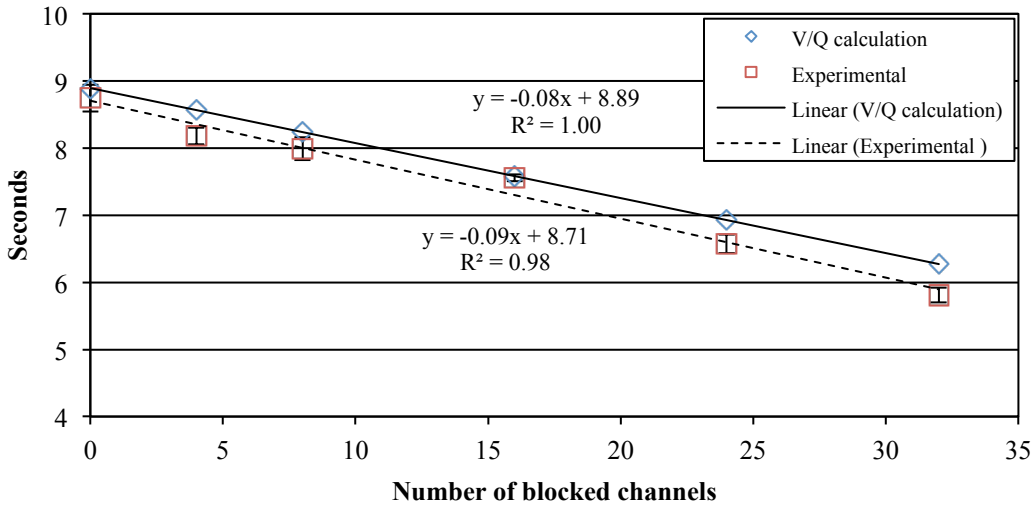

Figure 70. Average mean residence times for design 3 (wide-post) with error bars (1 standard deviation) plotted with V/Q predicted values.

When compared with design 2, design 3 showed a decrease in the difference of the y-intercept of the linear regression from 0.58 to 0.18 seconds, a 69% decrease in error. This may be attributed to the benefit of the micro-posts support the sealing PDMS layer above the header and will be discussed further in section 8.3.

The pulse response test loop sensitivity was also investigated with the wide-post lamina design. The calculated probabilities are plotted in Figure 71 and the values are listed in Table 6. The sensitivity level was similar to design 2 with a failure to detect a significant difference in mean residence time at only the 4 blocked channel condition. The probability values overall for design 3 are higher than for design 1 and 2 because fewer measurements were recorded with design 3 lamina.

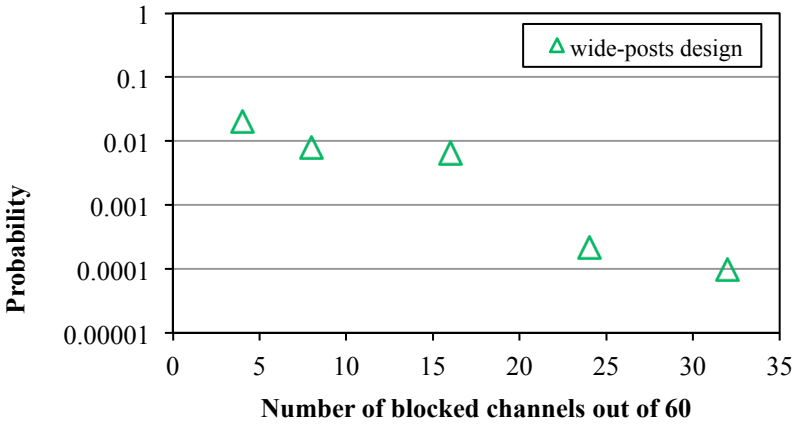

Figure 71. Probability of equal means for mean residence times of zero blocked channels versus various channel blockage conditions for design 3 (wide-posts).

Table 6 Probability of equal means for mean residence time measurements between no blockage condition and 5 blockage conditions.

Blocked	Design 3
4	0.020
8	0.0080
16	0.0065
24	0.00021
32	0.00030

7.8 Residence Time Distributions from Deconvoluted Pulse Response Profiles

Deconvolution was performed on the pulse response profiles to create the residence time distribution of the test loop system which includes microchannels, headers, and extraneous volume leading from and to the absorbance flow cells. Without any post filtering of the data, the resulting residence time distribution profile varied in noise and some groups failed to fully converge on a solution, defined by error being less than 1% between the original output profile and an output profile created by convoluting the original input profile with the residence time distribution.

Figure 72 shows an example of a data set that converged properly (0.6% error) and Figure 73 shows a data set that did not sufficiently converge on a solution (3.1% error).

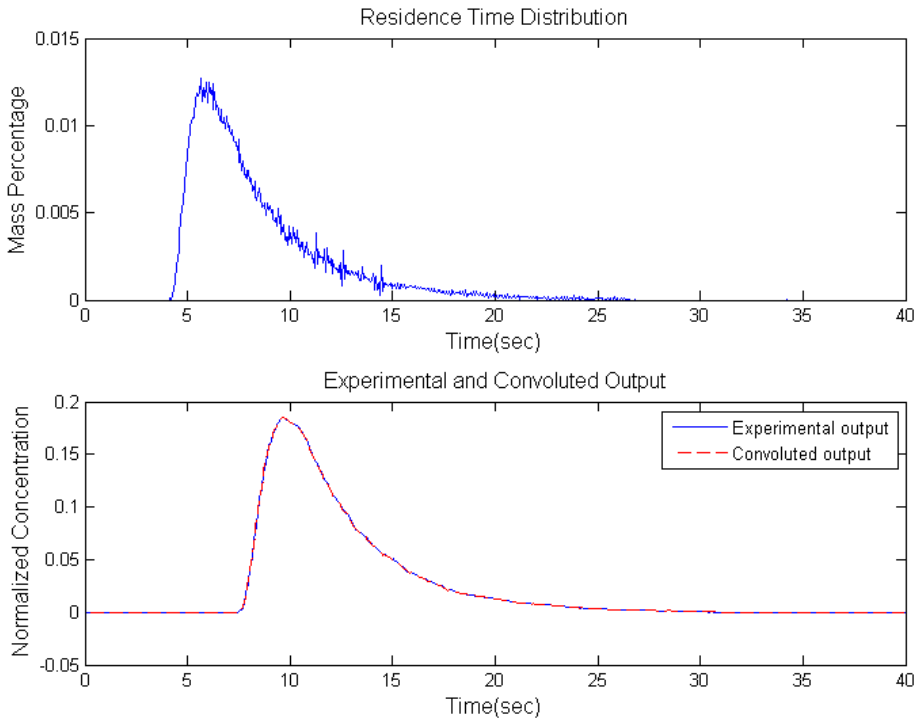

Figure 72. Example of a data set converging on a solution. Conditions: design 1 (slim-header) with 4 blocked channels. (Top) Residence time distribution. (Bottom) Experimental output and reconvoluted output profile.

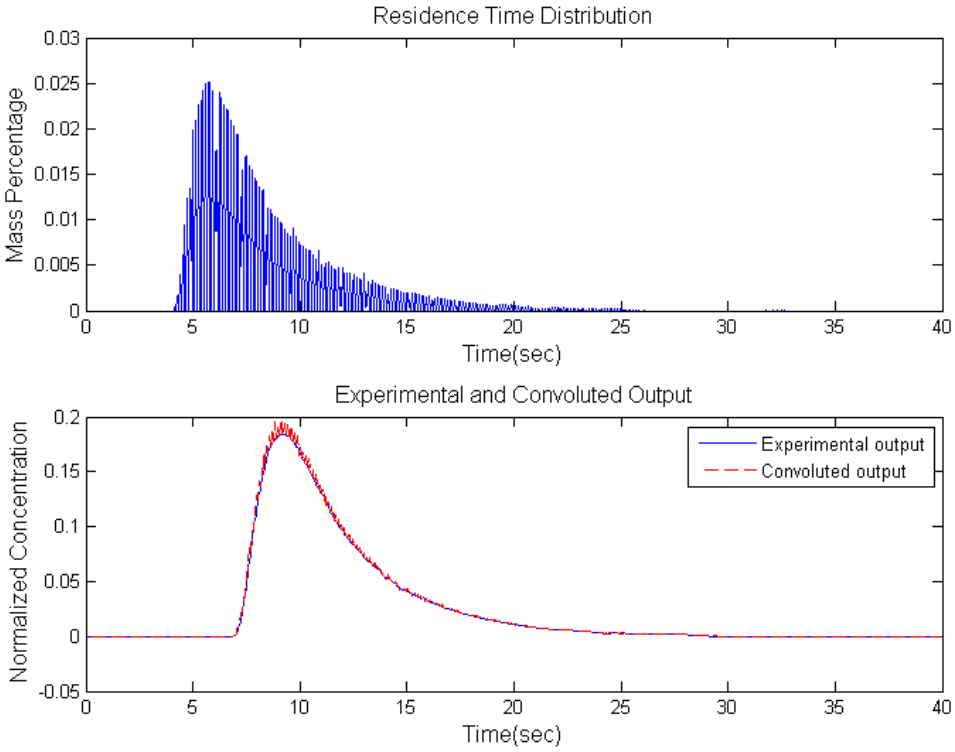

Figure 73. Example of a data set not fully converging on a solution. Conditions: design 1 (slim-header) with 4 blocked channels. (Top) Residence time distribution. (Bottom) Experimental output and reconvoluted output profile.

As discussed in section 5.2, results were passed through a local regression smoothing filter. This filter was chosen instead of a moving average filter that was used on the pulse response profile. The local regression filter was able to filter the high frequency noise in all portions of the RTD profile without removing critical information at the beginning of the curve. The resulting RTD profile showed small increase in error (>1%) of the reconvoluted output profile in some cases and in other cases showed a small decrease in error. For example, Figure 74 show the same data set as Figure 73 after pass through the local regression filter, resulting in a decrease in total output error from 3.1% to 2.8%. The sharp rise at the beginning of the profile was over smoothed with the moving average filter, as a larger averaging span was required to sufficiently remove high frequency noise. Appendix C.6 shows examples of both local regression filter and smoothing filter attempts on identical data sets.

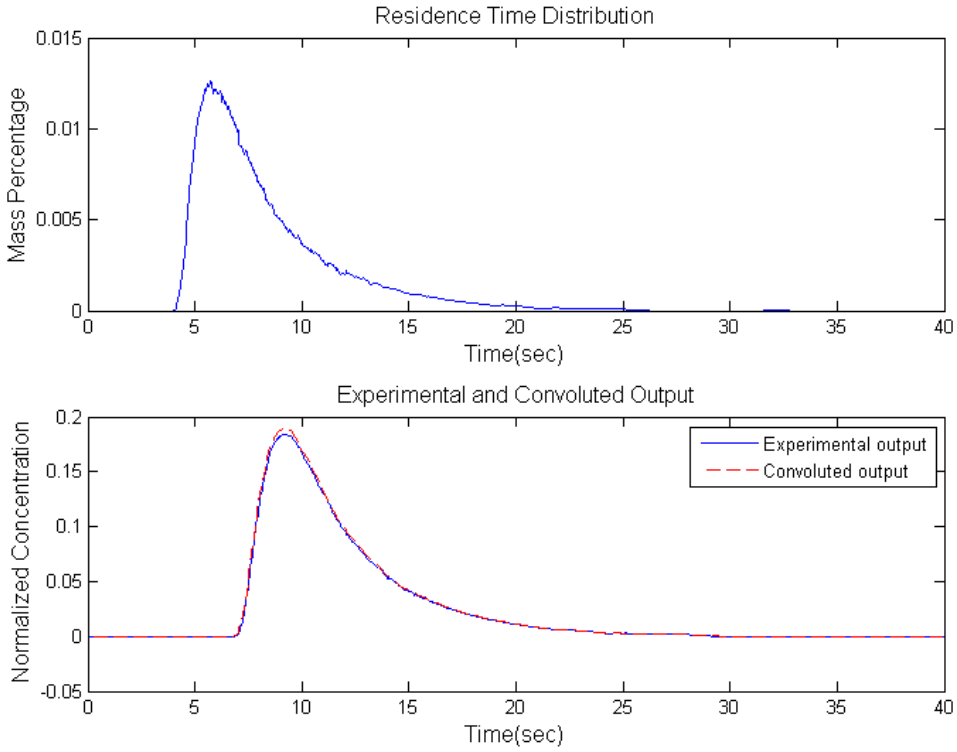

Figure 74. Example of an RTD profile smoothed with a local regression filter. Conditions: design 1 (slim-header) with 4 blocked channels (Identical data set as Figure 73). (Top) Residence time distribution. (Bottom) Experimental output and reconvoluted output profile.

The results following were obtained only from data sets that converged on an RTD solution with equal to or less than 1% total error in the reconvoluted output. Mean residence times were recalculated for the RTD profiles and were in good agreement with the MRTs calculated from the pulse response profiles (~0.1% error).

7.8 Effect of Lamina Design on RTD for Various Defect Scenarios

The four lamina designs were investigated for their robustness at minimizing flow maldistribution though the device in the presence of operation defects (channel blockage). The RTD profiles for design 1 (slim-header) are plotted for the five channel blockage conditions plus the control. The start of the RTD profiles shift predictably from right to left with the increasing of blocked channels. This is an expected outcome as the mean residence time shifts earlier with increasing channel

blockage. This initial signal in the RTD profile is often referred to as the breakthrough time. The breakthrough time is useful in process engineering as it provides the earliest time to expect fluid to exit the system or the least processed material. The peaks of the profiles also increase with increasing blockage, along with a decrease noticeable decrease in the spread of the RTDs. This is examined further by calculating the dimensionless variance of the RTDs.

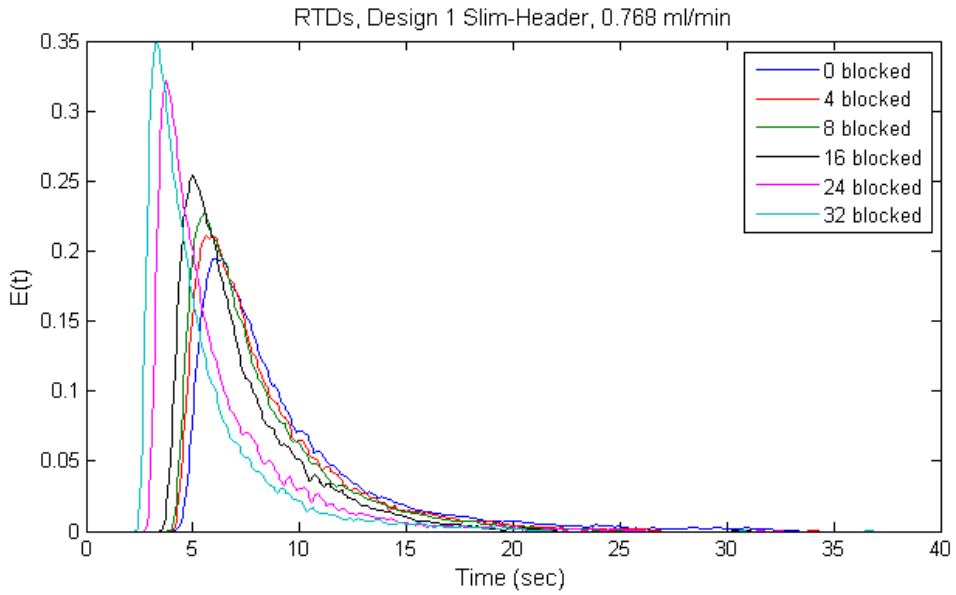

Figure 75. Residence time distributions of design 1 (slim-header) at various channel blockage conditions for flow at 0.768 ml/min.

The residence time distributions for design 2 (wide-header) are plotted in Figure 76 for various channel blockage conditions. Again, a similar trend of the breakthrough time of the distribution profile shifting right to left with increasing number of channels blocked but the additional trend of increasing peak height is noticeable but less consistent. From visual observation only, the amount of spread in the profiles is more similar throughout the conditions when compared to the results for the slim-header lamina.

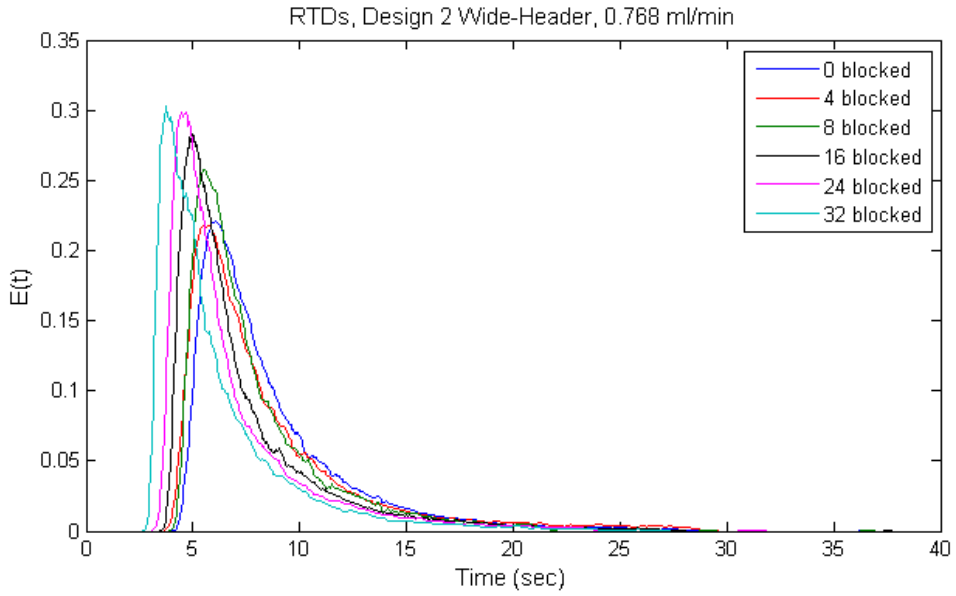

Figure 76. Residence time distributions of design 2 (wide-header) at various channel blockage conditions for flow at 0.768 ml/min.

The RTDs for design 3 (wide-posts) at various channel blockage conditions are plotted in Figure 77. Again similar trends can be observed as with designs 1 and 2. The breakthrough time shifts right to left with increasing channel blockage and the peak of the profiles increase with increasing channel blockage. The changes in profile shape are more visually definable, similar to design 1 result, compared to RTD profiles in design 2 that overlap more.

The RTDs for design 4 (all-posts) lamina design are displayed in Figure 78. A trend in profile with increasing channel blockage is less discernible. There is a rough trend in decreasing breakthrough time and increasing peak height with increasing channel blockage but all of the profiles are more similar in shape and magnitude compared to the other three designs. Design 4 was different from the other laminas in that it did not contain microchannels and instead a grid of micro-posts through the main rectangular portion. Because of this architectural feature difference, blockage was recreated to the equivalent width of an obstruction if microchannels were present and only at the beginning of the main rectangular portion, which is all that is necessary to block an equivalent microchannel.

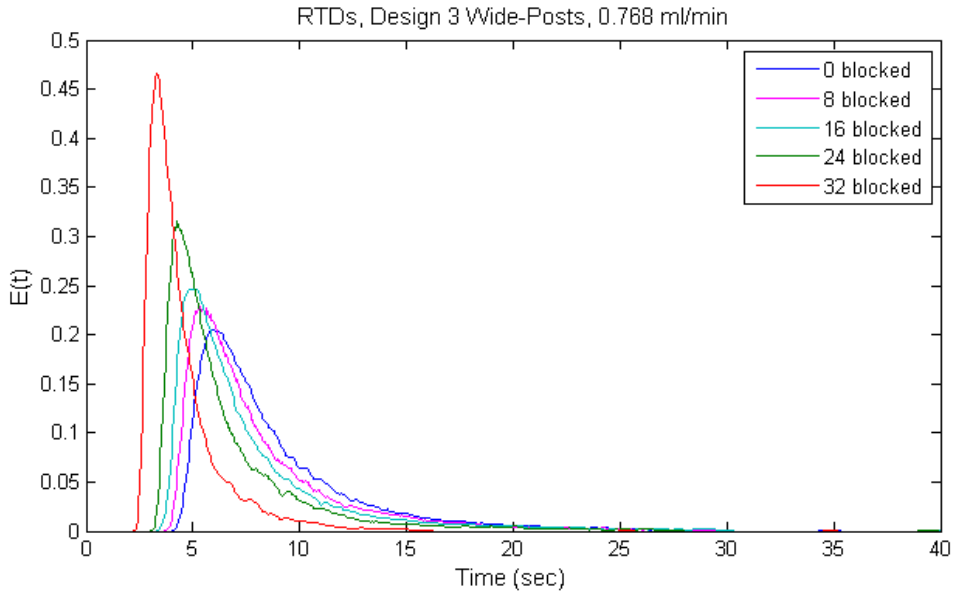

Figure 77. Residence time distributions of design 3 (wide-posts) at various channel blockage conditions for flow at 0.768 ml/min.

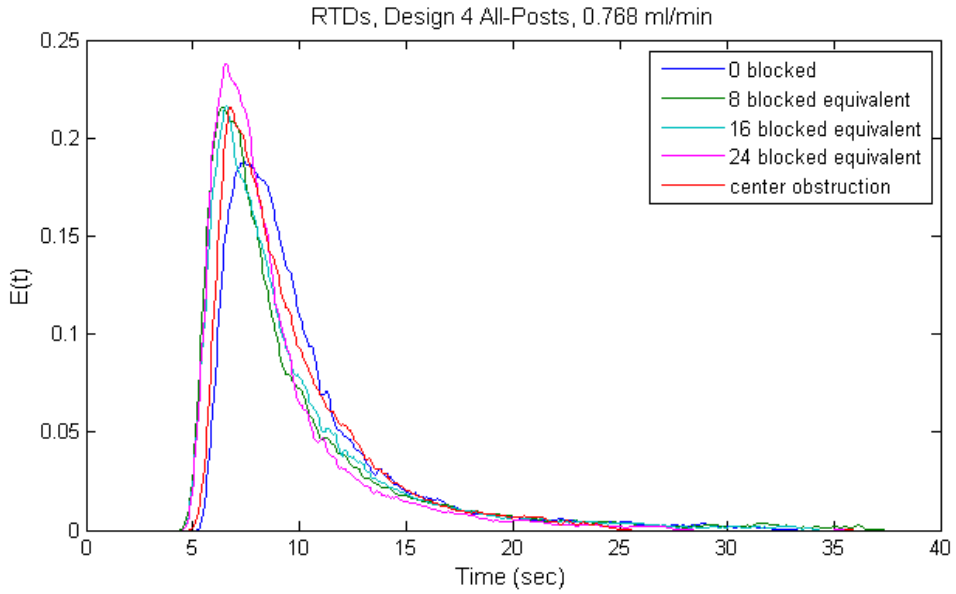

Figure 78. Residence time distributions of design 4 (all-posts) at various channel blockage equivalent conditions and a center obstruction condition for flow at 0.768 ml/min.

The dimensionless variances were calculated from the RTD profiles of each lamina design at the various blockage conditions. The results for all four lamina designs are shown in Figure 79. At the control condition: no blockage, design 2 shows the highest variance and designs 1, 3, and 4 show similar variance levels. As

channel blockage increased, designs 2 and 3 showed higher levels of variance compared to designs 1 and 4. At 24 blocked channels, the variance in design 1 increased dramatically to the level of design 2. And by 32 blocked channels, designs 1, 2, and 3 were at similarly higher levels (design 4 was not measured at a 32 blocked channels equivalent)

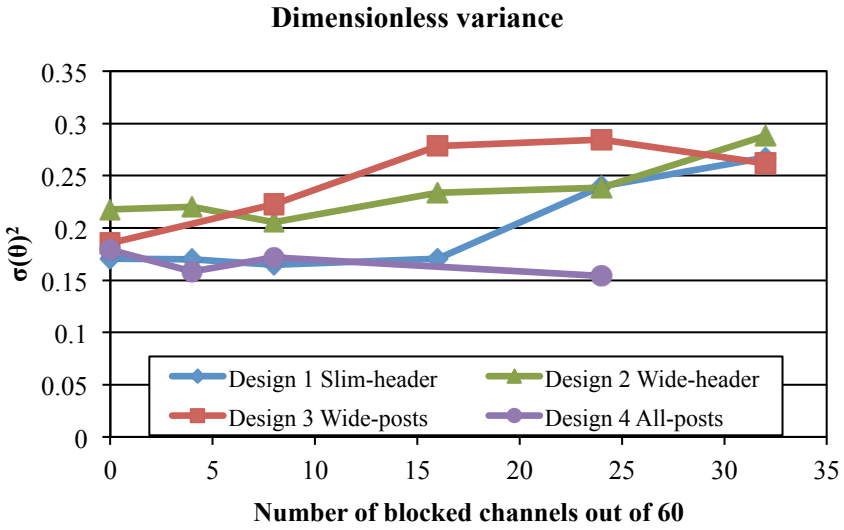

Figure 79. Comparison of the dimensionless variance of the RTDs for the four lamina designs at various blockage conditions.

The skewness of the RTD profiles was also calculated and is compared in Figure 80. Skewness is a measurement in the level of symmetry in a distribution. Symmetrical distributions have a skewness of zero. All RTD profiles showed a positive skewness, representative of the right-sided long tail. In a fully functioning hemodialyzer, we would aim to reduce positive skewness. The long right-sided tail would represent fluid remaining in the device much longer than the mean residence time. This could be a result of stagnant fluid and, in the application of blood, could potentially lead to cell damage. The results show that designs 2 (wide-header) and 4 (all-posts) had the highest skewness at the no blockage, control condition. Design 3 (wide-posts) showed the highest skewness overall at the 24 blocked channels condition. Design 1 (slim-posts) showed the lowest skewness for the lower blockage

condtions (4 to 16). Overall though, the relative change in skewness is smaller compared to changes in variance.

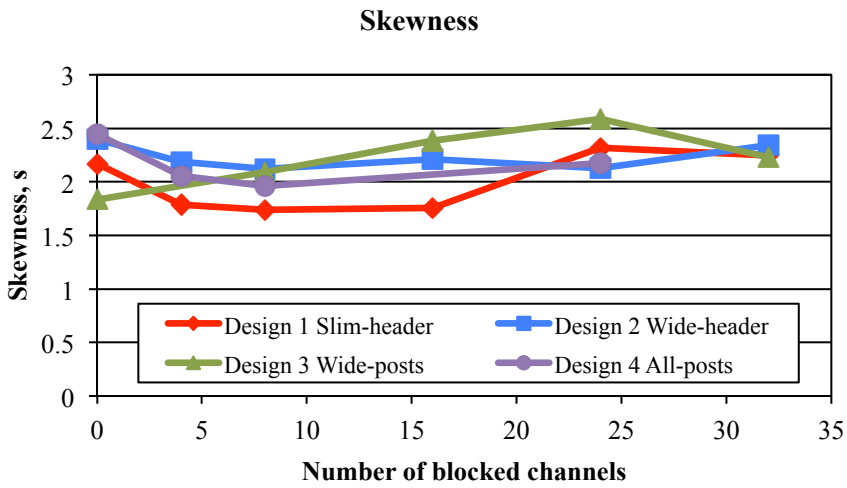

Figure 80. Comparison of skewness of the RTDs for the four lamina designs at various blockage conditions.

7.9 CFD Simulation of Pulse Response Tracer

A pulse response simulation was performed for the design 1 slim-header lamina at no channel blockage, design 1 slim-header lamina at 16 blocked channels, design 2 wide-header lamina at no blockage, and design 4 all-posts lamina at no blockage. Below are sets of concentration distributions for simulated tracer as it flows through the lamina portion of the segmented model. Figure 81 shows the simulated tracer flowing through the design 1 slim-header lamina at early, middle, and late stages. When visually compared with tracer behavior in the experimental device (see Figure 54), the simulation showed slightly more uniform introduction of the tracer into the entrance header of the lamina. Similarity increased between the experiment and model as the tracer moved down the channel and out of the lamina.

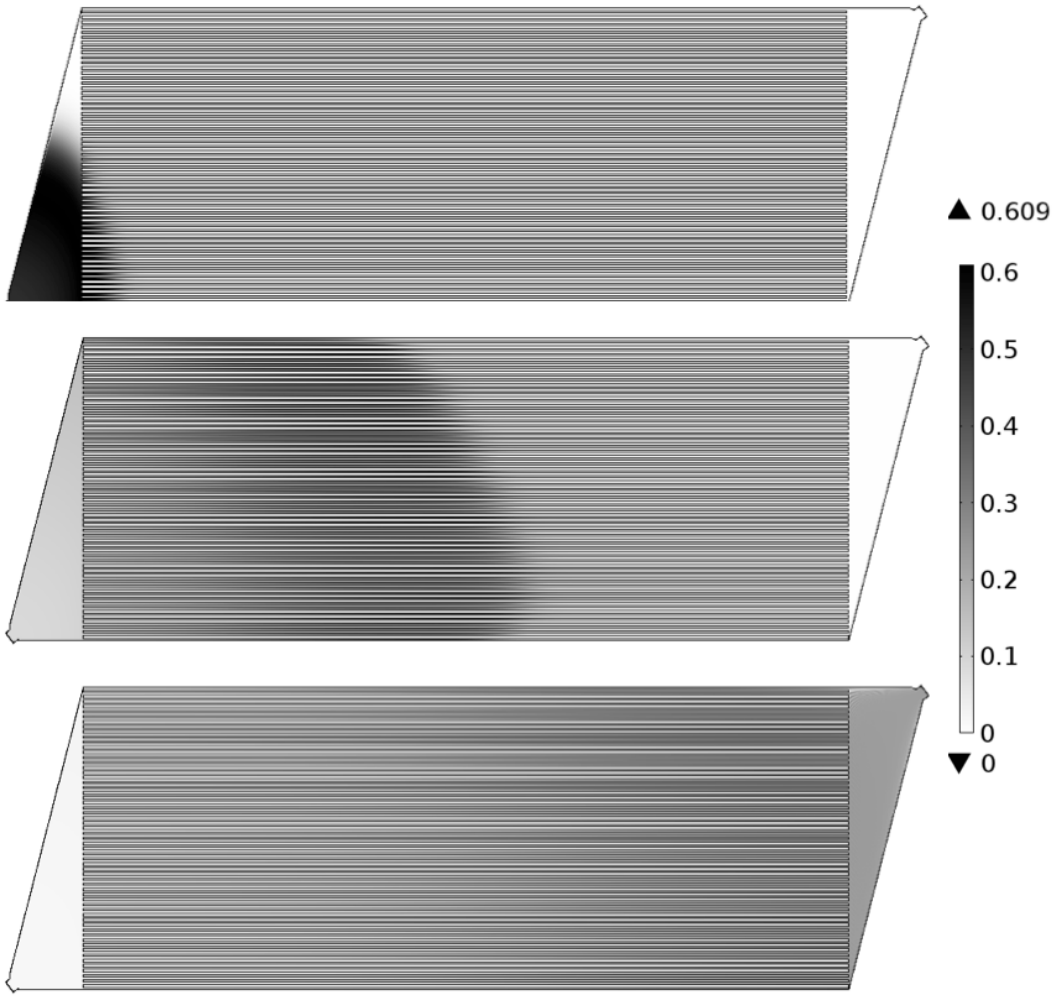

Figure 81. Concentration distribution of the tracer in the pulse response simulation for design 1 slim-header lamina for: (Top) tracer initially entering lamina, (Middle) bulk of tracer moving down channels, and (Bottom) tracer exiting the lamina. Flow from left to right. ***Image courtesy of Agnieszka Truszkowska***

The concentration distributions of the tracer in simulation of design 4 all-posts lamina are shown below in Figure 82. Compared to tracer images collected from experiment (see Figure 63), the simulation has a more evenly distributed flow through the lamina. Both experimental and simulated tracers enter the lamina more evenly distributed, although simulations show the tracer moving more quickly along the edges of the geometry. They begin to differ significantly in the main portion of the lamina when the experimental tracer segments into a top and bottom major flow path. The tracer flow pattern in simulation is more aligned with the expectation that the

tracer should have an overall profile similar to flow through the same lamina shape but lacking micro-posts. Both simulation and experiment show a pattern of local streamlining of the tracer around each micro-posts.

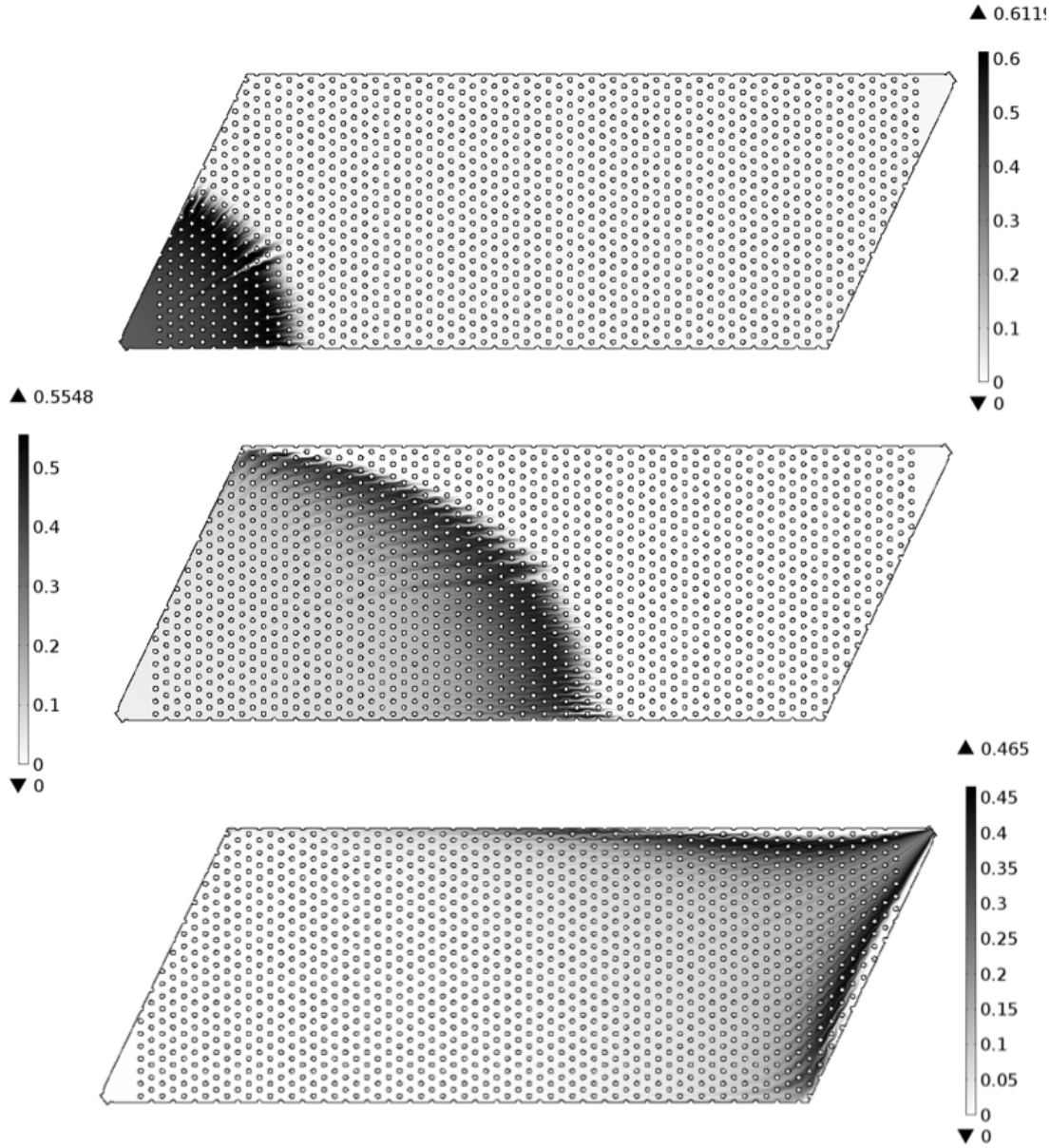

Figure 82. Concentration distribution of the tracer in the pulse response simulation for design 4 all-posts lamina for: (Top) tracer initially entering lamina, (Middle) bulk of tracer flowing through main portion, and (Bottom) tracer exiting the lamina. Flow from left to right. *Image courtesy of Agnieszka Truszkowska*

A simulation was performed for the design 1 (slim-header) lamina with 16 blocked channels for comparison with experiment. The presence of the deactivated channels in both simulation and experiment create dramatic changes in volume geometry that are reflected in the flow path of the tracer. For example, in Figure 83, we can see that as tracer exits the channel array in both cases, the flow wraps around to fill the top portion of the exit header and slowly creeps towards the isolated bottom corner of the header. It is also observed that tracer lingers at the slower edges of the entrance header although more predominantly in the experiment. And the tracer flow followed a less parabolic pattern through the microchannel array when compared to experiment.

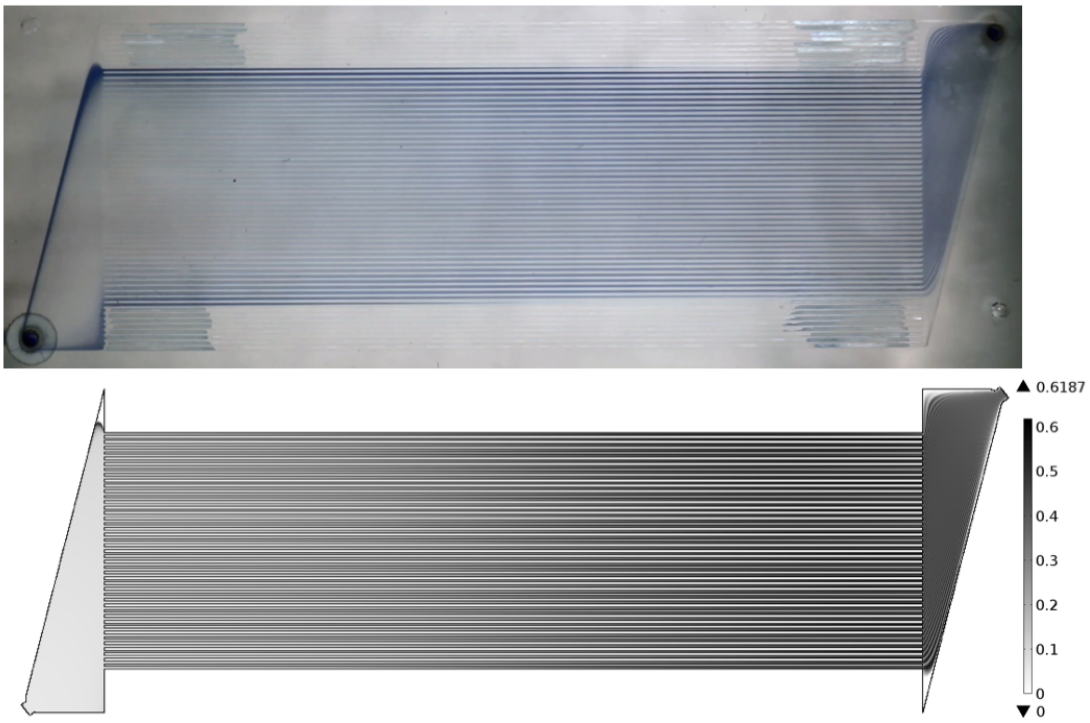

Figure 83. Design 1 slim-header lamina with 16 blocked channels: (Top) Tracer flow path in experiment and (Bottom) Concentration distribution of the tracer in the pulse response simulation. Flow from left to right. ***Image courtesy of Agnieszka Truszkowska***

The mass balance for each model segment and for the entire model system were maintained close to equal for the respective inlet and outlets. Closing the mass balance for each model segment is important but if the model is allowed a sufficient

grid size, time resolution and time span for solutions, it should for the most part close sufficiently. There may arise some issues with the tracer not leaving the system, but again, these should cause only smaller shifts in mass balance in a properly developed model. The more critical concern was moving between model segments as this step required approximations and assumptions, stated in Section 6.2, that are partially validated by closure of the mass balance across the whole model system.

Table 7 Mass balance error for each model segment and the entire model system for the various simulation conditions.

Design and Condition	Component	Abs relative error, %	Whole system error, %
1 Slim-header No blockage	Inlet tubing	0.30	1.90
	Test article	0.01	
	Outlet tubing	0.08	
1 Slim-header 16 blocked channels	Inlet tubing	1.55	0.052
	Test article	0.0052	
	Outlet tubing	0.76	
2 Wide-header No blockage	Inlet tubing	0.32	1.33
	Test article	0.042	
	Outlet tubing	0.078	
4 All-posts No blockage	Inlet tubing	1.58	3.41
	Test article	0.01	
	Outlet tubing	0.075	

The output profile of the pulse response measurement from CFD simulations and the pulse response test loop showed similar shape and peak magnitude for the three designs/conditions investigated (see Figure 84, Figure 85, and Figure 86). In all simulations, the mean residence times were longer than the overall average MRT values calculated for that condition (average mean residence time) but also for the predicted V/Q calculated values. The mean residence time was calculated from the numerical simulation results using the same method as in experiments.

Table 8 lists the mean residence times for experiments and simulations and lists the relative error between the two values. All simulation MRTs were longer than

experimental MRTs. The smallest difference occurred at 9.9% for the design 1 slim-header lamina with no blocked channels. The largest difference occurred at 32.1% for the design 4 all-posts lamina with no blockage.

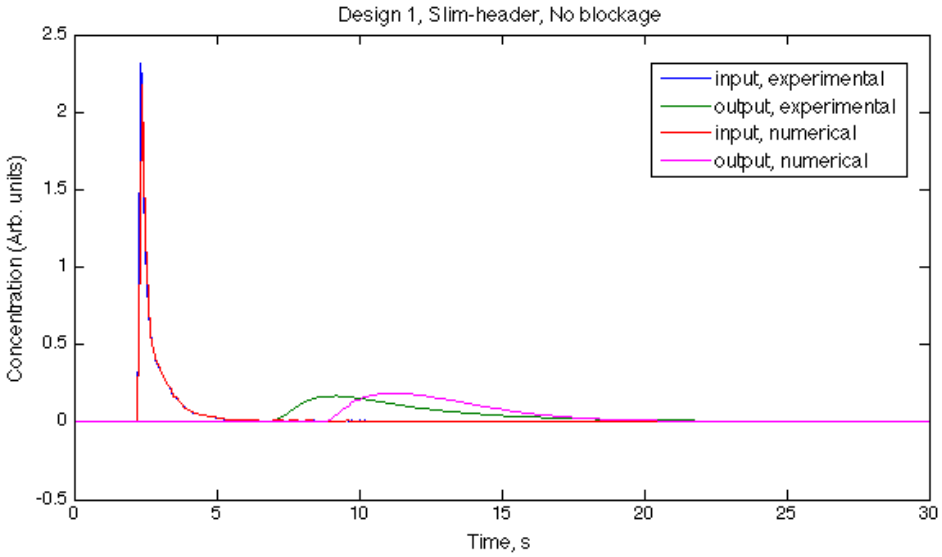

Figure 84. Input and output profiles for experimental and numerical pulse response of Design 1 Slim-header lamina at zero blocked channels.

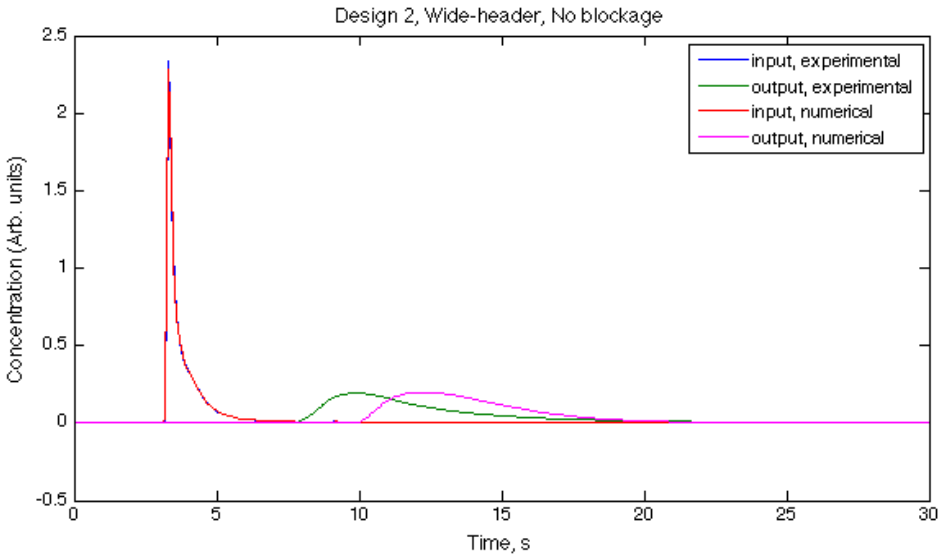

Figure 85. Input and output profiles for experimental and numerical pulse response of Design 2 Wide-header lamina at zero blocked channels.

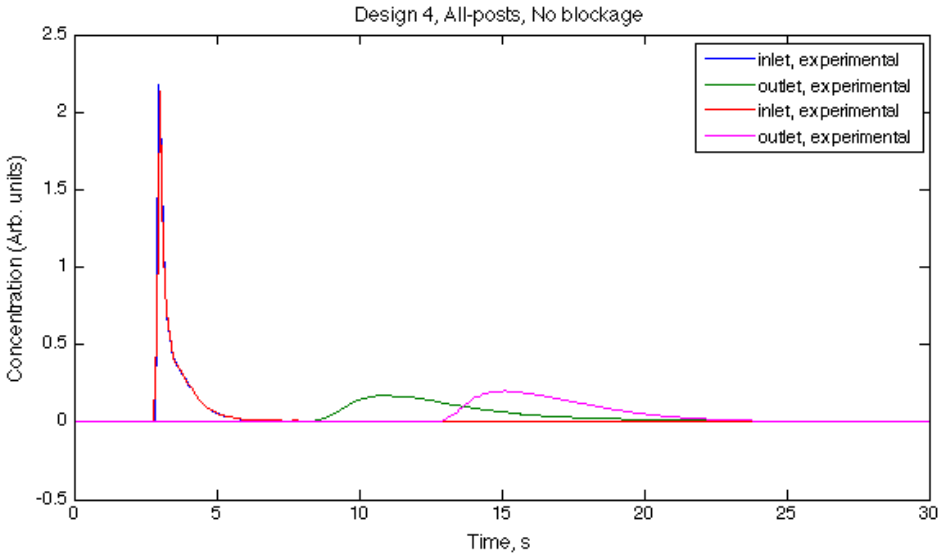

Figure 86. Input and output profiles for experimental and numerical pulse response of Design 4 All-posts lamina with no blockage.

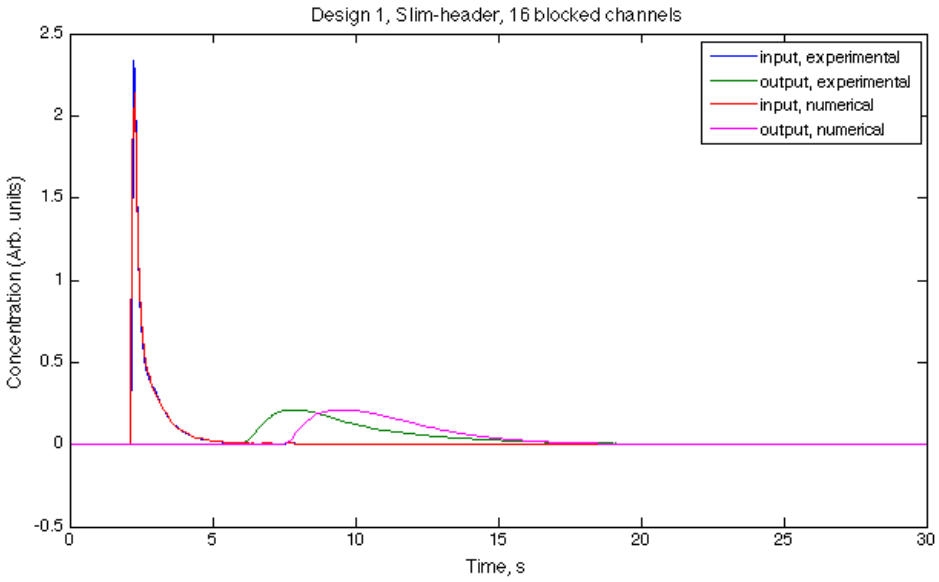

Figure 87. Input and output profiles for experimental and numerical pulse response of Design 1 Slim-header lamina with 16 blocked channels.

Table 8 Experimental and numerical mean residence times for various conditions.

Design and Condition	Experimental MRT, s	Numerical MRT, s	Relative Error, %
Design 1, slim-header, no blockage	8.97	9.86	9.92
Design 1, slim-header, 16 blocked channels	7.22	8.36	15.79
Design 2, wide-header, no blockage	8.67	9.93	14.53
Design 4, all-posts, no blockage	10.06	13.29	32.11

8 DISCUSSION

8.1 Effect of PEO Coating on Bubble Blockage in Microchannel Arrays

The effects of the PEO coating influence on bubble flow at lower Reynolds numbers and its negligible influence at higher Re were recreated in numerical simulations. However, the numerical simulations were restricted to a single channel in which bubbles were always mobile. In our experimental effort with the multichannel array, bubble mobility could be substantially reduced and stopped due to the flow redistribution among channels. Thus, comparison between experimental data shown and simulation results could be only qualitative and in trends. Nonetheless, the magnitude of the bubble velocity within coated and uncoated channel models and the existence of the liquid film between bubble and microchannel walls are quite indicative of the likelihood of channel blockage at various pressure fields. A region of low bubble mobility is defined by simulation results showing a reduction in bubble velocity in the hydrophobic model versus the hydrophilic model and high bubble mobility is defined by simulation results showing negligible difference in bubble velocity between the two conditions. These regions are overlaid with experimental results by relating simulated bubble velocity (similar to liquid velocity) with average nominal velocity from experiments (see Figure 88).

The low bubble mobility region, defined by both experimental and numerical simulation results, is the effective region at which the PEO coating can reduce channel obstruction by bubbles. Beyond this region, the pressure field is sufficient to similarly overcome forces resisting bubble movement in both PEO-coated and uncoated conditions, negating the utility aspect of the coating. This work serves as a proof of concept for the application of a PEO-PB-PEO coating for reducing bubble blockage at Reynolds numbers defining the low bubble mobility region. However, different microscale-based geometries/architectures could alter the pressure distribution through the headers and microchannel arrays and consequently the region of coating effectiveness may shift.

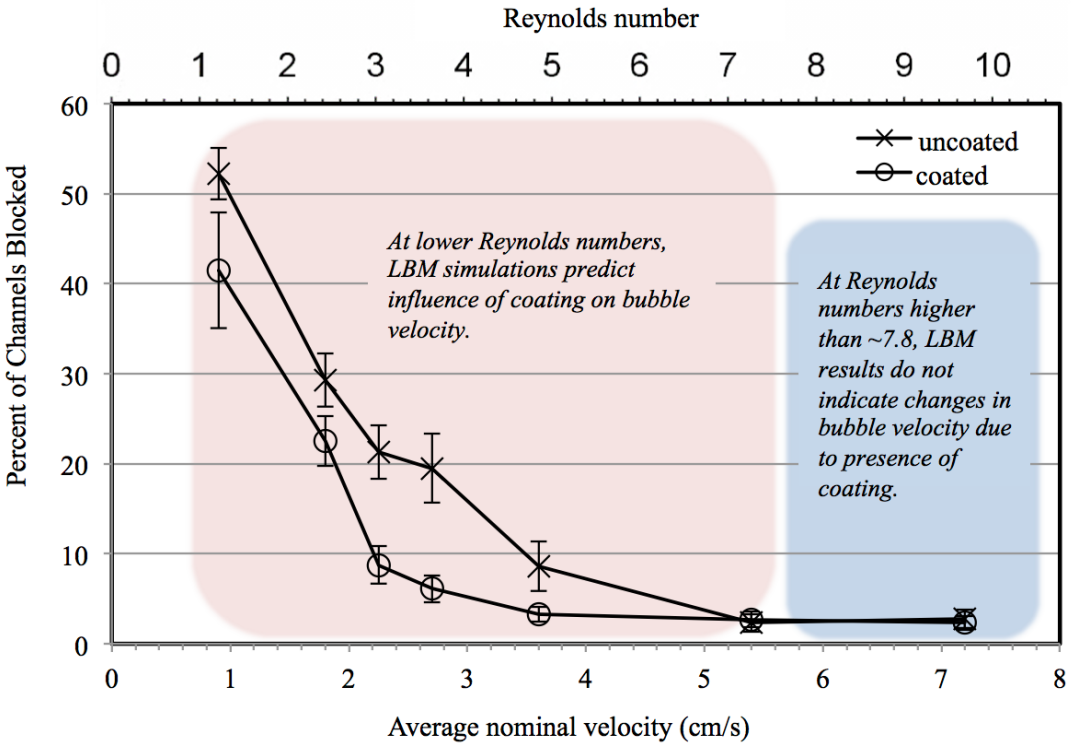

Figure 88. Qualitative results from LBM numerical simulations overlaid experimental data from Figure 51 indicating Reynolds number regions of PEO effectiveness on bubble mobility

The findings in this work are in good alignment with the existing body of knowledge regarding surface interactions in microfluidic flow [23], [24], [26]–[28], [33]. The thin liquid film between the bubble and channel wall plays a significant role in improving bubble mobility. The coating masks the surface electrostatic charge and surface heterogeneities, and reduces the contact angles [73]. The reduction in contact angle by the PEO-PB-PEO coating results in decreased dewetting velocity of the liquid thin film as well as the critical bubble velocity at which a thin film is maintained or formed, allowing the lubricated bubble to move at lower velocities [73]. On a heterogeneous surface, such as machined polycarbonate, advancing and receding contact lines successfully define the arresting forces acting on a stationary bubble in a pressure field [78]. Both advancing and receding contact angles were shown to be reduced in the presence of the PEO-coating [73]. Overcoming pinning forces is observed over the period allotted for the system to stabilize when stationary bubbles release and move down the channel. In addition to the effect on the air-water

interaction, the PEO-coating creates a stationary hydration barrier that is energetically similar to water [79]. This in turn decreases the slip length at the microchannel wall (where slip may otherwise occur) and increases pressure drop across the system, which also assists in bubble movement. Various phenomena responsible for improved bubble mobility have been listed. Further investigation is required to determine which phenomena dominate.

The cessation of bubble movement in straight microchannels occurs when the pressure drop along the length of the bubble cannot overcome the contact line forces. Contact line forces can resist the force that the pressure field applies on the bubble up to a certain limit and makes a bubble stationary. A more complete discussion of the pinning and capillary forces can be found in Mohammadi (2014).[73] The PEO brush coating masks the surface electrostatic charge and surface heterogeneities to some extent, and more importantly reduces the contact angles. The difference between the cosines of contact angles in the coated system is significantly less than ones in the uncoated system. Subsequently, in the coated system the minimum force provided by the pressure field required to overcome the pinning forces and keep the bubbles moving is lower, leading to the coated system having reduced bubble retention.

It can be observed from Figure 50 that a large number of bubbles are present in the exit manifold region. While important, it should be noted that our objective was to focus specifically on the microchannel array and therefore a straightforward, simple design was chosen for the manifolds.

Only the number of obstructed channels was recorded in these measurements but another valuable measurement is the length of the bubbles obstructing the microchannels. It was observed that at lowest mean channel blockage (< 2 channels), the size of bubbles remaining in the system tended to be smaller than at higher mean channel blockage values. In Figure 89, observed bubbles in microchannels are shorter unlike longer ‘noodle-like’ bubbles that occupy a significant portion of a single microchannel. Small bubbles, which do not experience a large pressure difference between their front and back interfaces, are more prone to becoming stationary when the thin film around them dries out. This finding is in agreement with our experimental observations.

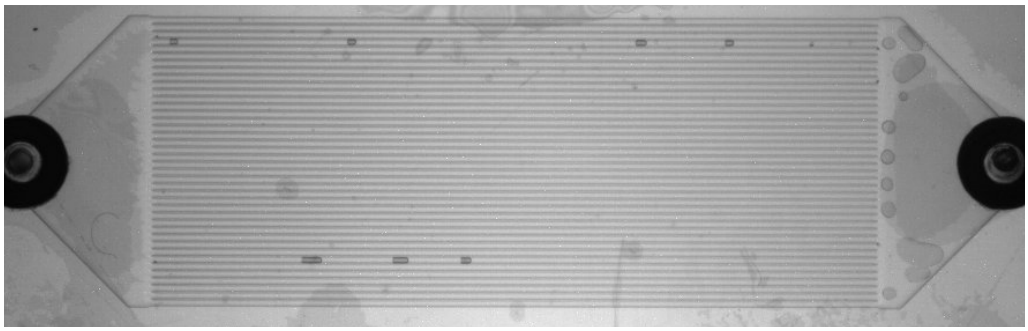

Figure 89. Coated channels obstructed by small bubbles after allowing systems to stabilize, at 2.0 ml/min flow rate or 3.6 cm/s average channel velocity. Fluid flow from left to right

The mechanisms responsible for the interaction between bubbles and PEO coated polycarbonate surface are more complex than a smooth and homogeneous hydrophilic or hydrophobic surface, as discussed in the introduction. As an initial attempt at implementing the Lattice Boltzmann modeling method for our system, only contact angle was represented as a surface characteristic. Current simulation results are encouraging and see promising potential for the LBM method to incorporate more surface complexity with a level of flexibility and transparency above classical CFD modeling.

8.2 Effectiveness of RTD as Diagnostic and Characterization tool

A significant change in mean residence time was detected down to 4 out of 60 blocked channels for the design 1 (slim-header) lamina and 8 out of 60 blocked channels for design 2 (wide-header) and design 3 (wide-posts) laminas. Design 2 fell short of the predicted 4 blocked channel sensitivity limit, while design 1 was able to meet that predicted sensitivity. This is likely due to design 1 having longer microchannels (6 cm versus 5 cm) and smaller header volume. Each blocked microchannel in design 1 then decreases the total volume of the system more significantly.

Based on these findings, the pulse response measurement is a suitable method for detecting defects, so long as what would be classified as a critical failure defect is above the detection limit. Significant defects such collapsed lamina features or

deactivated lamina layers should elicit a significant change in mean residence time. A rough extrapolation can be made by assuming, in a multilayer device of 40 alternating blood and dialysate layers, a pulse response test loop may be capable of detecting a deactivation of 1 of the 20 blood lamina layers (5% decrease in total laminae volume).

The inability to measure mass lost from the system even though the mass balance was closed for most measurements shows an important shortcoming in the current design of the absorbance flow cells. Mass loss correlates to another significant defect in the dialyzer: leakage of fluid to the outside of the laminae or rupture in the dialysis membrane. The tubing and fiber optic cable heads would need to be permanently secured in the flow cell housing using epoxy or glue. This may be achievable in a working diagnostic tool specifically dedicated to this application.

Residence time theory has been applied to various fields of chemical and environmental engineering.[49], [51] The application of this analysis in the microfluidic field is mostly to compare different mixing structures, plate reactors, or heat exchangers operating under ideal conditions.[57], [58], [60], [61] The research presented here differs by not only investigating new microchannel system designs but also the sensitivity of the pulse response measurements at detecting small changes to the system indicative of a defect present. This sensitivity level is a product of many processes: dye choice, dye injection, measurement technique, instrumentation noise, and data processing. These findings present an initial ceiling expectation on the utility of the pulse response method for detecting defects. Significant improvements can be implemented in future pulse response test loops and they should be expected to improve the sensitivity further.

8.3 Design of Microchannel Lamina for Hemodialysis

The four lamina designs chosen for the study represent basic design principles for a microchannel hemodialyzer but also microreactors in general. The first design consists of a narrow, small header that feeds longer channels. The focus of this design is to reduce volume outside of the microchannel array itself. This is a design that is

often seen in heat exchangers where a straight (non-triangular) header feeds a long array of tubes. The second design consists of a larger header without support features, allowing for a two larger volumes on each side of the microchannel array. Larger headers could help to pacify fluctuations in flow by acting as reservoirs. The third design uses the same header outline and microchannel array as the second design and adds micro-post support features to the header volume. The micro-posts utilized in this context assists in reducing dialysis membrane sagging, a common problem in larger area regions of the lamina and under the different pressure gradients create across the membrane under dialysis application. The presence of the micro-posts also creates small, localized rotational flow around each post increasing mixing effects. The fourth design does away with all microchannels and in place of the array is a grid of micro-posts filling the header and main rectangular portion. This design increases overall volume versus microchannels and increases mixing of the bulk fluid. In the context of microreactors, this design increases surface area for heterogeneous reaction versus flat plate reactors.

The mean residence time of the design 1 (slim-header) lamina for the no blockage, control condition was closest to the predicted value of the four types of lamina with the average of measured MRTs showing only -0.3% differences. Based on observations from dye tracer recordings, one reason for the better alignment with predicted MRT for the unblocked lamina versus design 2 (wide-header) is the narrower header of design 1 reduces the bulging of the PDMS sealing layer in the header regions. Although the PDMS was formulated to provide more stiffness to reduce sagging (Section 4.8.2) there was still some bulging of the layer into the header when the assembly was tightened. This bulging is more uniform across the entire header as opposed to sagging issue that was corrected. The bulging could be described as a deflection of material into the header. Because the header of design 1 is narrower, the span length is shorter and the deflection is decreased. The sagging that occurred in early device designs showed an air bubble forming between the PDMS and top platen and this localized defect in the header redistributed fluid flow in the header (see Figure 43). The bulging of the thicker PDMS, as far as was observed

from tracer recordings did not significantly impact the fluid flow pattern in the header, only reducing total volume of the header in the z-direction (see Figure 57A).

The difference in experimental and predicted MRT for the design 1 lamina increased to as much as -9% for the most extreme blockage scenario: 32 of 60 blocked channels. This increase in the MRT difference could be partially attributed to increased stagnation of bubbles in dead regions of the header as a result of the deactivated microchannels. Figure 90 shows the dead flow regions and stagnant bubbles in the headers for design 1 at 32 block channels. The narrower shape of the header inhibited fluid flow in the corner regions of the header that were not feeding or receiving direct flow from the microchannels. Even with high fluid flow rates (up to 3 ml/min) of isopropanol during the priming process, the bubbles remained stationary.

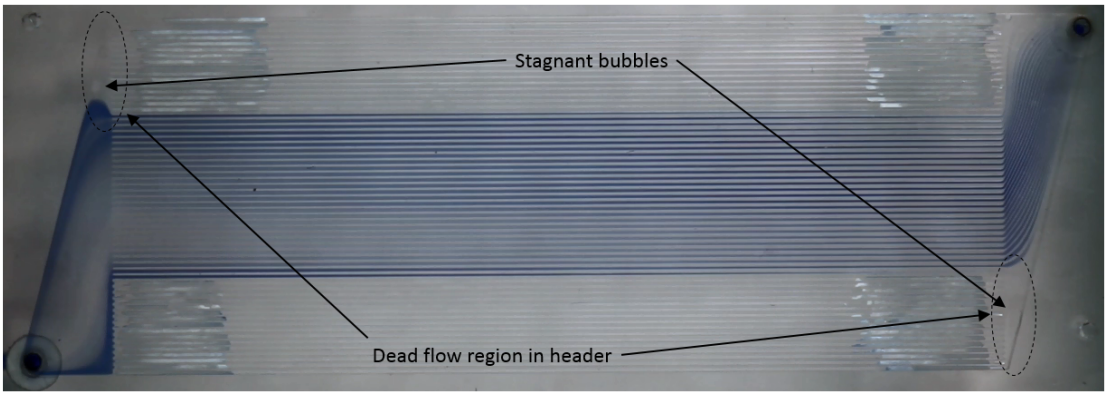

Figure 90. Dead fluid flow regions in the header and stagnant bubbles for the design 1 slim-header lamina at 32 blocked microchannels. Flow from left to right.

The design 2 (wide-header) lamina had a larger difference in MRT at the control condition at a 6.7% decrease in MRT of the pulse response measurement from the predicted value. In addition, overall differences in the MRT for design 2 at the various channel blockage conditions were more consistent than design 1 results, averaging a -6.4% difference. This is in agreement with the description of the physical system above. The wider area of the open header in design 2 resulted in a bulging of the PDMS layer into the lamina, decreasing the volume without significant impact on fluid flow distribution, resulting in a more uniform decrease in MRTs for all blockage conditions compared to predictions.

Additionally, the wider header of design 2 improved priming ability by allowing fluid to move to the header corners and flush most of the stationary bubbles out of the header. Tracer was also able to move further into the corners of the header, either by convection or diffusion, resulting in a greater utilization of the header at higher blockage conditions compared to design 1. Figure 91 shows the blue dye moving into the isolated corner of the entrance header for design 2 at 32 blocked channels. This may have attributed to the more consistent difference between experimental and predicted MRTs over the blockage conditions by minimizing additional effects volume utilization outside of the obstructed microchannels.

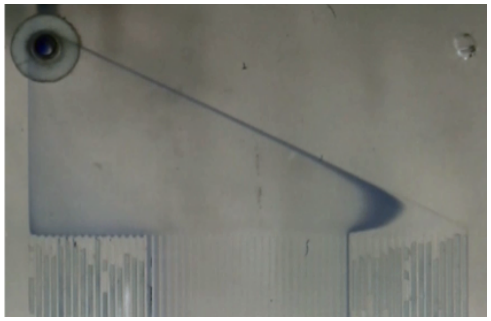

Figure 91. Dye tracer moving into the corner of the entrance header in design 2 wide-header for 32 blocked channel condition.

The average mean residence times for design 3 (wide-posts) are in closer alignment with predicted values. For the no blockage condition, the pulse response MRT showed a 1.6% decrease from the predicted MRT and an average decrease of 3.7% over all measured blockage conditions. This may be attributed to the micro-posts in the headers assisting in lifting up the PDMS layer and maintaining the 100μm depth throughout. Furthermore, the presence of the micro-posts in the headers did not significantly alter the flow pattern of the tracer through the unblocked lamina compared to design 2 results (see Figure 57 and Figure 60).

The mean residence time for design 4 (all-posts) matches up well with predicted values at a 0.6% increase. The predicted values are taken more cautiously than the other lamina designs and the following reasoning given should also be applied to design 3 although to a lesser extent. The shape of the micro-post is not a cylinder of uniform radius, although, that is what is often imagined by hearing the name. Instead, due to the photochemical etching process, the radius of the post

increases moving from the top to the bottom meeting the header floor. This creates some difficulty in accurately measuring the volume within the lamina without a higher resolution 3D surface metrology technique that can piece together a map of the entire lamina surface. Estimation was made using measurements from an optical microscope and measuring software.

The tracer segmented into two primary flows through the design 4 lamina. This was an unexpected observation. Micro-posts grids are becoming increasingly utilized in dialyzer designs associated with this research but also in microreactor research for applications such as fuel production and two-phase separation processes. It was somewhat assumed that the tracer would move in a pseudo-plug flow behavior through the micro-post grid pattern. This segmenting of the fluid flow points to a more complex interaction between header geometry, architectural feature layout and location of inlet and outlet holes, and fabrication reality. The findings place an emphasis on optimizing micro-post grid patterns not only for dialyzer applications but also for all microreactor research within our group.

The variance in an RTD describes the dispersion of a pulse of material through the device. This dispersion is a product of both lamina shearing and diffusion. For this application, the variance for a specific experimental condition is most useful when compared with other conditions measured because the standalone variance accounts for not only the lamina but the extraneous volume within the test loop and therefore cannot provide a clear picture of fluid behavior in the working region of the device (microchannels and headers).

The dimensionless variance of design 1 (slim-header) was on average 23% less than the variance of the design 2 wide-header lamina for 0 to 16 blocked channels. Reducing variance in the RTD of the dialyzer device is important because it reflects less stagnant flow that could potentially promote blood coagulation. Additionally, a narrower RTD profile reflects better homogenization of the flow through the increased ratio of transverse dispersion to longitudinal dispersion, thereby increasing the probability that exit fluid is processed or filtered to similar extent, addressing a major concern of insufficiently filter blood racing through the device faster than the mean residence time.

Design 1 (slim-header) and design 3 (wide-posts) showed closer variance levels in their RTDs at the no blockage condition with approximately 8% difference. The variance increased quickly for design 3 and predominantly had the largest variance overall for the various blocked channel conditions, except for 32 blocked channels in which the three microchannel lamina designs somewhat converge on a similar variance.

Design 4 (all-posts) showed consistently lower variance levels, similar to design 1 for the 0 to 16 blocked channels cases. The obstructions in design 4 do not occupy as much space when compared to the other designs and taking into consideration the deactivated portions of the microchannels. Still, for the obstructions that were measured, variance remained consistent. In reality, based on observations from the priming process, any stationary bubbles in the micro-post grid would not be bulked together in two concise rectangles; instead they would be dispersed randomly through the lamina, creating a tortuous fluid path. This randomness is more so prevalent in the micro-posts laminas than the microchannel laminas due to the opportunities for bubbles to become pinned between each set of micro-posts. Extra measurements were recorded of the unprimed system to provide additional perspective on this design. Those results are listed in the Appendix C.7.

Skewness is a descriptor of the asymmetry of the RTD and hint at the type of dispersion dominating the system. For example, a more symmetric, Gaussian distribution may mean that transverse diffusion is allowing tracer to sample a better average of velocities through the device. Generally, the amount of skew in the measured lamina and conditions were more similar than variance. Design 1 did show lower skewness than the other lamina designs for the 4 through 16 blocked channels conditions. Lower skewness can also imply shortening of the undesirable lagging tail region. In that regard, design 1 outperformed the other lamina but again values are close enough that this small set of data should be taken cautiously. All of the observations discussed in this section are summarized in Table 9.

Table 9 Comparison of the four lamina designs

Lamina Design	Pros	Cons
1. Slim-header	• Closer alignment with predicted MRT for fully operating lamina • Lower RTD variance for no blockage and low blockage • Less skewness in blockage conditions (relatively shorter tailing)	• Difficulty priming at higher blockages • Increased dead volume at higher blockages • Increased RTD variance at the higher blockages (24-32 of 60)
2. Wide-header	• Easier to prime headers • Less dead volume at higher blockages.	• Higher RTD variance at lower blockages • Consistently lower than predicted MRTs may be indicative of header sagging.
3. Wide-posts	• Less RTD variance compared to design 2 for fully operating lamina. • Reduced header sagging and better alignment of MRTs with predictions.	• RTD variance increases quickly once channel blockage occurs.
4. All-posts	• Lower decrease in MRT with obstructions. • Higher area utilization for dialysis mass transfer.	• High bubble stagnation due to fluid bypass • Segmenting of flow by micro-post grid pattern

Taking all the findings collectively, the best performing lamina design was design 1 with the slimmer headers. Although, it is recommended that support posts or features be incorporated with that design as well. The dialysis membrane is softer and more pliable and will be more susceptible to sagging than the PDMS. Design 1 showed less dispersion than other designs at lower blockages, which is more ideal for uniformly filtering all fluid entering the device. It did show increased variance at the higher blockages but that can be partially attributed to the decision to block the

outside most channels, creating dead flow pockets in the header corners. Although one might encounter high levels of blocked channels while operating the dialyzer, it more likely will be in a random configuration.

The all micro-post configuration of design 4 is one that may be utilized in future devices due it its increased surface area utilization for dialysis, a result of having posts instead of microchannel walls. But under this current configuration, the high level of bubble stagnation and flow segmenting presents a new design challenge that must be addressed. In parallel with this work, Mahshid Mohammadi has investigate bubble retention within lamina having different orientation and layout of the micro-post grid.[73]

8.4 CFD Simulated Pulse Response Compared with Experimental Pulse Response

The differences in mean residence times of numerical simulations and experiment currently range from 10% to 32%. On the surface this seems fairly large, especially the design 4 lamina that yielded the 32% difference. These differences are within the range of results from previous investigators that developed numerical simulations for RTD analysis of real fluid system, both macro- and micro-scale. For example, as previously discussed in the literature review, Adeosun and Lawal had differences in MRT between simulation experiment that varied from 12.81% up to 21.84%.[62] The fluid system investigated was a T-junction micromixer. Mendez-Portillo et al. investigated a split-and-recombination microreactor and a multilamination microreactor and had differences in MRT that were as high as 27.8%, although, they also had results within 1.06% error.[65] Shilapuram et al. investigated a larger solar-cyclone reactor system, and yielded differences in MRT of numerical simulations and experimental results between 6.6% and 23.6%.[80] Ultimately, what this shows is that there is still a significant disconnect between the experimental systems and the associated numerical simulations developed in the application of residence time distribution.

For this work, the discrepancy in MRTs between simulation and experiment could be partially attributed to the assumptions and strategies utilized in the

development of the model. The first strategy was segmenting the model into three parts, more specifically two 3-D segments and one 2-D segment, to alleviate the computational burden. For the transitions between segments, the tracer mass was averaged at the exit of the current model segment and uniformly redistributed at entrance of the next model segment. This nullifies any potential concentration distributions but it also solidifies the mass balance. What may occur is moving some of the "early appearing" tracer, preferentially located at the center of the tube, to the slower fluid velocity regions near the walls.

This is a difficult challenge to address when moving from 3-D to 2-D as the tracer in the inlet tubing can be asymmetrically distributed. One strategy is to force the tracer to locations in the lamina entrance that follow a parabolic profile with respect to time. In other words, early tracer is placed at the center of the lamina entrance and as later arriving tracer enters, it is placed increasingly closer to the entrance walls. This approximation may not be suitable for the entrance of the outlet tubing. One reason is that the behavior of the tracer as it exist a lamina is less understood compared the tracer behavior as it exits a tubing section. Another reason is that as we move from 2-D to 3-D segments, we also move from less to more necessary information.

Another reason for the discrepancy in MRTs between experiment and model could be partially ascribed to the 2-D approximation for the lamina segment. The actual lamina has fluid entering normal to the plane of the microchannels and headers but this cannot be recreated in a 2-D lamina and therefore was approximated as in plane, feeding into the corner of the header. Additionally, although the 2-D approximation utilized in *COMSOL* is commonly used for microchannel geometries, these are usually of a rectangular shape and not the semicircular profile in the microchannels and around the micro-posts and header edges that are a result of the etching process. The tapering at the corners of the semicircular profile may have an influence on parabolic fluid velocity profile that is not fully realized in the approximation.

The 2-D shallow channel approximation built into COMSOL has an additional term that acts similar to a drag force (see Equation 30). This decreases the solved

velocities by taking into consideration fluid slowing as our reference point moves closer to the microchannel ceiling and floor when moving in the z-direction, a result of the no-slip boundary condition. This approximation is accurate when considering flow rates through the system but the dampening of the peak velocities in channels and headers increases the breakthrough time of the tracer portion that follows the fastest path through the device, primarily the center of tubing and middle of channels. We see this in results as the general shape of the simulation pulse response is similar to experimental profiles but with a breakthrough time pushed later.

Finally, although most likely a smaller factor compared to the previous two discussed factors, the model was not fully verified for grid independence. Initial work was performed that suggested this was not an issue but attempts to increase grid density in the computational geometry resulted in unsolvable models using available computing resource or the occurrence of odd artifacts in the solution, a known issue with *COMSOL*.

9 CONCLUSIONS AND RECOMMENDATIONS

9.1 Conclusions

The PEO-PB-PEO triblock copolymer coating has a beneficial effect on bubble management by reducing obstruction of microchannels by stationary bubbles. Numerical simulations based on the Lattice Boltzmann modeling approach indicate that beneficial effects are due to the maintenance of a lubricating thin liquid film around the bubble. The experimental and numerical simulation results serve to validate the utility of the PEO-PB-PEO coating (bubble lubrication, biocompatibility, and therapeutic loading). Additionally, we have determined an important design constraint for this and similar multiphase microchannel devices, which is the highest flow velocity that still exhibits the beneficial effect of the coating. Within the scope of this study, that nominal average fluid velocity is approximately 1.8 cm/s (Re = 2.7), but will most likely need to be determined for other micro-scale based geometries with two-phase flow. Nevertheless, understanding the operable range of average fluid velocity in a microchannel hemodialyzer is an important design parameter because lower fluid velocities result in higher filtration, shorter microchannels, decreased damage to blood, but also in increased probability of channel blockage with stationary bubbles.

A test loop was developed for measuring the pulse response of a dye tracer injected into a dialyzer device for the purpose of detecting defects, developing residence time distribution analysis and characterizing lamina design. The results of the test loop as a diagnostic tool for detecting defects were optimistic as it performed close to our expectations and we've learned many important design lessons that should improve the accuracy and precision of the technique. In addition, testing a fully functioning dialyzer would equate to testing larger lamina and multiple layers, increasing the volume of the device and dampening the noise or effects from the extraneous parts of the test loop.

In previous work by our research group and others, it has been found that flow uniformity through the microchannel array is sensitive to header shape (e.g. triangular vs. rectangular), angle of triangular header, vertical spacing between header and microchannels and other factors.[81], [82] Much as flow uniformity is a constraint to

dictate lamina design, so is the residence time distribution. This has been shown through investigation of the residence time distributions of four standard lamina designs for microchannel dialysis and general microreactor application. Although these designs are often utilized, they consist of complex geometries not only for micro chemical processing but also in the field of residence time distribution analysis. The results of this work show that RTD variance tended to lower for designs that are more dominated, volume-wise, by the microchannel array versus the headers. These results have also pointed out a discrepancy between the idealized conceptual device and the real fabricated device by emphasizing how issues such as sagging or bulging, fabrication tolerances, and miniscule misalignments can significantly impact a microchannel device.

Lastly, the numerical model developed for pairing with the pulse response test loop and dialyzer showed promising results. There was good agreement between visual observation of the tracer in simulations and experiments, and the shape and peak height of the output profiles. The model still requires improvements in assumptions and approximations to bring mean residence times into closer alignment before this method can be presented as a significant advancement from previous work in the field of microreactor RTD modeling.

9.2 Future Work and Recommendations

Future work, specifically for the pulse response measurements and RTD analysis, is to apply this characterization technique into other microreactor technology fields. Towards the end of this research, tracer measurements had already been applied to larger microreactor systems. In the Ph.D. research of Frederick Atadana, we utilized the measuring techniques developed in this work to arrive at a mean residence time that he then applied to numerical simulations to solve for reaction coefficients.[20] In addition to the traditional single-phase pulse response measurements, early attempts were made to apply this technique to two-phase flow. Results were mixed but promising and this application could be feasible with further investigation into data processing and filtering techniques. There are various other

microreactor applications within this research group and residence time studies can provide additional understanding of the systems. Many of these microreactors are fabricated from stainless steel and hermetically sealed via laser welds, which restricts our ability to verify if defects were present in the system without opening up the device after the experiment.

With regard to dialysis, the larger lamina designs and enclosure device developed for this investigation will be transferred to continuing research to improve device sealing for multilayer laminae through the incorporation of sealing boss architecture and improve dialysis membrane utilization. The offset locations for the inlet and outlet holes allows for any of the four larger lamina designs to be immediately used a multilayer device for both blood and dialysate fluid compartments without further modification to the metal master plates used in fabrication. The micro-posts used in design 3 and 4 were planned in a layout that would mate precisely with the opposite facing lamina's micro-posts to support the dialysis membrane.

A recommendation for the PEO-coating application would be to investigate the effect of the coating in the presence of a complex biological fluid such as blood or plasma. The presence of the coating should not have a negative effect on bubble stagnation in blood or plasma but we cannot say for certain from this work whether it would have a beneficial effect on bubble management within the device. This does not take away from the fact that the PEO-coating still serves an important role in the blood compartment side by reducing protein fouling and with the addition of tethered therapeutic drugs, may have the potential to serve many other useful functions.

It is recommended that for the pulse response and residence time studies, the fluid tubing and fiber optic cable heads should be secured permanently within the flow cells for consistent closure of the mass balance which would allow for detecting mass loss in the device due to leakage. Additionally, I recommend continuing the iterative design process of bringing the flow cells closer into the device while maintain a discrete diagnostic tool that allows you to easily interchange different microchannel devices.

It is also recommended that a pulse response investigation eventually be conducted on the multilayer dialyzers and blood processing devices under development. With multiple lamina layers comes new fabrication and assembly challenges and a pulse response measurement and associated residence time distribution can verify whether the physical device is in good agreement with the intended designs and can assist in deciphering discrepancies between experimental results and numerical simulations.

Lastly, regarding CFD modeling of tracer pulse response, it is recommended that any future iterations on the design of the experimental test loop and dialyzer device incorporate features that would make translating it to a computer simulation and solving easier. The challenges encountered when modeling this system have already been discussed in Section 8.4. Some of these challenges could be addressed in the physical system instead of the numerical simulation. For example, feeding the tubing from the flow cells vertically through the top compression platen directly over the lamina fluid through hole instead of horizontally through the sides would provide more axisymmetric distribution of the tracer as it travels through the inlet tubing by avoiding an elbow in the current system. This may allow for improved approximation of the tracer moving from the inlet tubing segment to the lamina segment of the model. And there may be additional improvements to the physical device that would assist in improving the model.

REFERENCES

[1] "U.S. Renal Data System, USRDS 2013 Annual Data Report: Atlas of Chronic Kidney Disease and End-Stage Renal Disease in the United States," National Institutes of Health, National Institute of Diabetes and Digestive and Kidney Diseases, Bethesda, MD, 2013.

[2] D. U. Silverthorn, *Human physiology: an integrated approach*. Pearson/Benjamin Cummings, 2004.

[3] Renal Association, "Normal GFR." [Online]. Available: http://www.renal.org/information-resources/the-uk-eckd-guide/normal-gfr#sthash.B2G9tg2N.A0Kk6wve.dpbs. [Accessed: 15-Nov-2014].

[4] "About Chronic Kidney Disease." [Online]. Available: https://www.kidney.org/kidneydisease/aboutckd. [Accessed: 15-Nov-2014].

[5] National Kidney Foundation, "KDOQI CKD Guidelines," 2002. [Online]. Available: http://www2.kidney.org/professionals/KDOQI/guidelines_ckd/toc.htm. [Accessed: 15-Nov-2014].

[6] R. M. Lindsay, F. Alhejaili, G. Nesrallah, R. Leitch, L. Clement, A. P. Heidenheim, and C. Kortas, "Calcium and phosphate balance with quotidian hemodialysis," *Am. J. Kidney Dis.*, vol. 42, no. 1 Suppl, pp. 24–29, Jul. 2003.

[7] R. S. Lockridge, H. K. Anderson, L. T. Coffey, V. W. Craft, F. M. Jennings, L. L. McPhatter, M. O. Spencer, and A. C. Swafford, "Nightly Home Hemodialysis in Lynchburg, Virginia: Economic and Logistic Considerations," *Seminars in Dialysis*, vol. 12, no. 6, pp. 440–447, Dec. 1999.

[8] A. Pierratos, "Nocturnal home haemodialysis: an update on a 5-year experience," *Nephrol. Dial. Transplant.*, vol. 14, no. 12, pp. 2835–2840, Dec. 1999.

[9] A. R. Tuhy, E. K. Anderson, and G. N. Jovanovic, "Urea separation in flat-plate microchannel hemodialyzer; experiment and modeling," *Biomed Microdevices*, vol. 14, no. 3, pp. 595–602, Jun. 2012.

[10] A. Tonkovich, D. Kuhlmann, A. Rogers, J. McDaniel, S. Fitzgerald, R. Arora, and T. Yuschak, "Microchannel Technology Scale-up to Commercial Capacity," *Chemical Engineering Research and Design*, vol. 83, no. 6, pp. 634–639, Jun. 2005.

[11] G. Jovanovic, J. McGuire, B. Paul, and K. Sharp, "Microchannel Dialyzer Development Grant no. NBIB 1 R01 EB011567-01A1," Grant no. NBIB 1 R01 EB011567-01A1.

[12] K. Heintz, "Synthesis and evaluation of PEO-coated materials for microchannel-based hemodialysis," Aug. 2012.

[13] C.-H. Ho, L. Limberis, K. D. Caldwell, and R. J. Stewart, "A metal-chelating pluronic for immobilization of histidine-tagged proteins at interfaces: immobilization of firefly luciferase on polystyrene beads," *Langmuir*, vol. 14, no. 14, pp. 3889–3894, 1998.

[14] Y.-C. Tai, J. McGuire, and J. A. Neff, "Nisin antimicrobial activity and structural characteristics at hydrophobic surfaces coated with the PEO-PPO-PEO triblock surfactant Pluronic® F108," *J Colloid Interface Sci*, vol. 322, no. 1, pp. 104–111, Jun. 2008.

[15] R. B. Bird, W. E. Stewart, and E. N. Lightfoot, *Transport Phenomena, Revised 2nd Edition*, 2nd edition. New York: John Wiley & Sons, Inc., 2006.
[16] Y. Song, L. L. Henry, and W. Yang, "Stable Amorphous Cobalt Nanoparticles Formed by an in Situ Rapidly Cooling Microfluidic Process," *Langmuir*, vol. 25, no. 17, pp. 10209–10217, 2009.
[17] Y. Song and L. L. Henry, "Nearly Monodispersion CoSm Alloy Nanoparticles Formed by an In-situ Rapid Cooling and Passivating Microfluidic Process," *Nanoscale Res Lett*, vol. 4, no. 10, pp. 1130–1134, Jun. 2009.
[18] A. Warner-Tuhy, "Mass transfer of urea, creatinine and vitamin B-12 in a microchannel based membrane separation unit," Dec. 2009.
[19] E. K. (Eric K. Anderson, "Prediction of mass transfer performance of microchannel dialyzers using deconvolution of impulse-response experiments," Nov. 2009.
[20] F. W. Atadana, "Production of biohydrodeoxygenated diesel in a novel microscale reactor : experiments and modeling," Jun. 2014.
[21] M. N. Kashid, A. Renken, and L. Kiwi-Minsker, "Gas–liquid and liquid–liquid mass transfer in microstructured reactors," *Chemical Engineering Science*, vol. 66, no. 17, pp. 3876–3897, Sep. 2011.
[22] M. T. Kruetzer, *Hydrodynamics of Taylor Flow in Capillaries and Monolith Reactors*. Delft University Press, 2003.
[23] C.-H. Choi, K. J. A. Westin, and K. S. Breuer, "Apparent slip flows in hydrophilic and hydrophobic microchannels," *Physics of Fluids (1994-present)*, vol. 15, no. 10, pp. 2897–2902, Sep. 2003.
[24] Y. Zhu and S. Granick, "Rate-Dependent Slip of Newtonian Liquid at Smooth Surfaces," *Phys. Rev. Lett.*, vol. 87, no. 9, p. 096105, Aug. 2001.
[25] E. Bonaccurso, H.-J. Butt, and V. S. J. Craig, "Surface roughness and hydrodynamic boundary slip of a newtonian fluid in a completely wetting system," *Phys. Rev. Lett.*, vol. 90, no. 14, p. 144501, Apr. 2003.
[26] K. Watanabe and H. Udagawa, "Drag reduction of non-newtonian fluids in a circular pipe with a highly water-repellent wall," *AIChE J.*, vol. 47, no. 2, pp. 256–262, Feb. 2001.
[27] R. Pit, H. Hervet, and L. Léger, "Direct Experimental Evidence of Slip in Hexadecane: Solid Interfaces," *Phys. Rev. Lett.*, vol. 85, no. 5, pp. 980–983, Jul. 2000.
[28] D. C. Tretheway and C. D. Meinhart, "Apparent fluid slip at hydrophobic microchannel walls," *Physics of Fluids (1994-present)*, vol. 14, no. 3, pp. L9–L12, Mar. 2002.
[29] V. Hessel, A. Renken, J. C. Schouten, and J. Yoshida, Eds., *Micro Process Engineering: A Comprehensive Handbook*, 1 edition. Weinheim: Wiley-VCH, 2009.
[30] J. C. T. Eijkel and A. van den Berg, "Water in micro- and nanofluidics systems described using the water potential," *Lab Chip*, vol. 5, no. 11, pp. 1202–1209, Oct. 2005.
[31] V. S. Ajaev and G. M. Homsy, "Modeling Shapes and Dynamics of Confined Bubbles," *Annual Review of Fluid Mechanics*, vol. 38, no. 1, pp. 277–307, 2006.

[32] M. J. Fuerstman, A. Lai, M. E. Thurlow, S. S. Shevkoplyas, H. A. Stone, and G. M. Whitesides, "The pressure drop along rectangular microchannels containing bubbles," *Lab on a Chip*, vol. 7, no. 11, p. 1479, 2007.
[33] T. Cubaud and C.-M. Ho, "Transport of bubbles in square microchannels," *Physics of Fluids (1994-present)*, vol. 16, no. 12, pp. 4575–4585, Nov. 2004.
[34] C. Jacobs, *Replacement of Renal Function by Dialysis*. Springer, 1996.
[35] M. Barak, F. Nakhoul, and Y. Katz, "Reviews: Pathophysiology and Clinical Implications of Microbubbles during Hemodialysis: PATHOPHYSIOLOGY AND CLINICAL IMPLICATIONS OF MICROBUBBLES," *Seminars in Dialysis*, vol. 21, no. 3, pp. 232–238, Mar. 2008.
[36] C. Litterst, T. Metz, R. Zengerle, and P. Koltay, "Static and dynamic behaviour of gas bubbles in T-shaped non-clogging micro-channels," *Microfluid Nanofluid*, vol. 5, no. 6, pp. 775–784, Apr. 2008.
[37] A. M. Skelley and J. Voldman, "An active bubble trap and debubbler for microfluidic systems," *Lab Chip*, vol. 8, no. 10, pp. 1733–1737, Sep. 2008.
[38] J. Xu, R. Vaillant, and D. Attinger, "Use of a porous membrane for gas bubble removal in microfluidic channels: physical mechanisms and design criteria," *Microfluid Nanofluid*, vol. 9, no. 4–5, pp. 765–772, Mar. 2010.
[39] L. Clime, D. Brassard, J. P. Pezacki, and T. Veres, "Self-priming of liquids in capillary autonomous microfluidic systems," *Microfluid Nanofluid*, vol. 12, no. 1–4, pp. 371–382, Sep. 2011.
[40] C. Lochovsky, S. Yasotharan, and A. Günther, "Bubbles no more: in-plane trapping and removal of bubbles in microfluidic devices," *Lab Chip*, vol. 12, no. 3, pp. 595–601, Jan. 2012.
[41] M. Mohammadi and K. V. Sharp, "The Role of Contact Line (Pinning) Forces on Bubble Blockage in Microchannels," *Journal of Fluids Engineering*, vol. 137, no. 3, p. 031208, Mar. 2015.
[42] K. Heintz, K. F. Schilke, J. Snider, W.-K. Lee, M. Truong, M. Coblyn, G. Jovanovic, and J. McGuire, "Preparation and evaluation of PEO-coated materials for a microchannel hemodialyzer," *J. Biomed. Mater. Res.*, vol. 102, no. 5, pp. 1014–1020, Jul. 2014.
[43] A. Halperin, "Compression induced phase transitions in PEO brushes: the n-cluster model," *Eur. Phys. J. B*, vol. 3, no. 3, pp. 359–364, Jun. 1998.
[44] S. R. Sheth and D. Leckband, "Measurements of attractive forces between proteins and end-grafted poly(ethylene glycol) chains," *PNAS*, vol. 94, no. 16, pp. 8399–8404, Aug. 1997.
[45] Y.-C. Tai, P. Joshi, J. McGuire, and J. A. Neff, "Nisin adsorption to hydrophobic surfaces coated with the PEO–PPO–PEO triblock surfactant Pluronic® F108," *Journal of Colloid and Interface Science*, vol. 322, no. 1, pp. 112–118, Jun. 2008.
[46] H. Lee, D. H. Kim, K. N. Witte, K. Ohn, J. Choi, B. Akgun, S. Satija, and Y.-Y. Won, "Water Is a Poor Solvent for Densely Grafted Poly(ethylene oxide) Chains: A Conclusion Drawn from a Self-Consistent Field Theory-Based Analysis of Neutron Reflectivity and Surface Pressure–Area Isotherm Data," *J. Phys. Chem. B*, vol. 116, no. 24, pp. 7367–7378, Jun. 2012.

[47] M. Wagner, F. Brochard-Wyart, H. Hervet, and P.-G. de Gennes, “Colloid & Polymer Science,” *Colloid Polym Sci*, vol. 271, no. 7, pp. 621–628, Jul. 1993.
[48] T. Hu and C. Wu, “Clustering Induced Collapse of a Polymer Brush,” *Phys. Rev. Lett.*, vol. 83, no. 20, pp. 4105–4107, Nov. 1999.
[49] O. Levenspiel, *Chemical Reaction Engineering, 3rd Edition*, 3 edition. New York: Wiley, 1998.
[50] O. Levenspiel, *Tracer Technology: Modeling the Flow of Fluids*. Springer Science & Business Media, 2011.
[51] E. B. Nauman, “Residence Time Theory,” *Ind. Eng. Chem. Res.*, vol. 47, no. 10, pp. 3752–3766, May 2008.
[52] J. J. Carberry and R. H. Bretton, “Axial dispersion of mass in flow through fixed beds,” *AIChE J.*, vol. 4, no. 3, pp. 367–375, 1958.
[53] “Micro and Nanoscale Fluid Mechanics Transport in Microfluidic Devices | Thermal-fluids engineering,” *Cambridge University Press*. [Online]. Available: http://www.cambridge.org/us/academic/subjects/engineering/thermal-fluids-engineering/micro-and-nanoscale-fluid-mechanics-transport-microfluidic-devices?format=HB. [Accessed: 16-Jan-2015].
[54] R. Aris, “On the Dispersion of a Solute in a Fluid Flowing through a Tube,” *Proceedings of the Royal Society of London A: Mathematical, Physical and Engineering Sciences*, vol. 235, no. 1200, pp. 67–77, Apr. 1956.
[55] F. Trachsel, A. Günther, S. Khan, and K. F. Jensen, “Measurement of residence time distribution in microfluidic systems,” *Chemical Engineering Science*, vol. 60, no. 21, pp. 5729–5737, Nov. 2005.
[56] A. Cantu-Perez, S. Barrass, and A. Gavriilidis, “Residence time distributions in microchannels: Comparison between channels with herringbone structures and a rectangular channel,” *Chemical Engineering Journal*, vol. 160, no. 3, pp. 834–844, Jun. 2010.
[57] A. Cantu-Perez, S. Bi, S. Barrass, M. Wood, and A. Gavriilidis, “Residence time distribution studies in microstructured plate reactors,” *Applied Thermal Engineering*, vol. 31, no. 5, pp. 634–639, Apr. 2011.
[58] E. Georget, J. L. Sauvageat, A. Burbidge, and A. Mathys, “Residence time distributions in a modular micro reaction system,” *Journal of Food Engineering*, vol. 116, no. 4, pp. 910–919, Jun. 2013.
[59] A. A. V. N Reis, “Liquid backmixing in oscillatory flow through a periodically constricted meso-tube,” *Chemical Engineering and Processing*, vol. 49, pp. 793–803, 2010.
[60] D. Bošković and S. Loebbecke, “Modelling of the residence time distribution in micromixers,” *Chemical Engineering Journal*, vol. 135, Supplement 1, pp. S138–S146, Jan. 2008.
[61] D. Bošković, S. Loebbecke, G. A. Gross, and J. M. Koehler, “Residence Time Distribution Studies in Microfluidic Mixing Structures,” *Chem. Eng. Technol.*, vol. 34, no. 3, pp. 361–370, 2011.
[62] J. T. Adeosun and A. Lawal, “Numerical and experimental studies of mixing characteristics in a T-junction microchannel using residence-time distribution,” *Chemical Engineering Science*, vol. 64, no. 10, pp. 2422–2432, May 2009.

[63] J.-H. Ham and B. Platzer, “Semi-Empirical Equations for the Residence Time Distributions in Disperse Systems – Part 1: Continuous Phase,” *Chem. Eng. Technol.*, vol. 27, no. 11, pp. 1172–1178, 2004.
[64] J. T. Adeosun and A. Lawal, “Numerical and experimental mixing studies in a MEMS-based multilaminated/elongational flow micromixer,” *Sensors and Actuators B: Chemical*, vol. 139, no. 2, pp. 637–647, Jun. 2009.
[65] L. S. Méndez-Portillo, M. Heniche, C. Dubois, and P. A. Tanguy, “Numerical investigation of the hydrodynamics of split-and-recombination and multilamination microreactors,” *AIChE J*, vol. 59, no. 3, pp. 988–1001, 2013.
[66] M. Heniche, P. A. Tanguy, M. F. Reeder, and J. B. Fasano, “Numerical investigation of blade shape in static mixing,” *AIChE J.*, vol. 51, no. 1, pp. 44–58, 2005.
[67] H. Kasban, O. Zahran, H. Arafa, M. El-kordy, S. Elaraby, and F. E. A. El-Samie, “An efficient approach for Residence Time Distribution signal processing and identification,” in *2010 The 7th International Conference on Informatics and Systems (INFOS)*, 2010, pp. 1–8.
[68] P. A. Jansson, *Deconvolution: with applications in spectroscopy*. Academic Press, 1984.
[69] P. A. JANSSON, R. H. HUNT, and E. K. PLYLER, “Resolution Enhancement of Spectra,” *J. Opt. Soc. Am.*, vol. 60, no. 5, pp. 596–599, May 1970.
[70] B. K. Paul and D. K. Ward, “The Hermeticity of Compression Seals in Microchannel Hemodialyzers,” *J. Micro Nano-Manuf.*, vol. 2, no. 3, pp. 031006–031006, Jul. 2014.
[71] S. D. Porter, “Development of self-registration features for the assembly of a microchannel hemodialyser,” Sep. 2012.
[72] D. Ward, “Determining the dimensional requirements of a reliable compression sealing method for use in microchannel hemodialysers,” 2013.
[73] M. Mohammadi, “Design of a single lamina for a microchannel dialyzer with a focus on bubble removal,” Oregon State University, Corvallis, OR, 2014.
[74] X.-Y. Zhang, “Determination for the Diffusion Coefficient of Organic Molecule in Micro-channels by No Membrane Diffusion,” Northeastern University, 2008.
[75] S. Chapra, *Applied Numerical Methods W/MATLAB: for Engineers & Scientists*, 3 edition. New York: McGraw-Hill Science/Engineering/Math, 2011.
[76] H. Huang, D. T. Thorne Jr, M. G. Schaap, and M. C. Sukop, “Proposed approximation for contact angles in Shan-and-Chen-type multicomponent multiphase lattice Boltzmann models,” *Phys Rev E Stat Nonlin Soft Matter Phys*, vol. 76, no. 6 Pt 2, p. 066701, Dec. 2007.
[77] K. Fei, W. H. Chen, and C. W. Hong, “Microfluidic analysis of CO2 bubble dynamics using thermal lattice-Boltzmann method,” *Microfluid Nanofluid*, vol. 5, no. 1, pp. 119–129, Jul. 2008.
[78] P.-G. de Gennes, F. Brochard-Wyart, and D. Quere, “Capillarity and Wetting Phenomena: Drops, Bubbles, Pearls, Waves,” New York: Springer, 2003, pp. 37, 153–174.
[79] S. Chen, L. Li, C. Zhao, and J. Zheng, “Surface hydration: Principles and applications toward low-fouling/nonfouling biomaterials,” *Polymer*, vol. 51, no. 23, pp. 5283–5293, Oct. 2010.

[80] V. Shilapuram, D. Jaya Krishna, and N. Ozalp, “Residence time distribution and flow field study of aero-shielded solar cyclone reactor for emission-free generation of hydrogen,” *International Journal of Hydrogen Energy*, vol. 36, no. 21, pp. 13488–13500, Oct. 2011.
[81] M. Mohammadi, G. N. Jovanovic, and K. V. Sharp, “Numerical study of flow uniformity and pressure characteristics within a microchannel array with triangular manifolds,” *Computers & Chemical Engineering*, vol. 52, pp. 134–144, May 2013.
[82] R. Manikanda Kumaran, G. Kumaraguruparan, and T. Sornakumar, “Experimental and numerical studies of header design and inlet/outlet configurations on flow mal-distribution in parallel micro-channels,” *Applied Thermal Engineering*, vol. 58, no. 1–2, pp. 205–216, Sep. 2013.

Appendices

LIST OF APPENDICES

LIST OF APPENDICES (Continued)

Page

LIST OF APPENDIX FIGURES

LIST OF APPENDIX FIGURES (Continued)

LIST OF APPENDIX TABLES

Appendix A: Supplementary Materials and Methods

A.1 Stainless Steel Annealing Protocol in Vacuum Furnace

Table 10 Sequence for annealing PCM master plates

Step	Vacuum	Temp. set pt. (^{o}C)	Time span (min)
1	Pump	0	30
2	Pump	1040	51, vacuum delay 25 min
3	Pump	1040	20
4	Pump	100	30
5	Pump	30	3, guaranteed soak 25 min
6	Purge to atmospheric	30	1

A.2 Protocol for embossing stainless steel into PEI

1. Cool (Top = 20°C, Bottom = 20°C)
2. Wait until temp =< 40°C (top and bottom)
3. Place tool, substrate, and backing plate in chamber
4. Heat (Top=147°C, Bottom=147°C)
5. Close chamber
6. Move top down (Position = -3.0 mm, Velocity = 50.0 mm/min, MaxForce = 2000 N)
7. Evacuate chamber
8. Move top down (Position = -9.0 mm, Velocity = 50.0 mm/min, MaxForce = 2000 N)
9. Apply touch force = 300 N
10. Heat (Top=190°C, Bottom=190°C)
11. Wait until temp >= 180°C (top and bottom)
12. Hold temperature (Top = 218°C, Bottom = 218°C)
13. Wait until temp >= 216°C (top and bottom)
14. Apple force = 50,000 N (Velocity = 1.0 mm/min)
15. Wait 1500 seconds
16. Cool (Top=125°C, Bottom=125°C)
17. Wait 10 seconds
18. Apple force = 5000 N (Velocity = 1.0 mm/min)
19. Move top down (Position = 3.0 mm, Velocity = 50.0 mm/min, MaxForce = 10,000 N)
20. Open chamber
21. Cool (Top = 20°C, Bottom = 20°C)

A.3 ESI laser setttings for trimming PEI

4 step cut, stepping down 0.25 mm each cut

- Velocity: 100.0 mm/sec
- RepRate: 30.0 kHz
- Laser Power: 4.5 watts
- Bite Size: 3.33 μm
- Pulse: 150.0 μJ
- Repetitions: 15
- Imaging: Off
- Smoothing: Off

A.4 Protocol for embossing PEI into polycarbonate

1. Hold temperature (Top = 140^{o}C, Bottom = 140^{o}C)
2. Wait until temp >= 135^{o}C (top and bottom)
3. Place tool, substrate, and backing plate in chamber
4. Heat (Top=147^{o}C, Bottom=147^{o}C)
5. Close chamber
6. Move top down (Position = -12.0 mm, Velocity = 50.0 mm/min, MaxForce = 2000 N)
7. Apply touch force = 300 N
8. Evacuate chamber
9. Wait until temp >= 143^{o}C (bottom)
10. Hold temperature (Top = 149^{o}C, Bottom = 149^{o}C)
11. Wait until temp >= 147^{o}C (all sensors)
12. Apple force = 50,000 N (Velocity = 1.0 mm/min)
13. Wait 9000 seconds
14. Cool (Top=25^{o}C, Bottom=25^{o}C)
15. Wait until temp =< 140^{o}C (bottom)
16. Wait 40 seconds
17. Hold temperature (Top = 140^{o}C, Bottom = 140^{o}C)
18. Apple force = 5000 N (Velocity = 1.0 mm/min)
19. Move top down (Position = 3.0 mm, Velocity = 50.0 mm/min, MaxForce = 2000 N)
20. Open chamber
21. Hold temperature (Top = 125^{o}C, Bottom = 125^{o}C)

A.5 ESI laser setttings for trimming polycarbonate

3 step cut, stepping down 0.25 mm each cut

- Velocity: 150.0 mm/sec
- RepRate: 30.0 kHz
- Laser Power: 1.6 watts
- Bite Size: 5.0 μm
- Pulse: 53.333 μJ
- Repetitions: 50
- Imaging: Off
- Smoothing: On

Appendix B: Various Matlab scripts for processing data

B.1 Script for loading raw scope data into Matlab

```
%Loads scope txt into matlab arrays and renames
dummy1 = dlmread('run1b_1108179U2.TXT',';',9,0);
                  run1b = dummy1(1:2,:)';
dummy2 = dlmread('run1a_1108180U2.TXT',';',9,0);
                  run1a = dummy2(1:2,:)';

clear dummy1 dummy2

dummy1 = dlmread('run2b_1108179U2.TXT',';',9,0);
                  run2b = dummy1(1:2,:)';
dummy2 = dlmread('run2a_1108180U2.TXT',';',9,0);
                  run2a = dummy2(1:2,:)';

clear dummy1 dummy2

dummy1 = dlmread('run3b_1108179U2.TXT',';',9,0);
                  run3b = dummy1(1:2,:)';
dummy2 = dlmread('run3a_1108180U2.TXT',';',9,0);
                  run3a = dummy2(1:2,:)';

clear dummy1 dummy2
.
.
.
```

B.2 Script for converting scope values into absorbance values and adjusting for different flow cell path lengths.

```
%Transform scope data to absorbance, calculate integral and plot

for q = 1:10;

eval(['[ inlet_clean ]  = scope_clean( run' num2str(q) 'a);']);
eval(['[ outlet_clean ]  = scope_clean( run' num2str(q) 'b);']);

[ inlet_abs , inlet_time ] = scope_abs_mod031914( inlet_clean );
[ outlet_abs , outlet_time ] = scope_abs_mod031914( outlet_clean );

plot(inlet_time,inlet_abs,'r')
hold on
plot(outlet_time,outlet_abs,'b')
xlabel('Time (s)')
ylabel('Absorbance')
%title('title')
legend('input','output')
% axis ([0,inlet_time(end),0,max(inlet_abs)+0.1])
hold off
shg

% calculate area under the curve for inlet
integra = cumtrapz (inlet_time, inlet_abs);
auc_i = integra(end);

% calculate area under the curve for outlet
integra = cumtrapz (outlet_time, outlet_abs);
auc_o = integra(end);

% calculate difference percentage
auc_diff = (auc_i-auc_o)/(auc_i)*100;

% rename conventional variables
eval(['i' num2str(q) 'a = inlet_abs;']);
eval(['i' num2str(q) 't = inlet_time;']);
eval(['i' num2str(q) 'i = auc_i;']);
eval(['o' num2str(q) 'a = outlet_abs;']);
eval(['o' num2str(q) 't = outlet_time;']);
eval(['o' num2str(q) 'i = auc_o;']);
eval(['d' num2str(q) 'i = auc_diff;']);

end

clear auc_i auc_o auc_diff inlet_abs inlet_time inlet_mass
outlet_abs outlet_time outlet_mass integra flowrate inlet_clean
outlet_clean q;
```

B.3 Function file for converting scope to absorbance values

```
function [data_a,time] = scope_abs_mod031914( data_s )

%conversion of scope data to absorbance data
%function [data_a,time] = scope_abs( data_s )
%time is in units of seconds
%data_a = absorbance array

k = length(data_s);

dark = data_s(2,2);

ref = mean(data_s(k-40:k,2));

data_s2 = data_s(4:k,2);

time1 = data_s(4:k,1);

time = time1/(100*1000);

data_a = -log10((data_s2-dark)/(ref-dark));

end
```

B.4 Converting absorbance data into normalized curves

```
% define data range set and tolerance level for rounding values to
zero
range= 1:10;
tolerance = 0.0001

clf

% Calculate the first batch of mean res times and shifted time
vectors
for k = range;

eval(['time1 = i' num2str(k) 't;']);
eval(['abso1 = i' num2str(k) 'a;']);
eval(['time2 = o' num2str(k) 't;']);
eval(['abso2 = o' num2str(k) 'a;']);

mrt1 = time1'*abso1/sum(abso1);
mrt2 = time2'*abso2/sum(abso2);

mrt_diff = mrt2-mrt1;

eval(['rtdi' num2str(k) '= mrt1;']);
eval(['rtdo' num2str(k) '= mrt2;']);
eval(['rtdm' num2str(k) '= mrt_diff;']);

eval(['i' num2str(k) 'tz = i' num2str(k) 't - mrt1;']);
eval(['o' num2str(k) 'tz = o' num2str(k) 't - mrt1;']);

end
clear mrt1 mrt2 mrt_diff time1 time2 abso1 abso2 k

%%%%%%%%%%%%%%%%%%%%%%%%%%%%%%%%%%%%%%%%%%%%%%%%%%%%%%%%%%%%%%%%%%%

% Set threshold for values below tolerance limit be zero

for k = range;

eval(['time1 = i' num2str(k) 't;']);
eval(['abso1 = i' num2str(k) 'a;']);
eval(['time2 = o' num2str(k) 't;']);
eval(['abso2 = o' num2str(k) 'a;']);
eval(['mrt = rtdm' num2str(k) ';']);

[~,i]=max(abso1);
[~,j]=max(abso2);
s = length(abso1);
d = length(abso2);

q=i;
w=j;
```

```
while abso1(i)>0.1
    i=i-1;
    if i<=0
        i=1;
        break
    end
end

abso1(1:i)=0;

while mean(abso1(q-10:q))>tolerance*max(abso1)
    q=q+1;
    if q>=s
        q=s;
        break
    end
end

abso1(q:s)=0;

while abso2(j)>0
    j=j-1;
    if j<=0
        j=1;
        break
    end
end

abso2(1:j)=0;

while mean(abso2(w-10:w))>tolerance*max(abso2)
    w=w+1;
    if w>=d
        w=d;
        break
    end
end

abso2(w:d)=0;

% calculate area under the curve for inlet
integra = cumtrapz (time1, abso1);
auc_i = integra(end);

% calculate area under the curve for outlet
integra = cumtrapz (time2, abso2);
auc_o = integra(end);

% calculate difference percentage
auc_diff = (auc_i-auc_o)/(auc_i)*100;

eval(['i' num2str(k) 'ad = abso1;']);
eval(['o' num2str(k) 'ad = abso2;']);
eval(['i' num2str(k) 'id = auc_i;']);
```

```
eval(['o' num2str(k) 'id = auc_o;']);
eval(['d' num2str(k) 'id = auc_diff;']);

end

clear time1 time2 abso1 abso2 k integra auc_i auc_o auc_diff mrt i j
s d q w

%%%%%%%%%%%%%%%%%%%%%%%%%%%%%%%%%%%%%%%%%%%%%%%%%%%%%%%%%%%%%%%%%%

% Normalize absorbance data (area under curve = 1)

for k = range

eval(['time1 = i' num2str(k) 't;']);
eval(['abso1 = i' num2str(k) 'ad;']);
eval(['time2 = o' num2str(k) 't;']);
eval(['abso2 = o' num2str(k) 'ad;']);

% define delta time
DeltaTime1 = time1(2)-time1(1);
DeltaTime2 = time2(2)-time2(1);

% define denominator
D1 = abso1*DeltaTime1;
D2 = abso2*DeltaTime2;

Denom1 = sum(D1);
Denom2 = sum(D2);

% normalize density
E1 = abso1/Denom1;
E2 = abso2/Denom2;

eval(['i' num2str(k) 'adn = E1;']);
eval(['o' num2str(k) 'adn = E2;']);

end

clear time1 time2 abso1 abso2 DeltaTime1 DeltaTime2 D1 D2 Denom1
Denom2 E1 E2

%%%%%%%%%%%%%%%%%%%%%%%%%%%%%%%%%%%%%%%%%%%%%%%%%%%%%%%%%%%%%%%%%%

% Recalculate mean res times

for k = range;

eval(['time1 = i' num2str(k) 't;']);
eval(['abso1 = i' num2str(k) 'adn;']);
eval(['time2 = o' num2str(k) 't;']);
eval(['abso2 = o' num2str(k) 'adn;']);
```

```
mrt1 = time1'*abso1/sum(abso1);
mrt2 = time2'*abso2/sum(abso2);

mrt_diff = mrt2-mrt1;

eval(['rtdidn' num2str(k) '= mrt1;']);
eval(['rtdodn' num2str(k) '= mrt2;']);
eval(['rtdmdn' num2str(k) '= mrt_diff;']);
eval(['RTDmdnList(' num2str(k) ',1)= mrt_diff;']);

eval(['i' num2str(k) 'tzd = i' num2str(k) 't - mrt1;']);
eval(['o' num2str(k) 'tzd = o' num2str(k) 't - mrt1;']);

% Plot profiles with each data set calculation
plot(time1,abso1,'r')
hold on
plot(time2,abso2,'b')
xlabel('Time (s)')
ylabel('Total mass')
%title('title)
legend('input','output')
%axis ([0,time1(end)])
hold off

shg
pause(0.5)
end
clear mrt1 mrt2 mrt_diff time1 time2 abso1 abso2 k range
```

B.5 Adaptive noise dampening using filter with variable span length

```
clf

% range defines the number of data sets to handle
range = 1:10;

for k = range;

% load and cycle through each data set to filter
eval(['time1 = i' num2str(k) 't;']);
eval(['abso1 = i' num2str(k) 'adn;']);
eval(['time2 = o' num2str(k) 't;']);
eval(['abso2 = o' num2str(k) 'adn;']);

% determine the length
L1 = length(abso1);
L2 = length(abso2);

% determine the location of peak in absorbance profile
[h1,i1] = max(abso1);
[h2,i2] = max(abso2);

% define slope width (span of data for linear regression)
m = 4;
n = 7;
L3 = 1+n;

% rename absorbance arrays to avoid errors
abso1s = abso1;
abso2s = abso2;

% Apply smoothing filters to absorbance arrays. These values will
then be selectively pulled to create final filtered absorbance
array.
abso1_s7 = smooth(abso1,7);
abso2_s11 = smooth(abso2,9);
abso2_s41 = smooth(abso2,41);

% Calculate slope via linear regression and apple filter
% inlet array
for j = i1+m:L1-m;

    slope1 = polyfit (time1(j-m:j+m),abso1(j-m:j+m),1);

    if slope1(1,1) < -0.25
        abso1s(j) = abso1(j);
    else
        abso1s(j) = abso1_s7(j);
    end
    if abso1(j) < 0
        abso1s(j) = 0;
        else
    end
end
```

```
% Outlet array
for g = 1:L2-n;

    if g > n
        if g > i2+(30+n)
            slope2 = polyfit (time2(g-n:g+n),abso2(g-n:g+n),1);

            if slope2(1,1) < -0.012
                abso2s(g) = abso2_s11(g);
            else
                abso2s(g) = abso2_s41(g);
            end
        else
            abso2s(g)=abso2_s11(g);
        end
    else
    if abso2(j) < 0
        abso2s(j) = 0;
        else
    end
    end
end

% define delta time
DeltaTime1 = time1(2)-time1(1);
DeltaTime2 = time2(2)-time2(1);

% define denominator
D1 = abso1s*DeltaTime1;
D2 = abso2s*DeltaTime2;

Denom1 = sum(D1);
Denom2 = sum(D2);

% normalize density
E1 = abso1s/Denom1;
E2 = abso2s/Denom2;

eval(['i' num2str(k) 'adns = E1;']);
eval(['o' num2str(k) 'adns = E2;']);

mrt1 = time1'*E1/sum(E1);
mrt2 = time2'*E2/sum(E2);

% calculate mean residence times
mrt_diff = mrt2-mrt1;

eval(['mrtdis' num2str(k) '= mrt1;']);
eval(['mrtdos' num2str(k) '= mrt2;']);
eval(['mrtds' num2str(k) '= mrt_diff;']);

% plot filtered arrays with original data sets to visually inspect
for errors
```

```
subplot(2,1,1)
plot(time1,abso1)
xlabel('Time(sec)','FontSize',12)
ylabel('Normalized Concentration','FontSize',12)
title('Input','FontSize',12)

hold on

subplot(2,1,1)
plot(time1,E1,'r')
legend('Raw Input','Filtered Input')

hold off

subplot(2,1,2)
plot(time2,abso2)
xlabel('Time(sec)','FontSize',12)
ylabel('Normalized Concentration','FontSize',12)
title('Output','FontSize',12)

hold on

subplot(2,1,2)
plot(time2,E2,'r')
legend('Raw Output','Filtered Output')

hold off

shg
%pause(0)

clear range time1 time2 abso1 abso2 DeltaTime1 DeltaTime2 D1 D2
Denom1 Denom2 E1 E2 slope1 slope2 k j g m n h1 i1 h2 i2 L1 L2 L3
abso1_s7 abso2_s11 abso2_s41 mrt1 mrt2 mrt_diff

end
```

B.6 Script to perform deconvolution

```
clf
range = 1:10;

for k = range;

group = k

eval(['Input_time = i' num2str(k) 't;']);
eval(['Input_abs = i' num2str(k) 'adns;']);
eval(['Output_time = o' num2str(k) 't;']);
eval(['Output_abs = o' num2str(k) 'adns;']);

shrink_size = length(Input_time) ;
es = 0.01;
maxit = 200;

% smooth absorbance data
Input_abs2 = Input_abs;
Output_abs2 = Output_abs;

%calculate time step from original data
DeltaTime1 = Input_time(2) - Input_time(1);
DeltaTime2 = Output_time(2) - Output_time(1);

% define denominator
D1 = Input_abs2*DeltaTime1;
D2 = Output_abs2*DeltaTime2;
Denom1 = sum(D1);
Denom2 = sum(D2);

% normalize density
Input_abs3 = Input_abs2/Denom1;
Output_abs3 = Output_abs2/Denom2;

[ Input_abs4 ] = rvs2( Input_abs3, shrink_size );
[ Input_time2 ] = rvs2( Input_time, shrink_size );
[ Output_abs4 ] = rvs2( Output_abs3, shrink_size );
[ Output_time2 ] = rvs2( Output_time, shrink_size );

% Define variables and run deconvolution function
inp = Input_abs4;
outp = Output_abs4;
time_step = Input_time2(2)-Input_time2(1);
trun = length(Input_abs4);

[RTD,inp_small,outp_small,outp_numer,time_small,total_error,iter,inp
_diag,outp_shift] = deconvolution(inp,outp,time_step,trun,es,maxit);

subplot(2,1,1)
plot(time_small,RTD)
xlabel('Time(sec)','FontSize',12)
ylabel('Mass Percentage','FontSize',12)
```

```
title('Residence Time Distribution','FontSize',12)

subplot(2,1,2)
plot(time_small,outp_small)
xlabel('Time(sec)','FontSize',12)
ylabel('Normalized Concentration','FontSize',12)
title('Experimental and Convoluted Output','FontSize',12)

hold on

subplot(2,1,2)
plot(time_small,outp_numer,'r--')
legend('Experimental output','Convoluted output')

hold off

rtd_sum = sum(RTD);

rtd_mean = sum(time_small'*RTD);

% disp('')
% disp('Total error:')
% disp(total_error)
% disp('')
% disp('Iterations:')
% disp(iter)

mrt1 = Input_time'*Input_abs/sum(Input_abs);

eval(['RTD' num2str(k) '= RTD;']);
eval(['RTDsum' num2str(k) '= rtd_sum;']);
eval(['RTDmean' num2str(k) '= rtd_mean;']);
eval(['time_small' num2str(k) '= time_small;']);
eval(['XMat' num2str(k) '= inp_diag;']);
eval(['yvec' num2str(k) '= outp_shift;']);
eval(['outputRTD' num2str(k) '= outp_numer;']);
eval(['outp_small' num2str(k) '= outp_small;']);

clear f inp_diag mrt1 inp_small outp_small time_small maxit es trun
time_step inp outp clear DeltaTime1 DeltaTime2 D1 D2 Denom1 Demon2
shrink_size Input_abs Input_time Output_abs Output_time Input_abs2
Input_time2 Output_abs2 Output_time2 Output_abs3 Output_abs3
Input_abs3 Input_abs4;

shg
end
clear group

beep
```

B.7 Function file called by deconvolution script to perform Gauss-Seidel Method with conditions

```
function
[RTD,inp_small,outp_small,outp_numer,time_small,total_error,iter,inp
_diag,outp_shift] = deconvolution(inp,outp,time_step,trun,es,maxit)
% Deconvolution: Utilizing Gauss-Seidel method of iteration
%   [RTD,total_error,iter] = deconvolution(inp,outp,trun,es,maxit):
Gauss Seidel without relaxation
%input:
%   inp = input response
%   outp = output response
%   timestep = time step of output data
%   trun = size of new arrays for deconvolution (default = raw data)
%   es = stop criterion (default = 0.00001%)
%   maxit = max iterations (default = 50)
%output:
%   RTD = solution vector
%   total_error = sum of errors at each evaluation point
%   iter = number of iterations

% checking input conditions
if nargin<2, error('at least 2 input arguments required'),end
if nargin<3||isempty(trun), trun=size(inp);end
if nargin<4||isempty(maxit), maxit=50;end
if nargin<5||isempty(es), es=0.00001;end

% check to make sure input and output are same size
% if length(inp)~=length(outp), error('response signals must be same
size');end
% decided to remove this feature since I use variable time step now

% create the time array
time_end = length(outp)*time_step-time_step;
time = 0:time_step:time_end;
if length(time)~=length(outp), error('time array does not match
response signals');end

% create new array of x-values to accompany response values
% unused: xdata = 1:length(inp);
% create truncated coordinates
% first for input
xi_i = linspace(1,length(inp),trun);
% second for output and time
xi_o = linspace(1,length(outp),trun);

% use interp1 to shrink response profiles
inp_small = interp1(inp,xi_i,'linear');
outp_small = interp1(outp,xi_o,'linear');
time_small = interp1(time,xi_o,'linear');

% creating the diagonal matrix using a nested function
function [mat599] = diagmatrix(vec599)
```

```
n_vec=length(vec599);
% determin location of maximum value in inp_small
[~,W]=max(vec599);
% creating zeros square matrix size of inp_small + W - 1
K=zeros(n_vec+W-1,n_vec+W-1);

% filling in matrix with inp_small with max value on diagonal
for r = 1:n_vec+W-1
    for j = 1:n_vec
        if j+r-W>0
        K(j+r-W,r)=vec599(j);
        end
    end
end

mat599=K(1:n_vec+W-1,1:n_vec+W-1);
end

inp_diag = diagmatrix(inp_small);

% check if inp_diag matrix is square
[m,n] = size(inp_diag);
if m~=n, error('Matrix must me square');end
C = inp_diag;

% outp_small becomes outp_shift to account for diagonal dominance
shift
outp_shift = zeros(m);
outp_shift(m-length(outp_small)+1:m)=outp_small;
time_shift = m-length(outp_small);


% creating square matrix with adjusted coefficients
for i = 1:n
    C(i,i) = 0;
end
for i = 1:n
    C(i,1:n) = C(i,1:n)/inp_diag(i,i);
end

% creating x-array that will become RTD at end
x = zeros(n,1);

% creating array of modified coefficients previous associated with
solving variable x(i)
d = zeros(n,1);
for i = 1:n
    d(i) = outp_shift(i)/inp_diag(i,i);
end

% error value array
ea=zeros(n,1);
% setting iteration # to zero
iter = 0;
```

```
% loop will run until one criteria in last 'if' is satisfied
while (1)
    %separating old and new x values
    xold = x;
    for i = 1:n
        % ex.: x1 = b1/a1 - a2*x2/a1 - a3*x3/a1 -...
        x(i) = d(i)-C(i,:)*x;
        % condition: no negative values
        if x(i)< 0
            x(i)=0;
        end
        % calculating error and storing value
        if x(i) ~= 0
            ea(i) = abs((x(i) - xold(i))/x(i))*100;
        end
    end
    % bump iteration # up 1 each cycle
    iter = iter+1;
    % criteria: maximum error equal or less than error specified
    % iteration number reaches maximum
    if max(ea)<=es || iter >= maxit, break, end
end

% eliminate extra zeroes at beginning of RTD array

RTD = zeros(length(time_small'),1);
[~,inputmaxloc]=max(inp_small);
choppedRTD=x(2*inputmaxloc-1:end);
RTD(1:length(choppedRTD))=choppedRTD;

% calculated predicted output response
outp_numerical = inp_diag*x;
outp_numer = outp_numerical((time_shift+1):m);

total_error = sum(abs(outp_small-outp_numer'))/sum(outp_small)*100;

time_small = time_small';

end
```

B.8 Local regression filtering

```
clf

range = 1:10;
m=9;

for k = range;

eval(['dummyrtd = RTD' num2str(k) ';']);
eval(['dummytime = time_small' num2str(k) ';']);

dummyrtds = smooth(dummyrtd,m,'lowess');

eval(['RTD' num2str(k) 's' num2str(m) '= dummyrtds;']);

plot(dummytime,dummyrtd,'b')
hold on
plot(dummytime,dummyrtds,'r');
hold off

shg

pause(0.5)

clear dummyrtd dummyrtds dummytime

end

clear range
```

B.9 Script for calculating statistical values from RTD results

```
% k defines the range of data sets to pull from
for k = 1:10;

eval(['stattime = time_small' num2str(k) ';']);
eval(['statRTD = RTD' num2str(k) 's9;']);

[mean,varia,skew] = stat_pack(stattime,statRTD);

eval(['z' num2str(k) 'af= mean;']);
eval(['z' num2str(k) 'bf= varia;']);
eval(['z' num2str(k) 'cf= skew;']);

end

clear stattime statRTD mean varia skew

beep
```

B.10 Function file called by stat_pack script for RTD analysis

```
function [ mean, variance, skewness ] = stat_pack( time, rtd )
%STAT_PACK gives you mean (first moment) and variance (second
moment) of
% set of data (x and y), specifically designs for RTD analysis
%   --function [ mean, variance ] = stat_pack( time, rtd )--
%   time: [m:1] array
%   rtd: [m:1] array

mean = time'*rtd / sum(rtd);

variance = (time.*time)'*rtd / sum(rtd) - mean^2;

%skewness = (time.*time.*time)'*rtd/sum(rtd) - mean^3;

m3 = sum((time-mean).^3.*rtd)/sum(rtd);
%m2 = sum((time-mean).^2.*rtd)/sum(rtd);

skewness = m3/variance^(3/2);

% variance is equal to m2, another way of stating relation
% that first definition of skewness is not correct and may only
represent
% the 3rd central moment

end
```

B.11 Calculating error of filtered RTD based on difference in output profile

```
% define span length to pull rtd from
m=13;

for k = 1:10;

    eval(['dummyRTD = RTD' num2str(k) 's' num2str(m) ';']);
    eval(['dummytime = time_small' num2str(k) ';']);
    eval(['dummyinput = i' num2str(k) 'adns;']);
    eval(['origoutput = outp_small' num2str(k) ';']);
    eval(['origrtdoutp = outputRTD' num2str(k) ';']);

    toepvec = zeros(length(dummyRTD),1);
    toeplitzRTD = toeplitz(dummyRTD,toepvec);
    ConvOutput = toeplitzRTD*dummyinput;

    OutputError= sum(abs(ConvOutput-origoutput'))/sum(origoutput');

    eval(['outp_error' num2str(k) 's' num2str(m) '=OutputError;']);
    eval(['outp_small' num2str(k) 's' num2str(m) '=ConvOutput;']);

    plot(dummytime,ConvOutput,'r')
    hold on
    plot(dummytime,origoutput,'b')
    plot(dummytime,origrtdoutp,'g')
    hold off
    shg
    pause(1)

    clear origrtdoutp dummyRTD dummytime dummyinput origoutput
toepvec toeplitzRTD ConvOutput OutputError

end

clear k m
```

Appendix C: Experimental Results

C.1 Design 1 – Slim header, mean residence times for various channel blockage conditions. All measurements collected.

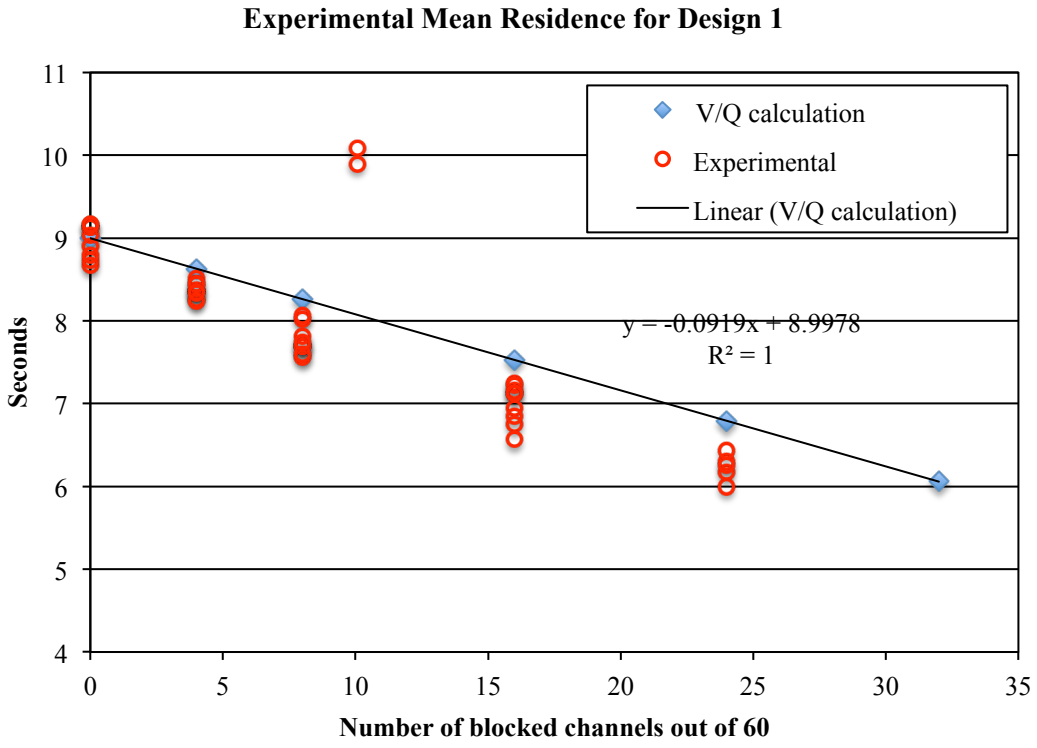

Figure 92. Individual mean residence times measured from pulse response test loop compared with predicted mean residence times.

C.2 Design 2 – Wide-header, mean residence times for various channel blockage conditions. All measurements collected.

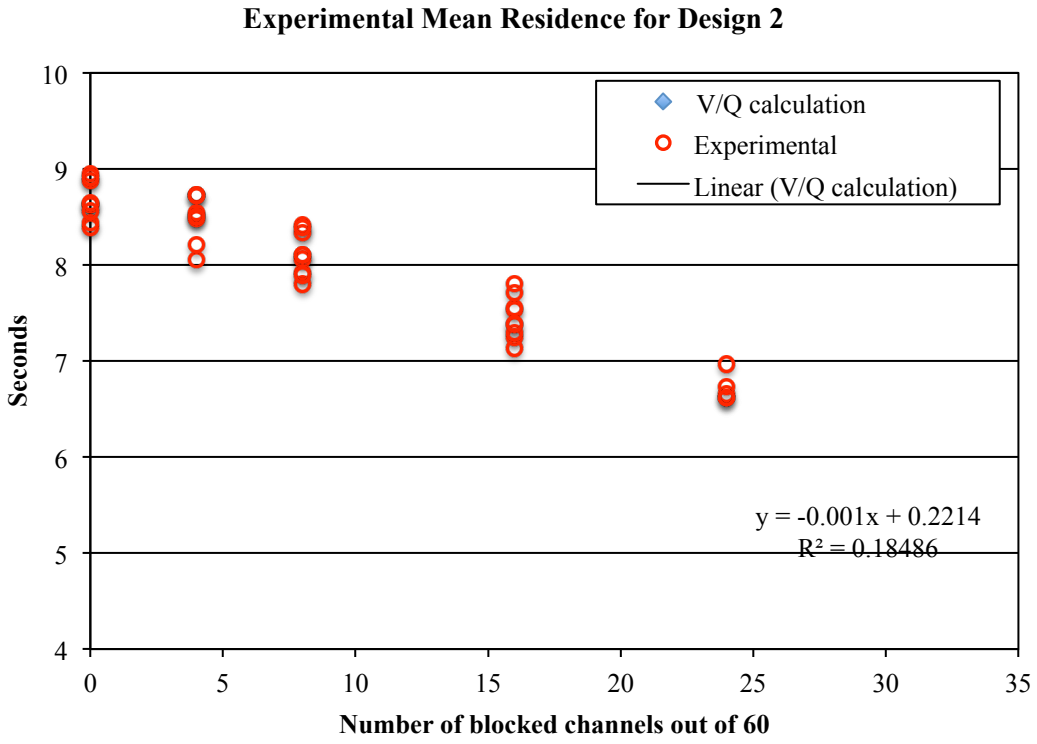

Figure 93. Individual mean residence times measured from pulse response test loop compared with predicted mean residence times.

C.3 Design 3 – Wide-posts, mean residence times for various channel blockage conditions. All measurements collected.

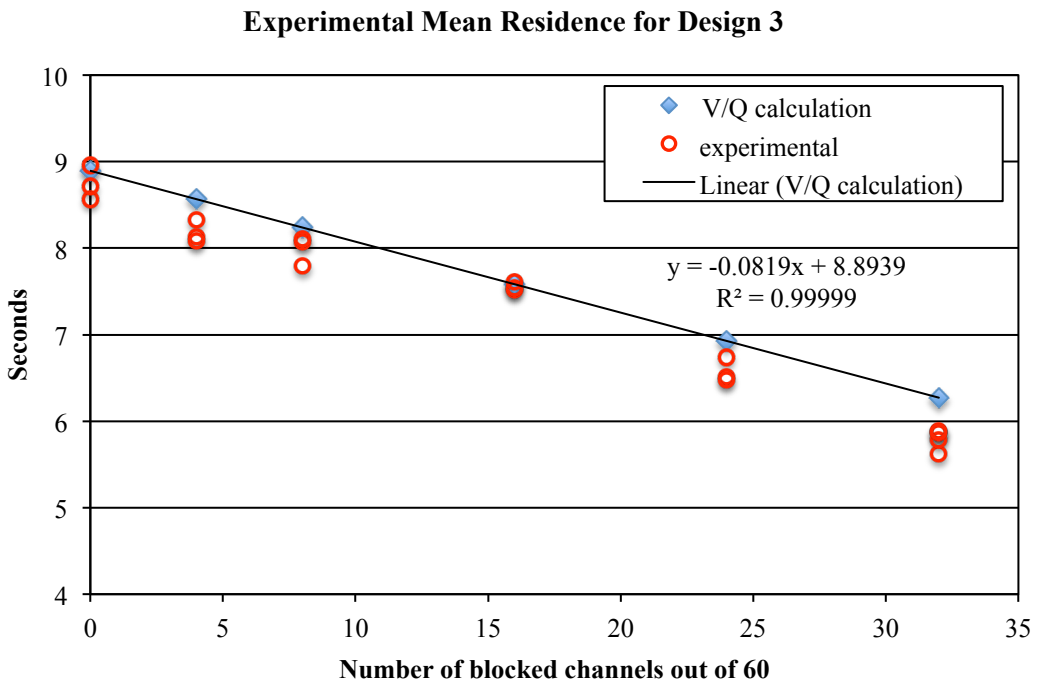

Figure 94. Individual mean residence times measured from pulse response test loop compared with predicted mean residence times.

C.4 Histograms of experimental vs. predicted MRT for design 1 and design 2

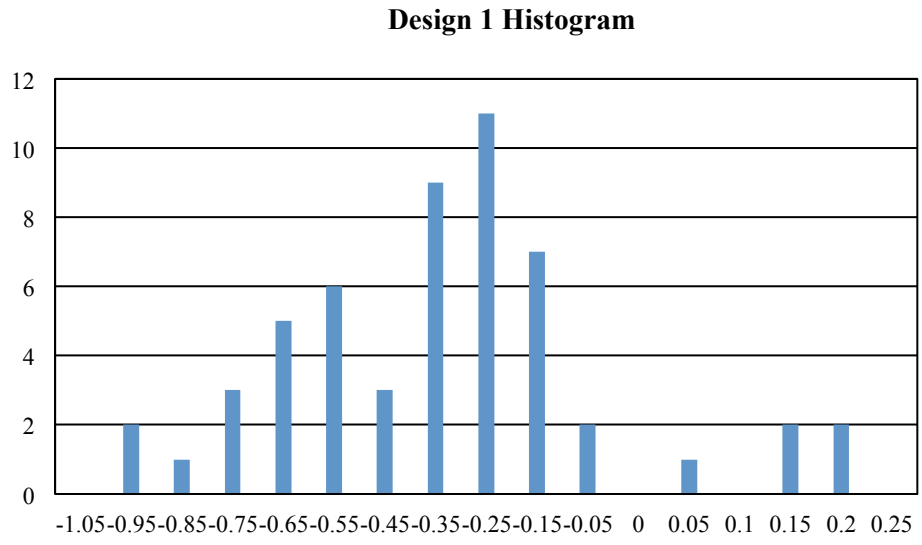

Figure 95. Design 1 Slim-header: difference between experimental and predicted mean residence times are plot in a histogram to verify results behave with ordinary variation.

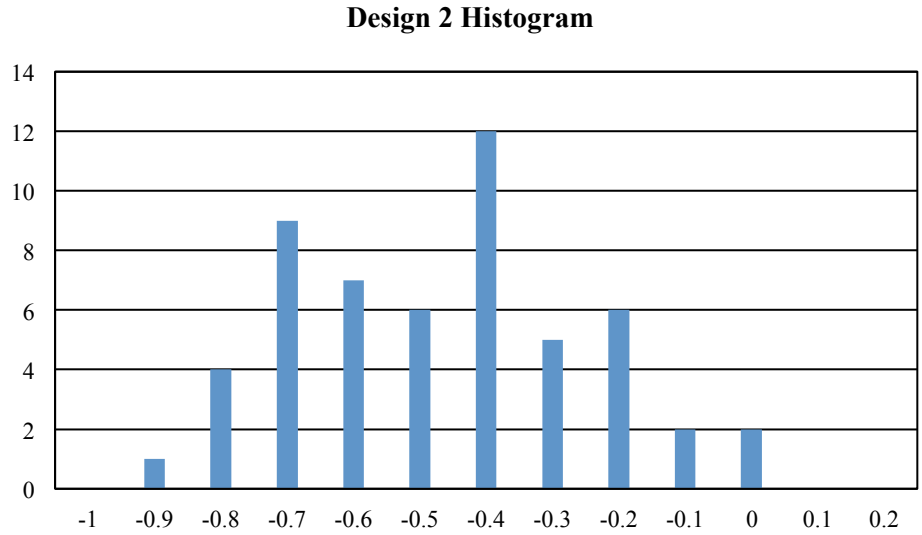

Figure 96. Design 2 Wide-header: difference between experimental and predicted mean residence times are plot in a histogram to verify results behave with ordinary variation.

C.5 Tables of mean residence times from pulse response measurements

Table 11 Mean residence times for Design 1 Slim-header

Blocked Chan.	0	0	0	4	4	4	8	8	8
Run	1	2	3	1	2	3	1	2	3
	8.669	9.128	8.797	8.363	8.266	8.243	7.690	7.563	7.744
	8.733	8.907	9.165	8.508	8.359	8.437	7.699	7.595	8.020
	9.038	9.128	9.160	8.445	8.366	8.339	7.689	7.817	8.064
Average			8.97			8.37			7.76

Blocked Chan.	16	16	16	24	24	24	32	32	32
Run	1	2	3	1	2	3	1	2	3
	6.947	6.751	6.572	6.000	6.254	5.864	5.375	5.305	5.363
	7.242	7.159	7.130	6.169	6.429	6.502	5.082	5.686	5.717
	7.228	7.118	6.848	6.299	6.434	6.460	5.455	5.839	5.822
Average			7.00			6.27			5.52

Table 12 Mean residence times for Design 2 Wide-header

Blocked Chan.	0	0	0	4	4	4	8	8	8
Run	1	2	3	1	2	3	1	2	3
	8.633	8.393	8.438	8.735	8.215	8.539	7.800	8.061	8.098
	8.630	8.647	8.558	8.730	8.481	8.501	8.332	7.919	8.110
	8.949	8.874	8.915	8.054	8.520	8.723	8.413	7.896	8.388
Average			8.67			8.50			8.11

Blocked Chan.	16	16	16	24	24	24	32	32	32
Run	1	2	3	1	2	3	1	2	3
	7.245	7.556	7.391	6.656	6.614	6.855	6.638	6.092	6.260
	7.137	7.292	7.710	6.967	6.620	6.877	6.532	6.369	6.305
	7.533	7.379	7.810	6.733	6.843	7.022	6.704	6.233	6.198
Average			7.45			6.80			6.37

Table 13 Mean residence times for Design 3 Wide-posts

Blocked Chan.	0	4	8	16	24	32
	8.564	8.132	7.797	7.513	6.510	5.623
	8.710	8.083	8.069	7.547	6.480	5.785
	8.960	8.325	8.103	7.613	6.734	5.868
Average	8.74	8.18	7.99	7.56	6.57	5.76

Table 14 Mean residence times for Design 4 All-posts

Blocked Chan.	0.00	4	8	16	24	center
	10.063	8.750	9.048	9.477	8.184	9.487
	10.063	8.725	9.031	9.652	8.617	9.880
	10.222	8.756	8.678	9.593	8.714	10.000
Average	10.12	8.74	8.92	9.57	8.50	9.79

C.6 Examples of a data set passed through a moving average filter and a local regression filter

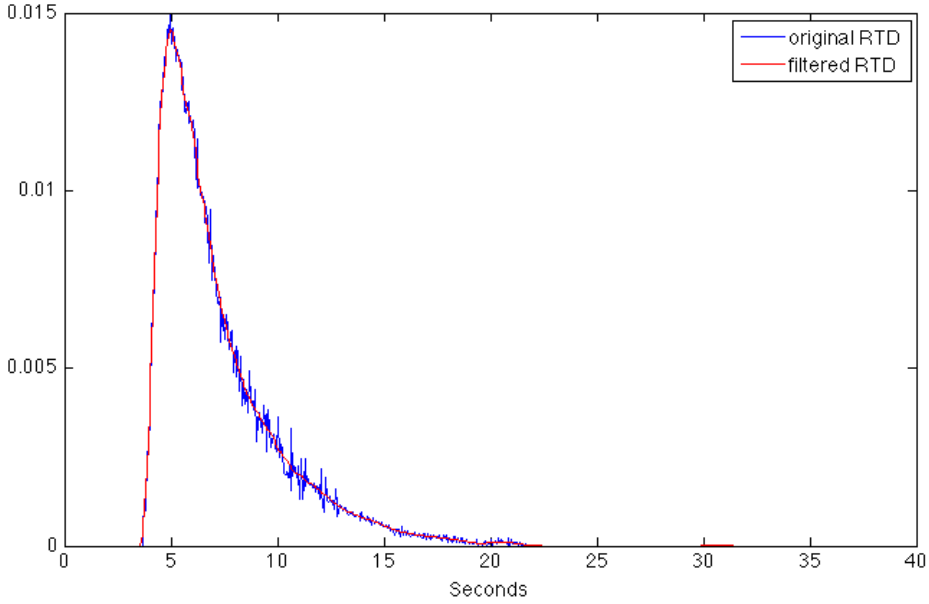

Figure 97. Example of a RTD profile that converged on a solution (low noise) passed through a moving average filter

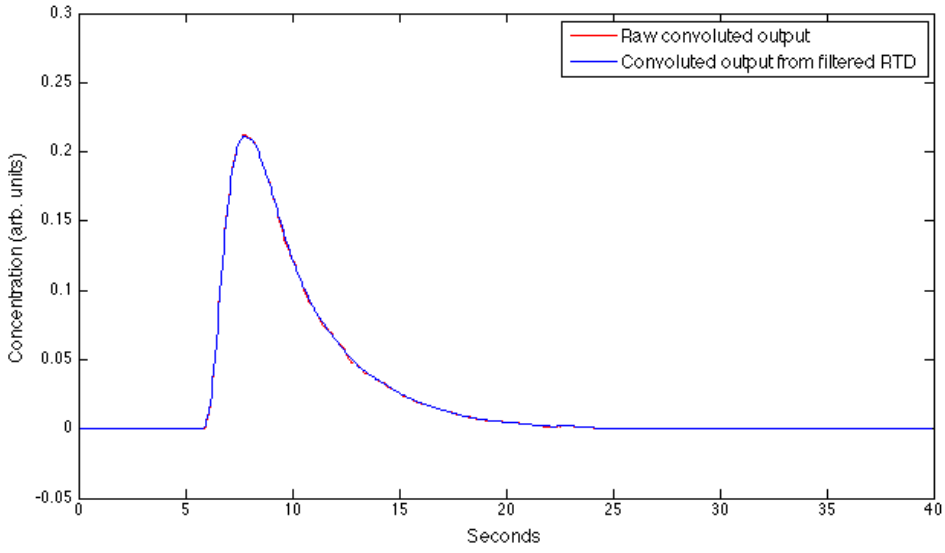

Figure 98. Resulting reconvoluted output from Figure 97 results. Total relative error: 0.78%.

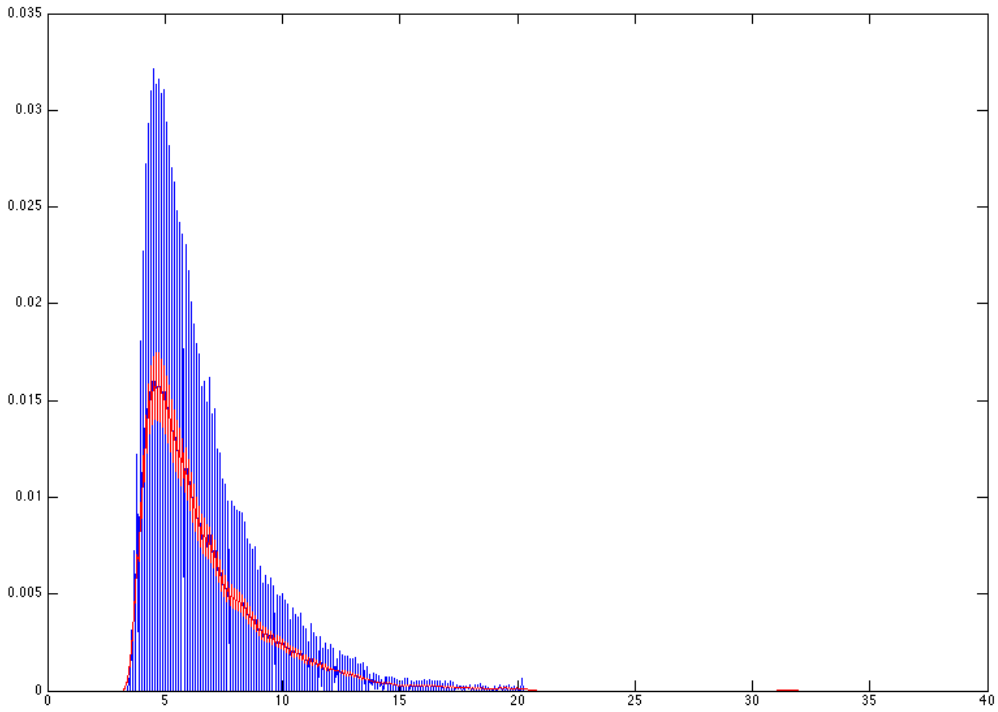

Figure 99. Example of a RTD profile with lower convergence on a solution (high noise) passed through moving average filter, span length: 8 units. RTD: blue, Filtered RTD: red.

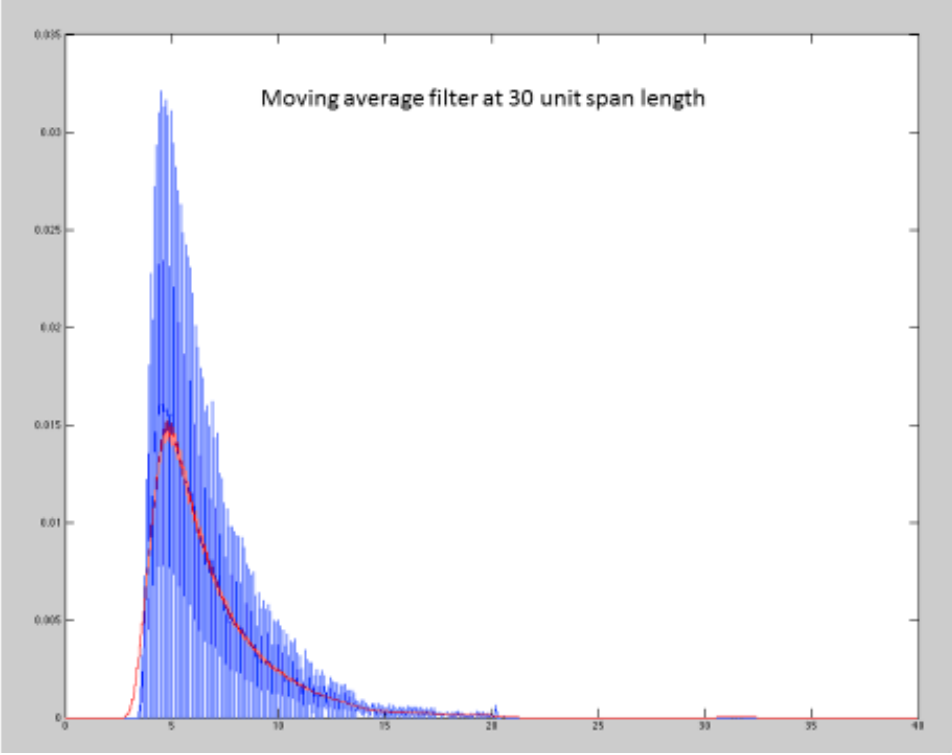

Figure 100. Example of a RTD profile (same data set as Figure 99) passed through moving average filter, span length: 30 units. RTD: blue, Filtered RTD: red.

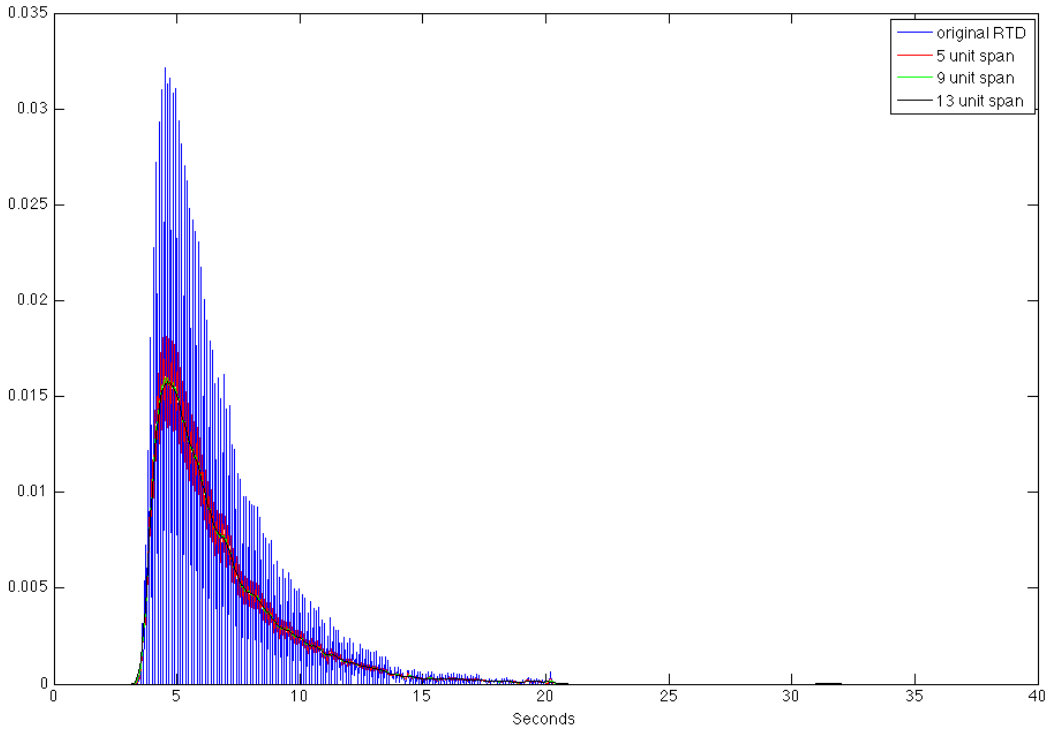

Figure 101. Example of a RTD profile (same data set as Figure 99) passed through local regression filters of various span lengths.

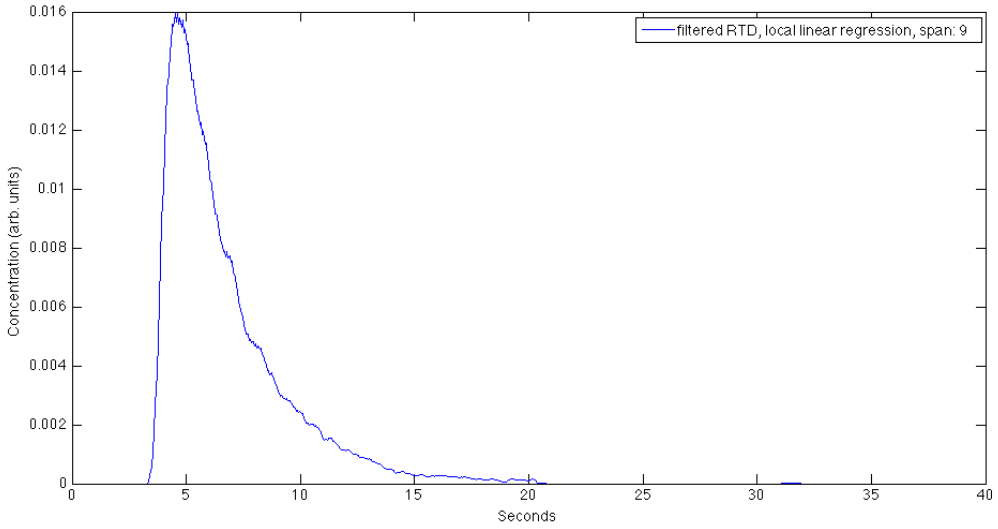

Figure 102. Filtered RTD results from Figure 101. Only showing results from filter set to span length of 9 units.

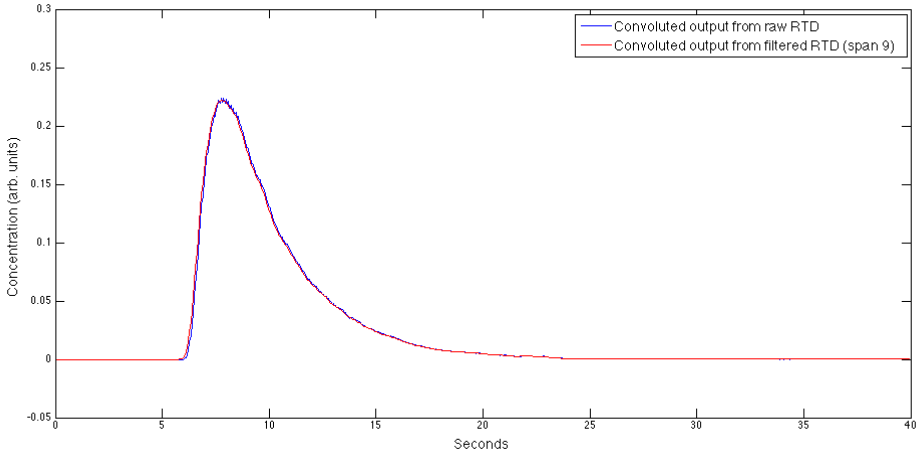

Figure 103. Resulting reconvoluted output from Figure 102 results. Total relative error: 2.6%.

C.7 Images of dye tracer flowing through unprimed design 4 lamina

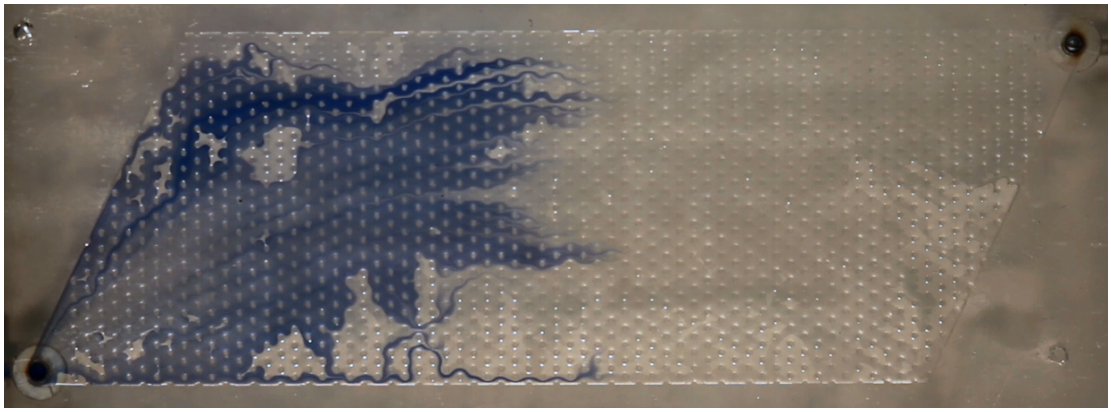

Figure 104. Design 4 All-posts lamina unprimed at 1.18 ml/min as the dye flows through main portion of the micro-post grid. Flow from left to right.

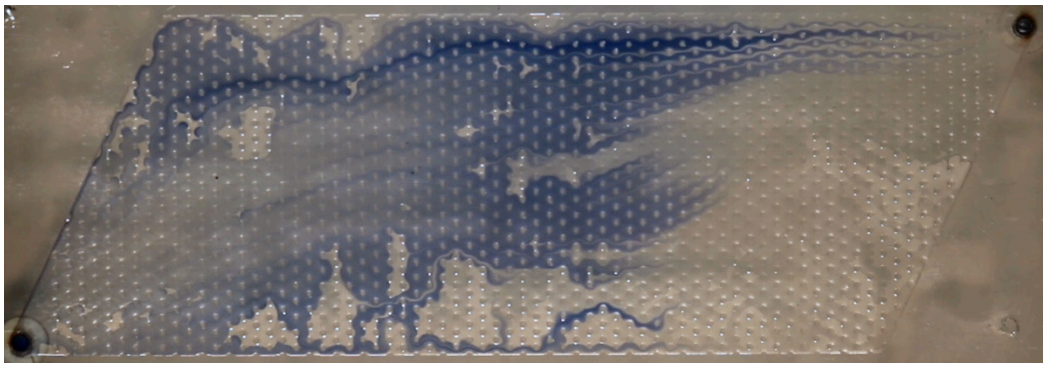

Figure 105. Same tracer recording as Figure 104 but taken later during process. Note the dye flow around the stagnant bubbles. Flow from left to right.

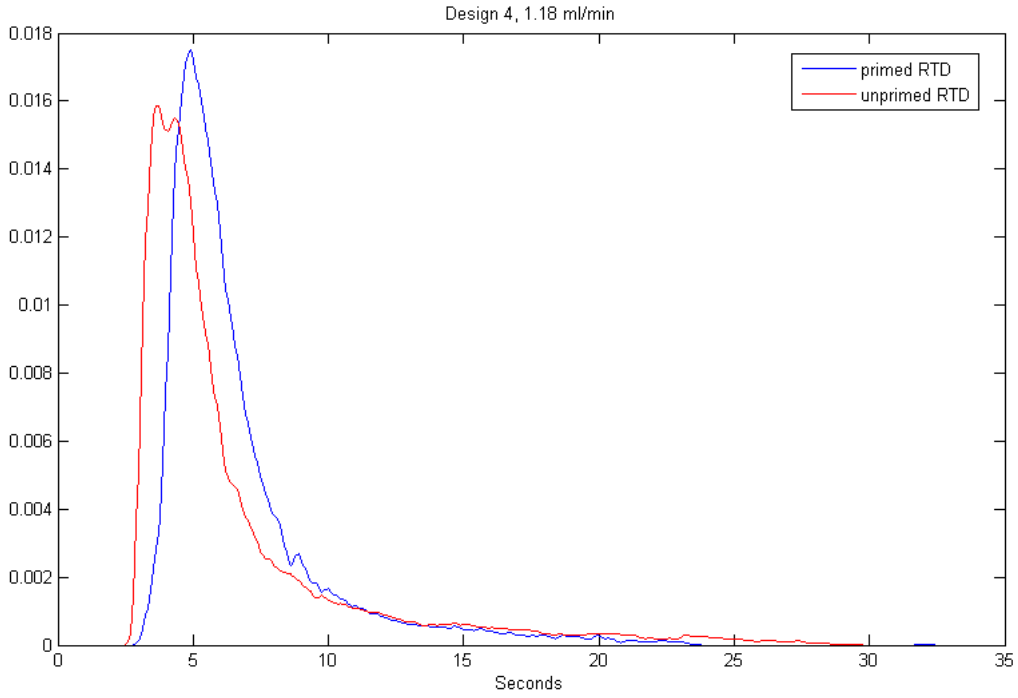

Figure 106. RTDs from pulse response measurements of design 4 all-posts lamina unprimed and primed at 1.18 ml/min. Unprimed data set is from same measurement used for images in Figure 104 and Figure 105.

C.8 Mean residence times and variance at difference channel blockage conditions plotted together for the slim-header, wide-header, and wide-posts lamina designs.

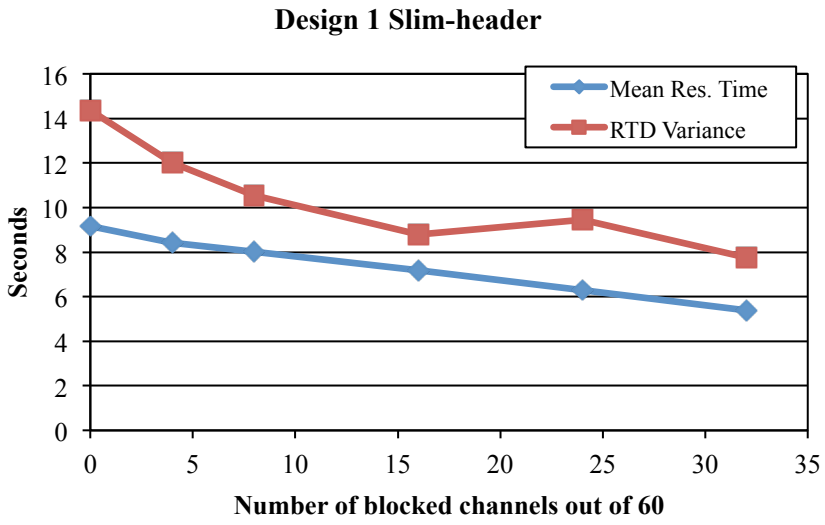

Figure 107. Design 1 Slim-header, mean residence time and variance calculated from residence time distributions

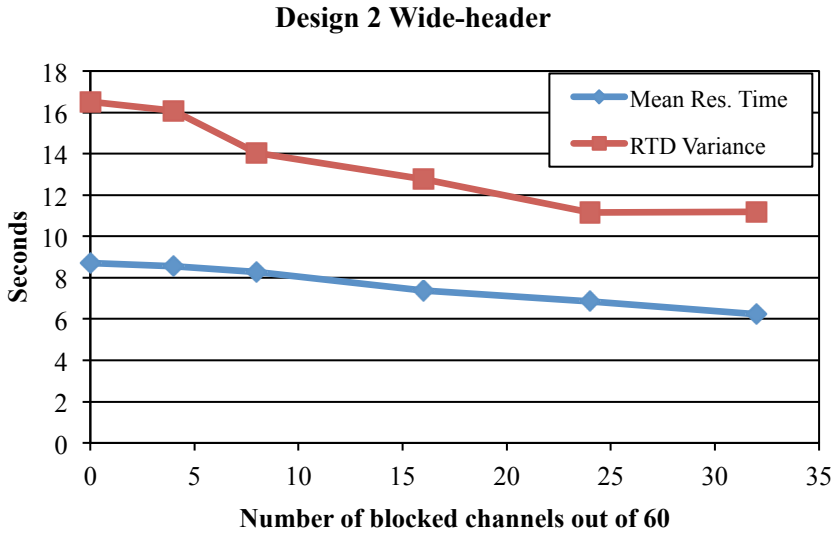

Figure 108. Design 2 Wide-header, mean residence time and variance calculated from residence time distributions

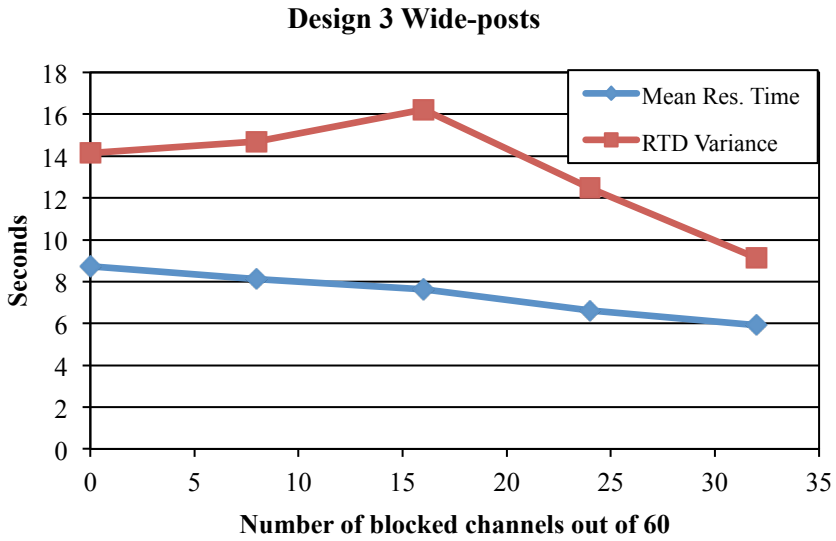

Figure 109. Design 3 Wide-posts, mean residence time and variance calculated from residence time distributions